



The Specific Heat of Astro-materials: Review of Theoretical Concepts, Materials, and Techniques

Jens Biele¹ · Matthias Grott² · Michael E. Zolensky³ · Artur Benisek⁴ · Edgar Dachs⁴

Received: 3 March 2022 / Accepted: 21 May 2022 / Published online: 1 August 2022
© The Author(s) 2022, corrected publication 2022

Abstract

We provide detailed background, theoretical and practical, on the specific heat of minerals and mixtures thereof, ‘astro-materials,’ as well as background information on common minerals and other relevant solid substances found on the surfaces of solar system bodies. Furthermore, we demonstrate how to use specific heat and composition data for lunar samples and meteorites as well as a new database of endmember mineral heat capacities (the result of an extensive literature review) to construct reference models for the isobaric specific heat c_p as a function of temperature for common solar system materials. Using a (generally linear) mixing model for the specific heat of minerals allows extrapolation of the available data to very low and very high temperatures, such that models cover the temperature range between 10 K and 1000 K at least (and pressures from zero up to several kbars). We describe a procedure to estimate $c_p(T)$ for virtually any solid solar system material with a known mineral composition, e.g., model specific heat as a function of temperature for a number of typical meteorite classes with known mineralogical compositions. We present, as examples, the $c_p(T)$ curves of a number of well-described laboratory regolith analogs, as well as for planetary ices and ‘tholins’ in the outer solar system. Part II will review and present the heat capacity database for minerals and compounds and part III is going to cover applications, standard reference compositions, $c_p(T)$ curves, and a comparison with new and literature experimental data.

Keywords Meteorites · Minerals · Rocks · Solid matter · Specific heat · Thermophysical properties

This article is part of the Special Issue on Thermophysics of Advanced Spacecraft Materials and Extraterrestrial Samples.

✉ Jens Biele
Jens.Biele@dlr.de

Extended author information available on the last page of the article

1 Introduction

Specific heat $c_p(T)$ is one of the parameters which determine a surface's temperature response to (solar) heating. Remote sensing in the mid-infrared is often used to estimate a parameter termed the thermal inertia of the surface material, which is defined as $\Gamma(T) = \sqrt{\rho(T)k(T)c_p(T)}$, where (in SI units) T is absolute temperature in K, k is thermal conductivity in $\text{W}\cdot\text{m}^{-1}\cdot\text{K}^{-1}$, ρ is bulk density in kg m^{-3} , and c_p is specific heat at constant pressure in $\text{J}\cdot\text{kg}^{-1}\cdot\text{K}^{-1}$. Knowledge or an estimate of $c_p(T)$ is required to extract information on, e.g., thermal conductivity k from the data, which in turn allows for an estimation of important surface properties like grain size [1–5] and porosity [6]. Furthermore, knowledge of thermophysical surface properties (including porosity) is essential to model the Yarkovsky [7–9] and YORP [9, 10] effects as well as the response of planetary surfaces to impact cratering [11, 12]. In comets, the surface material is a mixture of ices (water ices, CO, CO₂) and silicate dust, which in most of a comet's orbit is at very low temperatures—with a very different specific heat than commonly assumed for silicates near room temperature. Trans-Neptunian objects (TNOs) and icy moons likewise have a surface composition very different from, e.g., the Moon—thus we need to know specific heats of solar system ices and of the so-called 'tholins,' the 'complex abiotic organic gunk' [13] on the very surface.

Piqueux et al. [14] have recently studied the effect of composition- and temperature-dependent specific heat on thermal modeling of surfaces in the solar system. We agree with them that under non-cryogenic conditions, the composition is typically (excluding perhaps metal-rich worlds like M-type asteroids) not a significant factor controlling $c_p(T)$ and thermal inertia trends, and even the temperature dependence of specific heat has usually only a second-order influence on surface temperatures (although it must at least be considered in the error budget since the advent of high-resolution, high-precision thermal datasets).

However, we also agree with [14, 15] that surface temperature models could be impacted by the drastic decrease in $c_p(T)$ values toward low temperatures; thermal models generally assume lunar basalt calorimetric properties, which are not well known outside the data range 90 K to 350 K. Indeed, 'knowledge of specific heat variability as a function of temperature and bulk material composition remains largely under-constrained for the need of planetary thermal modelers' [14]. In particular, the specific heat capacity of geological materials relevant to solar system body surfaces below room temperature is not particularly well constrained and the thermal modeling community only has a limited set of adequate ready-to-use $c_p(T)$ trends for planetary surface temperature modeling.

The goal of Piqueux et al. is to provide a reference for thermal models by providing experimental data on a wide range of materials—covering a wide range of compositions and temperatures relevant to planetary surfaces—from which thermal models can incorporate the most appropriate one.

Our approach is complementary: We provide the means to calculate synthetic $c_p(T)$ from a known bulk composition, and additionally a method to predict the

specific heat curve beyond the temperature range measured, even if the composition is not (well) known.

Unbeknownst maybe to most astronomers and planetary scientists, many precise heat capacity data exist for hundreds of minerals, over wide temperature ranges, yet in particular for temperatures below 25 °C [16], they are scattered in the literature. Our motivation thus is also to collect, merge, critically review and tabulate these data for substances of interest, and to make this database readily available.

Around room temperature, the temperature dependence of c_p is a second-order effect in the thermal inertia, and except for the mass fraction of meteoritic iron (FeNi), and to a lesser degree phyllosilicates, specific heat is not very strongly dependent on the specific material. However, at low temperatures c_p shows a strong temperature and compositional dependence. Specific heat must approach 0 as temperature approaches absolute zero, and it is usually proportional to T^3 at very low temperatures. Specific heat furthermore shows a noticeable, about linear increase at very high temperatures, which is caused by anharmonicity of the lattice vibrations and by thermal expansion (only harmonic lattice C_V , heat capacity at constant volume, obeys the Dulong–Petit limit).

The range of temperatures relevant for this study is given by the minimum and maximum surface temperatures in the solar system, which span a large range from asteroids with smallest perihelia and Mercury to cold TNOs at the edge of the Edgeworth–Kuiper belt. While Mercury has maximum surface temperatures of up to 700 K and some asteroids even ~ 1000 K (e.g., (3200) Phaethon and (155,140) 2005 UD [17]), TNOs have night time temperatures down to ~ 10 K to 30 K, and even on the Moon, surface temperatures as low as 25 K have been measured in permanently shadowed craters in the vicinity of the south pole [18, 19]. Therefore, we aim for a description and parameterization of specific heat in the temperature range between 10 K and 1000 K, while simultaneously allowing for a physical reasonable extrapolation to 0 K as well as to the respective melting temperatures. The latter are typically of the order of 1400 K for silicates, while the threshold temperature for sintering of silicates is close to 700 K [20].

Note that knowledge of specific heat is also necessary to calculate thermal conductivity from thermal diffusivity measurements (e.g., by the flash method [21]).

Data on the specific heat of extra-terrestrial material (apart from the Apollo lunar samples) are scarce, and only a handful of c_p data of meteorites have been published (most of them measured at temperatures at or above 300 K) until quite recently; since about 2012, there has been a surge of new meteorite specific heat data [14, 22–30]. The only other extra-terrestrial material with known c_p over a wide temperature range is lunar samples from the Apollo missions, and lunar $c_p(T)$ has widely, but not always wisely, been used as a representative standard in studies covering solar system bodies ranging from asteroids [4] to planets like Mars [31]. However, heat capacity can strongly depend on composition, thus the use of lunar data for, e.g., C- or M-class asteroids or objects containing frozen volatiles may give rise to large systematic errors. Furthermore, most available data cover only a limited temperature range, introducing further uncertainty when extrapolating to lower or higher temperatures. In the next years, however, it is expected that the first specific

heat data of asteroid material will become available, e.g., from the Bennu samples acquired by the OSIRIS-REx mission [32].

$c_p(T)$ data for rocks (in general, ‘astro-material,’ any solid material present on the surface of solar system bodies) can be calculated from the contributions of the constituent minerals (and mineraloids, i.e., amorphous substances). This is particularly important when studying the surfaces of outer solar system objects like icy moons, comets, or TNOs, as the specific heat capacities of ices are dramatically different from those of silicates near room temperature. We will also demonstrate how $c_p(T)$ measurements over a limited temperature range (example: lunar regolith) can be meaningfully extrapolated.

One of the problems that has to be considered when calculating specific heat of astro-material is that the minerals are usually neither perfectly mechanically mixed nor do they show solid solutions of the same composition throughout the sample of interest. This is clear from the study of meteorites, which show compositional zoning and obvious inhomogeneities in the form of chondrules (of mostly < 1 mm diameter), embedded in a fine-grained matrix, but also from brecciated meteorites like siderolites (stony iron meteorites). A linear mixing model for c_p is only valid at spatial scales larger than the intrinsic spatial inhomogeneities. Note that natural polycrystalline minerals often exhibit a range of solid solution compositions (i.e., characteristic zoning patterns) at length scales of the order of the grain size, indicating changes in pressure and temperature conditions during crystallization ([33, 34] and references therein). This has implications for any composition-dependent transition peaks in the c_p curve (FeNi is possibly the most important example, but only at temperatures between ~600 K and ~1000 K), and appropriate averaging is necessary if utmost peak fidelity is sought.

More practically, if in a given sample volume a mineral with composition-dependent transition peaks is present with a significant mass fraction, and that mineral has a range of compositions within that sample volume, smearing out of the sample-averaged transition peaks is expected. We speculate that this effect will obscure the magnetic transition peaks in olivine (Fo–Fa) to a slight hump between ~20 K and ~60 K, and in iron-bearing pyroxenes (Di–Hed, En–Fs; augites and pigeonites) between ~10 K and ~40 K, possibly also in non-stoichiometric compounds like wüstite Fe_{1-y}O and pyrrhotite Fe_{1-x}S , but not in minerals like magnetite.

When interpreting remote sensing observations of thermal emission, it is important to note that observations are sensitive to average thermal properties. First of all, averaging takes place horizontally over the size of the instrument’s footprint, which can range from cm to km scales. Furthermore, thermal properties are also averaged vertically over the thermal skin depths¹ s , i.e., the e-folding length of the

¹

$$s = \sqrt{\kappa P / \pi \rho c_p} = \frac{\Gamma}{\rho c_p} \sqrt{\frac{P}{\pi}}$$

P is the diurnal period, κ the thermal conductivity (note that erroneously, sometimes a factor of 2 in the denominator of the fraction under the root appears; also, it remains to be studied what the e-folding length is for surface temperature waves that are not sinusoidal, like the simple thermal model surface temperature (thermal inertia 0, $T=0$ at night) or for step T changes at the surface).

periodic surface temperature forcing. The diurnal skin depth of solar system bodies surfaces typically varies between 2 mm and 1 m [35] such that the specific heat of the observed surfaces can usually be regarded as homogeneous. However, laboratory specific heat measurements of meteorites often involve only tens of milligrams of material, and care has to be taken to grind and mix a representative volume of the specimen and all its constituents in unbiased proportions; this can be problematic with meteorites containing ductile FeNi metal besides brittle minerals [36].

Note that c_p of a homogeneous crystalline material is independent of particle size down approximately 50 nm, whereas nanoparticles show deviations from the bulk specific heat value due to surface effects and a strong discretization of possible lattice vibration modes [37].

We will review the available data on lunar samples and meteorites as well as the specific heat capacities of the most abundant endmember minerals including iron–nickel metal. Furthermore, organic materials found in meteorites and frozen volatiles thought to exist on outer solar system bodies are also considered. From these data, we built up a computerized database to calculate the specific heat of approximately 100 minerals and compounds for temperatures between absolute zero and close to melting (or decomposition temperature) by the usage of tables and correlation equations apt for convenient but accurate interpolation.

The paper is organized as follows: in Sect. 1, we first summarize the relevant background on heat capacity, its temperature and pressure dependence as well as useful approximations, and discuss the various transitions and effects of crystallinity and particle size. The concept of endmember minerals and mechanical mixtures versus solid solutions is introduced, and polymorphs as well as phase transitions are discussed.

Section 2 gives background on minerals and compounds reviewed in this work (Table 5). We also investigate which minerals are compositionally likely to be important on the terrestrial planets (other than Earth) and the moon, since otherwise we have focused on minerals known to be important in meteorite samples. This section also presents a table with an overview of our database. We then briefly summarize textbook descriptions of the most common and important mineral groups that occur in solar system materials and which are part of the c_p database. Note the newly introduced sections on carbon-rich/organic matter, on solar system ices and on tholins. For each material, if necessary, important aspects of the specific heat like the influence of composition, (adsorbed/hydrate) water content, transitions, solid solutions, isomorphs, and thermal alteration at elevated temperatures are emphasized. The detailed description of methods and used input data, for each mineral and compound covered, will be given in paper II.

Section 3 gives some examples what can be done with the methodology presented here, using the database; Sect. 4 summarizes the paper and Sect. 5 gives an outlook.

In Online Appendix (Supplementary Information), we describe methods like our accurate Padé approximant to the 3D-Debye function and details on the results shown in Sect. 3, list all data known to us on measured meteorite heat capacities and lunar samples, and present the reference $c_p(T)$ for lunar regolith and some (mostly commercial) laboratory regolith simulants along with the mineral compositions of the latter.

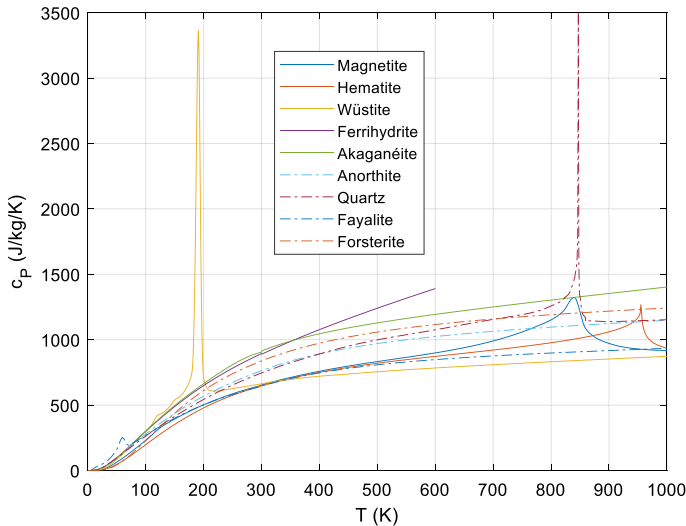


Fig. 1 Example c_p curves, (magnetic) transition peaks in some iron oxides, quartz with the λ transition (α - β) at 843 K, fayalite with its low-temperature magnetic transition, forsterite and anorthite with no anomalies. Note that magnetite has a small broad Verwey peak at ~ 124 K which here shows only as a ‘bump.’ Akaganéite here is β -FeOOH \cdot 0.65H $_2$ O and the ferrihydrite is 2-line

2 Background: Heat Capacity of Solids

Heat capacity is a bulk thermodynamic quantity; at constant pressure, we have $C_p = (\partial H/\partial T)_p$ and at constant volume, $C_v = (\partial U/\partial T)_v$, where H is enthalpy, U internal energy. While strictly an extensive property, it is always made intensive. Molar heat capacity, C , is conventionally just called ‘heat capacity’ of a compound while the ‘specific heat,’ c , refers to unit mass. In calorimetry, the temperature range 0 to $340 \text{ K} \pm 40 \text{ K}$ is traditionally called ‘low temperature’ and the range $340 \pm 40 \text{ K}$ to melting (or decomposition) temperature ‘high temperature.’ Also traditionally, and somewhat arbitrarily, temperatures below $90 \text{ K} \pm 10 \text{ K}$ are called ‘cryogenic.’ Experimentally, c_p is measured, and C_p can only be given for substances of known chemical composition: $C_p = c_p M$, where M is the molar mass. In this paper, we use C , c where necessary (e.g., in Eqs. 1, 2). Wherever it does not matter, we use ‘heat capacity,’ C_p and ‘specific heat,’ c_p , interchangeably.

c_v is very difficult to measure directly, but can be calculated from c_p (see below). The heat capacity of solids depends mainly on temperature, especially at low temperatures; the pressure dependence is negligible, so data measured at 1 bar can be used in a wide pressure range, from 0 to several kilobars. Yet in many substances, we see signals in the $C_p(T)$ curve from magnetic and substitutional order/disorder transitions leading to transition peaks (some obvious examples are shown in Fig. 1), but sometimes (especially at very low temperatures) only to minor ‘bumps’ and ‘shoulders.’ C_p also depends to a lesser extent on vacancy defects, dislocations, and effects of crystallinity. The effect of particle size is normally negligible (see below).

The seminal work of Cezairliyan et al. [38] is still a very good reference on the theory of specific heat of solids and their measurement (calorimetry).

$C_p(T)$ is important for thermodynamics and mineralogy/petrology; thus, there is abundant and precise data in the literature for endmember minerals. However, these data are scattered in the literature and often reflect different temperature ranges, methods, and accuracies. There exist excellent collections of C_p and other thermodynamic mineral data (some of them internally consistent) [39–47], but these collections typically only give polynomial $C_p(T)$ interpolation equations for high temperatures ≥ 298.15 K and include either none or rather crude descriptions of transition peaks; they do, however, give citations of the original (i.e., including the low temperature²) data. Therefore, we have undertaken to revise, combine, smooth, and electronically tabulate $C_p(T)$ data for the most important endmember minerals, for a temperature range as wide as possible.

What about the *ab initio*-based prediction of thermodynamic properties like specific heat? This is indeed possible, with the state-of-the-art theoretical techniques like density-functional theory (DFT), density-functional perturbation theory (DFPT) in quasi-harmonic approximation (QHA), combining, for magnetic contributions, with methods like the spin quantum Monte Carlo approach (QMC) for solving the quantum Heisenberg model (suitably mapped), e.g., [48–50]. A number of compounds (elements, oxides, simple minerals) have been calculated with satisfying accuracy (that is, systematic deviations to experimental data less than a few %). Benisek and Dachs [51] provide information about the uncertainties in DFT-calculated C_p 's on a number of well-known minerals; the uncertainties range from less than one % to a few %. For other minerals, see [52]; complex minerals are not a problem in principle, just the computing time gets impractical if Z , the number of atoms in a unit cell, is larger than about 100. Note that there is an issue to transform C_V into C_p : the quasi-harmonic approximation can calculate C_p (not the anharmonic contributions though!) but it is a very time-consuming task. Also, we have little experience concerning the accuracy of magnetic (spin) contributions using QMC and it is unclear how to calculate C_p contributions from other phase transitions. However, for minerals for which no C_p data exist, DFT calculations are really helpful and far better than estimation methods (see Sect. 2.2.1).

2.1 Theory

Heat capacity can be written as the sum of terms: lattice vibrational, Schottky, electronic and magnetic (ferromagnetic and ferromagnetic) contributions, order/disorder, activation (vacancy), and anharmonic contributions [53]. ‘Lattice heat capacity’ is the conventional, but rather colloquial term for the phonon heat capacity (the lattice as a mathematical construct has no heat capacity of its own).

In general, the heat capacity due to lattice vibrations (phonons) can be written as follows:

² Indispensable to obtain 0th-law entropy.

$$C_{V,lattice}(T) = \frac{\partial}{\partial T} \int_0^{\omega_{max}} g(\omega) E \left(\frac{\hbar\omega}{k_B T} \right) d\omega = R \int_0^{\infty} g(\omega) \left(\frac{\omega}{T} \right)^2 \frac{\exp(\omega/T)^2}{[\exp(\omega/T) - 1]^2} d\omega \tag{1}$$

with $g(\omega)$ the DOS (distribution of vibrational states function), ω the circular frequency, k_B the Boltzmann constant, \hbar is Planck’s constant, and E the Einstein oscillator function (oscillator energy times Bose–Einstein distribution with degeneracies 1)

$$E = \frac{\hbar\omega}{\exp\left(\frac{\hbar\omega}{k_B T}\right) - 1}$$

Due to the integral, heat capacity is not very sensitive to the details in the DOS; only at very low temperatures the DOS becomes decisive, while at very high temperatures it has no influence at all.

Lattice heat capacity The theory of Debye [54] is a reasonable approximation for simple, monoatomic, and isotropic crystals (Pb, lead is a famous example). For polyatomic solids, it is only applicable if the following conditions hold (which they usually do not) [55]:

1. The various atoms have nearly equal masses;
2. The coordination environments of the different atoms are nearly identical;
3. The environments are essentially isotropic; and
4. The various near-neighbor interatomic force constants are nearly equal.

Still, one can use the simple and elegant Debye theory and calculate an effective (‘calorimetric’) Debye temperature θ_D that depends on temperature but much less than C_p itself (we discuss this in detail below).

$$C_V = 3n R D(\theta_D/T) \quad [\text{J} \cdot \text{mol}^{-1} \cdot \text{K}^{-1}]$$

$$D(\theta_D/T) = 3 \left(\frac{T}{\theta_D} \right)^3 \int_0^{\theta_D/T} \frac{x^4 e^x}{(e^x - 1)^2} dx = 3 \left(\frac{T}{\theta_D} \right)^3 \int_0^{\theta_D/T} \frac{x^4 e^{-x}}{(e^{-x} - 1)^2} dx$$

$$\theta_D = \frac{h}{2\pi k_B} \left(\frac{6\pi^2 N_A}{ZV} \right)^{1/3} v_m \tag{2}$$

$$v_m \cong \sqrt{\frac{3}{(1/v_p^2 + 2/v_s^2)}}$$

where n is the number of atoms in a formula unit, V is the molar volume, Z is the number of formula units in the unit cell, V_L is the volume of the primitive unit cell, N_A is the Avogadro constant, N is the number of atoms in 1 mol of crystal, k_B is the Boltzmann constant, R is the $R = N_A k_B$, molar gas constant, θ_D is the Debye temperature (‘effective,’ ‘calorimetric’), h is the Planck constant, v_p is the acoustic longitudinal wave velocity, v_s is the acoustic shear wave velocity, v_m is the mean sound

speed, M_r is the molecular mass of the formula unit, α is the isobaric coefficient of thermal volume expansion, and B is the isothermal bulk elastic modulus $=1/\beta$.

For isotropic or cubic crystals,

$$v_p = \sqrt{\frac{K + 4G/3}{\rho}} = \sqrt{\frac{E(1 - \nu)}{\rho(1 + \nu)(1 - 2\nu)}}, \tag{3}$$

$$v_s = \sqrt{\frac{G}{\rho}}$$

where K is the (isentropic) bulk modulus, G is the shear modulus, E is Young’s modulus, ρ is density, and ν is the Poisson’s ratio. Note that for anisotropic crystals, the relationship between sound velocities (in a given direction) and elastic constants (many more than 2) is much more complicated, cf. [56].

Note the second form of the Debye integral $D(\theta_D/T)$ in (2) with $\exp(-x)$ is equivalent but numerically much more robust (avoids overflow).

The low-temperature approximation of the Debye model is the famous $\sim T^3$ law:

$$C_V = \frac{12\pi^4}{5} nN_A k_B \left(\frac{T}{\theta_D}\right)^3, \tag{4}$$

and the high-temperature approximation, Dulong–Petit’s law:

$$C_V = 3nR$$

Actually, the series (Taylor) expansions of the Debye function are, for $T \rightarrow 0$

$$C_V = c_3 \left(\frac{T}{\theta_D}\right)^3 - c_5 \left(\frac{T}{\theta_D}\right)^5 + c_7 \left(\frac{T}{\theta_D}\right)^7 - c_9 \left(\frac{T}{\theta_D}\right)^9 + \dots \tag{5}$$

And for $T \rightarrow \infty$

$$C_V = 3nR \left[1 - \frac{1}{20} \left(\frac{\theta_D}{T}\right)^2 + \frac{1}{560} \left(\frac{\theta_D}{T}\right)^4 - \dots \right] \tag{6}$$

Equation 6 has rather bad convergence properties; modifications have traditionally been used (see chapter 1.2.3), and recently a novel, fast-converging series representation of the Debye function for high temperatures has been proposed [57], where the reciprocal square-root of the Debye function is written as $1 +$ (polynomial with only even powers of T).

The point of inflection of the Debye curve, C_V vs. T , is at $T \approx \theta_D/6.1$. At this point, $C_V = 0.7713675nR$. The maximum of the curve C_V/T is at $0.27985645 \times \theta_D$ which is useful to quickly estimate the Debye temperature of a solid if θ_D is constant (which is, unfortunately, almost never the case for minerals).

The Einstein model [58] is given by

$$C_V(T) = 3nR \cdot \left(\frac{\Theta_E}{T}\right)^2 \cdot \frac{\exp\left(\frac{\Theta_E}{T}\right)}{\left[\exp\left(\frac{\Theta_E}{T}\right) - 1\right]^2} \quad (7)$$

with Θ_E the Einstein temperature. The Einstein model is unphysical for low temperatures T_0 , but useful as a reasonable approximation for the lattice heat capacity of optical vibration modes at high temperatures.

In some cases, other vibrational c_p contributions are observed, for example, by hindered rotations, inversion vibrations, etc. (e.g., in ammonia NH_3); often in molecular solids, polymers and complex organic substances, see, for example [59]. Note that in polymeric science, where often linear chains of molecules dominate the vibrational modes, the 1-dimensional Debye function is often used [e.g., 60].

Coming back to silicate minerals, Kieffer [61–63] developed a more sophisticated theory which captures the main features of the vibrational spectra encountered in non-simple solids. It proposes a vibrational spectrum consisting of three acoustic branches, an optical continuum, and optional Einstein oscillator(s). This theory contains up to 25 parameters; it is, however, independent of calorimetric data and not obtained by any fitting procedure. Kieffer's theory is useful—if measurements are not available—for the prediction of lattice heat capacities of structurally complex rock-forming minerals from their elastic constants and spectroscopic data. The parameters are given by elastic, crystallographic, and spectroscopic (infrared and Raman) data only, which are used to define upper and lower limits of the various vibrational branches. Its accuracy, if compared to accurate experimental data, is typically 30 % to 50 % below 50 K, 5 % at 300 K, and 1 % at 700 K; fitting of ill-determined spectroscopic parameters by calorimetric data can improve the low- T accuracy significantly. The theory, however, cannot model any anomalies (Schottky anomalies, electronic and magnetic contributions, transitions) and neglects the effects of thermal expansion (the spectrum is referred to the volume V at 0 K), defect/domain/surface contributions and, perhaps most significantly, anharmonic effects. All these effects are usually small in the temperature range $10 \text{ K} < T < 500 \text{ K}$. At high temperatures, when the details of the lattice vibration spectrum are not so important, often a single Einstein oscillator term (corresponding to the Si–O stretching mode) suffices to fit silicate c_p data (to the order of 1 % at 700 K).

A variant of Kieffer's lattice dynamics model using vibrational density of states for constructing thermodynamic databases is given by [64]. This model is computationally much simpler and faster than the Kieffer model, it models the vibrational density of states by the sum of (a large number, ~ 60) monochromatic Einstein frequencies and adds models for the dependence on volume of the Einstein temperatures, an equation of state for the static lattice contributions and a free-electron gas model for the electronic contribution. It allows to predict also thermal expansion and anharmonicity [65] of minerals; the main input are data (infrared, Raman, inelastic neutron scattering) on the vibrational DOS.

There is an established alternative theoretical model for the lattice heat capacity, that of Komada and Westrum [66, 67] which is somewhat complex mathematically (discussed in [68]). This model needs also a number of input parameters from

chemical and crystallographic data, besides a (nicely constant) characteristic temperature θ_{KW} , and similarly to the Kieffer model does not describe any peaks and anomalies.

The relation between C_V and C_P from thermodynamics is

$$C_P - C_V = TV\alpha^2 B = TV\alpha^2 / \beta, \quad (8)$$

where $\alpha = \frac{1}{V} \left(\frac{\partial V}{\partial T} \right)_P$ is the isobaric coefficient of thermal volume expansion, $V(T)$ the molar volume, B the isothermal bulk modulus, $\frac{1}{B} = \beta = -\frac{1}{V} \left(\frac{\partial V}{\partial P} \right)_T$ the isothermal compressibility.

All quantities are temperature-dependent.

The pressure dependence dC_P/dp is negligible for most minerals at pressures up to thousands of bars. As an example, for periclase (MgO), the maximum relative sensitivity $dC_P/dp/C_P$, at ~ 70 K, is about $3E-6/\text{bar}$, thus reaching 1 % at pressures of 3000 bar or more. For forsterite, Chopelas [69] finds dC_V/dp of $4.98E-5 \text{ J}\cdot\text{mol}^{-1}\cdot\text{K}^{-1}\cdot\text{bar}^{-1}$ at 298 K or, in relative terms, $4e-7/\text{bar}$ or reaching 1 % at 23 kbar. See [70, 71] for extensive information on the pressure dependence where it matters (e.g., in the Earth's mantle).

Anharmonicity On top of the effects of thermal expansion ($C_V C_P$), the anharmonicity of lattice vibrations typically increases even C_V beyond the Dulong–Petit limit at high temperatures; the anharmonicity of forsterite, fayalite, and periclase has been discussed by Anderson and Suzuki [72]. Anharmonicity in general is covered in [38, 65, 73–75]. For example, C_P of feldspars ($n=13$) at 1400 K [42] is between 330 and $346 \text{ J}\cdot\text{mol}^{-1}\cdot\text{K}^{-1}$, where $3Rn = 324.26 \text{ J}\cdot\text{mol}^{-1}\cdot\text{K}^{-1}$ would be the predicted limit for C_V . Forsterite has a high intrinsic anharmonicity, where even C_V exceeds the Dulong–Petit limit for $T > 1550$ K [76].

Electronic heat capacity occurs in conductors with free electrons, thus mostly in metals (Fe, Ni) but also in, e.g., in graphite and pentlandite (Fe, Ni)₉S₈ [77, 78]. It is a small effect only relevant at low temperatures. The usual low-temperature limit [79] is given in the free-electron approximation by (T_f : Fermi temperature, calculated with the number density and effective mass of the valence electrons)

$$C_{V,el} = \frac{\pi^2}{2} k_B \left(\frac{k_B T}{E_f} \right) = \frac{\pi^2}{2} k_B^2 \left(\frac{T}{T_f} \right) = \gamma T. \quad (9)$$

Various refinements valid for higher temperatures exist, e.g., [79] but deviations of a simple linear T -dependence are usually negligible. A different electronic heat capacity stems from electronic excitation from the ground state (energy set to 0, degeneracy g_0) to higher energy levels (degeneracy g_i ; T_Δ is the energy difference expressed in Kelvin) and is usually called *Schottky-type heat capacity*. It has the form of a very broad asymmetric peak [53, 80, 81] which falls off $\propto 1/T^2$ at temperatures higher than the peak temperature.

For a two-level system the Schottky heat capacity is

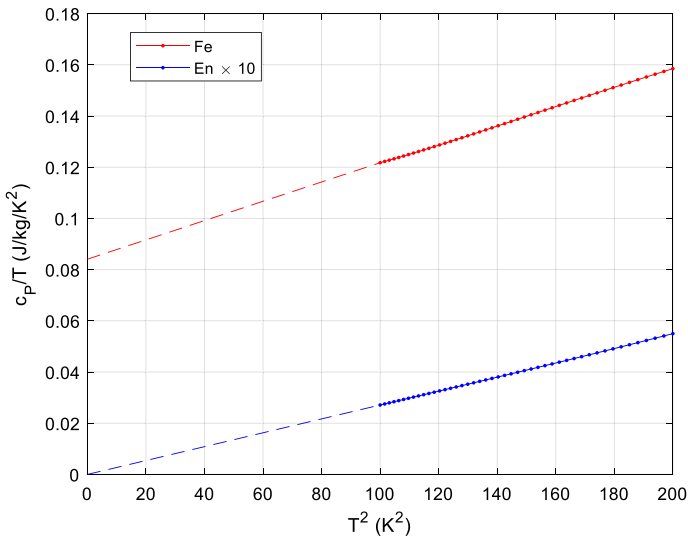


Fig. 2 Plotting c_p/T versus T^2 for low temperatures, less than about 15 K, gives straight lines for most solids; the slope is $\propto 1/\theta_D^3$, and extrapolation to 0 K gives directly γ , the electronic heat capacity term, while for Debye solids it is zero. Low-temperature anomalies (e.g., Schottky) also show up clearly. Smoothed c_p data of our database have been used

$$C_{e,sh} = R(g_0/g_1) \left(\frac{T_\Delta}{T} \right)^2 \frac{\exp(T_\Delta/T)}{[1 + (g_0/g_1) \exp(T_\Delta/T)]^2}.$$

Realistic systems often involve several transitions with various degeneracies, usually at very low temperatures, e.g., [82] for fayalite. Note that the peak temperature of the Schottky bump is of the order of $(0.3\text{--}0.4)T_\Delta$ and its magnitude is of order $\sim 0.2R$ to $\sim 0.8R$, depending on the degeneracies, not on temperature; at very low temperatures, this can be a significant or even the dominating (in case of nuclear terms) contribution to heat capacity.

Note that a linear term in c_p (at low $T \ll 100$ K) not necessarily stems from conduction electrons, but could also be caused by lattice vacancies [83].

It is customary to plot low-temperature c_p/T vs. T^2 ; obviously, cubic (Debye) and linear (electronic or glass anomaly) terms can then be easily determined from extrapolating a linear fit to zero K, see the example in Fig. 2.

Anomalies in glasses and gels Glasses have a c_p anomaly at low temperatures (and a glass transition c_p anomaly, basically a step, at the high-temperature glass transition temperature T_g which is typically at a much lower temperature than the melting temperature of the crystalline phase). T_g for silicate minerals depends strongly on water content [84].

The low-temperature anomaly of glasses consists of an extra c_p contribution, about linear in T ($\propto T^{1+\delta}$), but vanishing at high $T >$ about 30 K (*au contraire* to electronic heat capacity). See the glass Sect. 2.15 for details.

Table 1 Limiting cases at low temperatures $T \rightarrow 0$ K, from [38]

$C_V = \beta T^3$	Lattice vibrations only, isolators
$C_V = \beta T^3 + \gamma T$	Non-magnetic conductors, glasses (approx.)
$C_V = \beta T^3 + \gamma T + \delta T^{3/2}$	Ferromagnetic and ferrimagnetic
$C_V = \beta T^3 + \delta T^{3/2}$	Ferrimagnetic
$C_V = \beta T^3 + \gamma T + \delta T^3$	Antiferromagnetic
$C_V = \beta T^3 + \eta/T^2$	Nuclear (2-level, $> 10^{-3} \dots 10^{-2}$ K)

Activation heat capacity At high temperatures, especially for substances with a high melting point, lattice monovacancies can have a marked effect on c_p , e.g., for tungsten > 1000 K [85]. This effect can be mixed with the ‘premelting’ increase in heat capacity caused by impurities (see below).

Magnetic (ferromagnetic and ferromagnetic) and order/disorder transitions are discussed in more detail below. They are generally very difficult to model precisely. They usually produce transition peaks in the $C_p(T)$ curve that can be very dominant (compare Fig. 1). For the magnetic contributions, at least limiting cases for $T \rightarrow 0$ can be given (Table 1).

Nuclear contribution to the specific heat can become significant below ~ 1 K in certain compounds, depending on isotopic composition and dependent on external magnetic fields, e.g., [38, 86]. It is typically a Schottky peak at ~ 0.01 K; below this peak temperature, nuclear contribution tends to 0, at high temperatures it varies as $\sim 1/T^2$.

More theoretical background, in particular for low temperatures and ‘heat capacity anomalies’ can be found in [87, 88].

2.1.1 Mixing Model

Except (presently) for Olivine (see below), we use a simple mechanical mixing model for astro-materials composed of endmember minerals:

$$C_p = \sum_i X_i C_p^{(i)},$$

$$c_p(T) = \sum_i w_i c_p^{(i)}(T) \quad (10)$$

with X_i the mole and w_i the mass fractions of the constituents, $\sum X_i = 1$, $\sum w_i = 1$, and $C_p^{(i)}$ are the heat capacities of the endmembers. This model is exact for mechanical mixtures and for ideal solid solutions of endmember minerals (without interactions); deviations for solid solutions are discussed next.

2.1.1.1 Solid Solutions and the Excess Heat Capacity of Mixing Many minerals form solid solution series (‘joins,’ in the jargon). Their c_p is only ideally given by the linear combination of endmember c_p with the endmember mass fractions as coefficients

(mole fractions of endmembers for C_p). For detailed background, theory and experimental, see e.g., [89].

However, non-idealities exist. The definition [89] of the non-ideality of C_p , called *excess heat capacity* of mixing, is ('real minus ideal')

$$\Delta C_p^{ex} = C_p^{solid\ sol.} - \sum C_p^{(i)} X_i,$$

where $C_p^{solid\ sol.}$ is the heat capacity of the solid solution, $C_p^{(i)}$ are the heat capacities of the endmembers and X_i are the corresponding mole fractions. Usually, measured excess heat capacities are used to compute the excess entropy S^{ex} and modeled (at STP, 298.15 K) as function of composition. This done, the $\Delta C_p^{ex}(T)$ cannot be derived anymore. Rather, the measured data have to be used to calculate temperature-dependent Margules parameters, e.g., for a binary mixture: $C_p^{mix}(T) = (1 - X_2)C_p^1(T) + X_2C_p^2(T) + X_2^2W_{12}(T) + (1 - X_2)^2W_{21}(T)$ or the Margules formulation for an asymmetric ternary solution [90] which has 7 Margules parameters, 6 $W_{ij}(T)$ parameters and $W_{123}(T)$.

Olivines, feldspars, and pyroxenes are the most abundant rock-forming minerals, thus it is desirable to know the excess heat capacities for their solid solutions. At present, we can do that only for olivine, a mixture of the two endmembers forsterite and fayalite, where the excess heat capacity is well characterized. For other minerals, there is a dearth of data on excess heat capacities, so we mostly ignore the deviations from ideal, (or mechanical) mixtures. This leads to uncertainties, which are negligible at high temperatures (> 300 K), and possible systematic deviations from the mechanical mixing model in the low-temperature range for some solid solution series. Maximum excess heat capacities found [89] are, e.g., $\sim 25\%$ at 40 K for grossular–pyrope, $\sim 10\%$ at 40 K for analbite–sanidine, $\sim 3\%$ at 400 K for annite–siderophyllite; $\sim 50\%$ at 10 K for bronzite (Fe-poor orthopyroxene) but negligible > 65 K [91, 92], $< 2\%$ for feldspars between 10 and 800 K [90, 93, 94].

For olivine (Fo/Fa solid solutions), [95] measured a significant excess heat capacity, but only near the magnetic transition at 35 K to 70 K. Since these data cover the whole composition range of olivines in sufficiently small increments (Fig. 3), we are able to 2D-interpolate the c_p of the solid solutions accurately. Thus, for olivines of known Fo/Fa composition, the database gives the accurate c_p directly. A 2D interpolation (table lookup) is used to obtain c_p values for fayalite concentrations $0 < X_{Fa} < 1$ and $T < 300$ K and a mechanical mixing model for $300 < T < 1400$ K where the excess heat capacity in olivines is negligible.

There are data on the excess heat capacities of feldspars and pyroxenes [90, 93, 94, 96–98], but they are presently difficult to model due to the up to 4-dimensional compositional range. For Fe–Ni alloys, the enthalpy of mixing is small since the two metals are very similar. However, the temperatures and amplitudes of the magnetic and structural transition lambda peaks > 600 K change drastically with composition (see Fig. 10). Our database currently employs the curve for a standard Fe/Ni ratio for all temperatures and a real mixing model for olivine; it is planned to give at least approximate real mixing models for idealized feldspars and pyroxenes in the future, i.e., for idealized anorthoclase (alkali) Ab–Or and plagioclase Ab–An feldspars and for idealized orthopyroxenes En–Fs and clinopyroxenes Di–Hed.

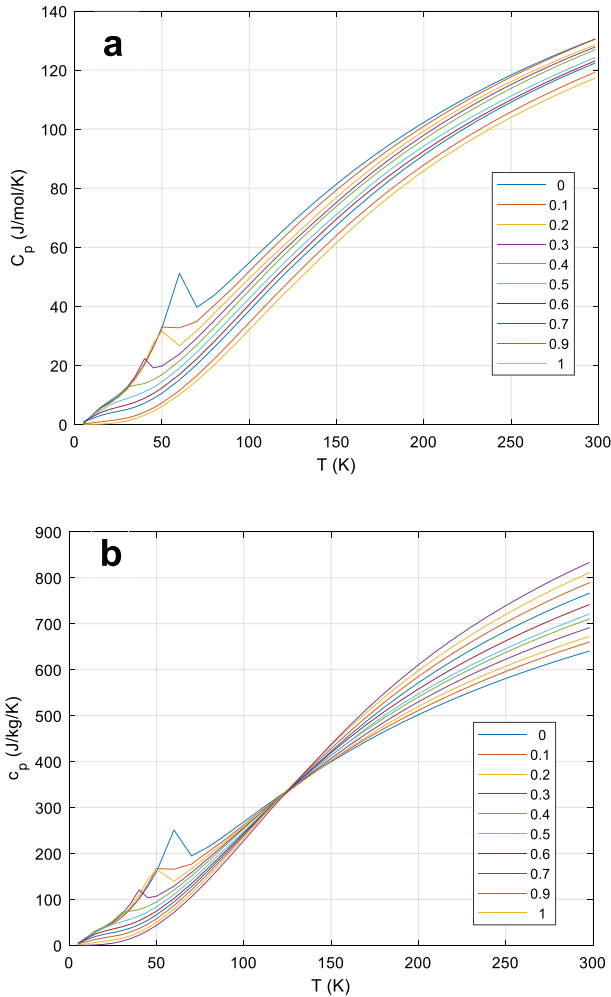


Fig. 3 The C_p (upper panel, **a**) and c_p (lower panel, **b**) of olivines, after [95]. Note the X-point at ~ 125 K, where all compositions have about the same mass-based specific heat, which is not the case in the molar C_p . This is a quite natural effect of the vastly different formula weights of fayalite (203.778) and forsterite (140.693). Parameter in legend: x_{Fo} , mole fraction forsterite ($w_{Fo} = x_{Fo} \times 140.693 / (203.778 - 63.085 \times x_{Fo})$). Higher-resolution data around the transition peaks not shown for clarity

So, what accuracy can be expected for the $c_p(T)$ of an astro-material of given mineral composition, if accurate endmember mineral's $c_p(T)$ are in the database? We have indications that the remaining uncertainty is very low at high temperatures, e.g., [99] could reproduce the measured c_p of 4 'standard rock samples' from 300 K to 1000 K with a standard deviation of about 1 % if calculated from mineral compositions. For very low temperatures, if there are solid solutions (not olivine, which we already treat as non-ideal mixture) with a high excess heat capacity the few examples given above suggest a *maximum* relative deviation, outside or near c_p anomalies,

of ~25 % [89] or ~50 % at 10 K to 40 K, decreasing rapidly for $T > 65$ K, and for transition peaks (if seen at all in the $c_p(T)$ curve) a possibly significant change in peak temperature and amplitude.

Note that even for laboratory samples, the uncertainties of chemical analysis³ (for normative mineral composition) and especially the uncertainties of modal analysis⁴ are typically of the order of a few % even for major constituents; of the order of 10 % or more for minor constituents. This translates, already, into a few % uncertainty in c_p on average; for less well-known astro-material, it follows that the uncertainties stemming from compositional uncertainty are usually more significant than those from the non-ideality effects of $c_p(T)$ in solid solutions.

An example: bronzite Bronzite is Fe-poor orthopyroxene (hypersthene) and its c_p should thus be a linear combination of En and Fs. Krupka et al. [91, 92] have measured its c_p from 5 to 1000 K. The sample is a natural crystal of idealized composition $\text{Mg}_{0.85}\text{Fe}_{0.15}\text{SiO}_3$. ($x=0.15$ Fe, $1-x=0.85$ Mg).

It turns out that the nominal c_p calculated with $x=0.15$ and the ideal molar mass, $M=105.120$ g·mol⁻¹ (corresponding to $\text{Mg}_{0.85}\text{Fe}_{0.15}\text{SiO}_3$) already matches very closely (better than ± 1 %) the data except below ~100 K where the broad Fs transition peak occurs at 38 K, but the corresponding Bronzite peak (actually only a Schottky bump) is shifted to ~12 K (see Figs. 4 and 5). A free fit of the composition (Mg and Fe only), with temperatures < 100 K excluded from the fit, results in a slightly better agreement of measured and calculated C_p (0.25 % less bias, overall agreement mostly better ± 0.5 %) and returns compositions entirely consistent with the chemical analysis and its inherent uncertainties. For supporting data and figures see Online Appendix, Sect. 6.

We conclude that non-ideal mixing is negligible (< 1 % effect similar to experimental uncertainties) here for $T > 100$ K but significant (up to ~60 %) at certain very low temperatures, near 12 K and near 38 K, but only due to the change of the magnetic/Schottky-transition peaks at low temperatures with composition.

2.1.2 Polymorphs and Phase Transitions

Polymorphism is the ability of a mineral to exist in more than one form or crystal structure. Different polymorphs can have slightly differing $C_p(T)$ and there may be a peak in C_p at the phase transition temperature, where the low-temperature form transforms into the high-temperature structure.

There are three main types of *structural* phase transitions [e.g., 106]:

³ The relative 1- σ uncertainty of a mass fraction p in chemical analysis is about $\sigma(p)/p \approx 0.25 \exp(-5\sqrt{p})$, correlating data of [100–103]. This reflects the state-of-the-art ca. 1950 to 1985, combination of atomic absorption spectroscopy and standard wet-chemical techniques [104]. Nowadays, uncertainties are much smaller.

⁴ Was generally point counting of thin sections, with significant statistical uncertainties of the order of 20 % (relative) [105] depending much on component abundance, number of points counted. Potentially much more depending on the homogeneity of the sample, i.e., the representativeness of that thin section. No one does it anymore that way so those old analyses will stand forever. Newer SEM X-ray mapping techniques are probably not as good.

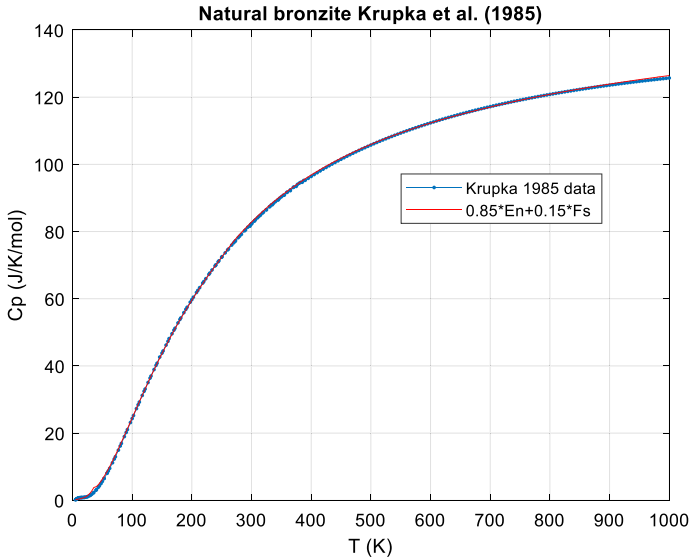


Fig. 4 Bronzite [92], data and ideal c_p calculated for ideal composition

- Reconstructive (metastable at low T , since they require diffusion)
- Order–disorder (metastable at low T , since they require diffusion)
- Displacive (instantaneous, since they only require a distortion of the lattice)

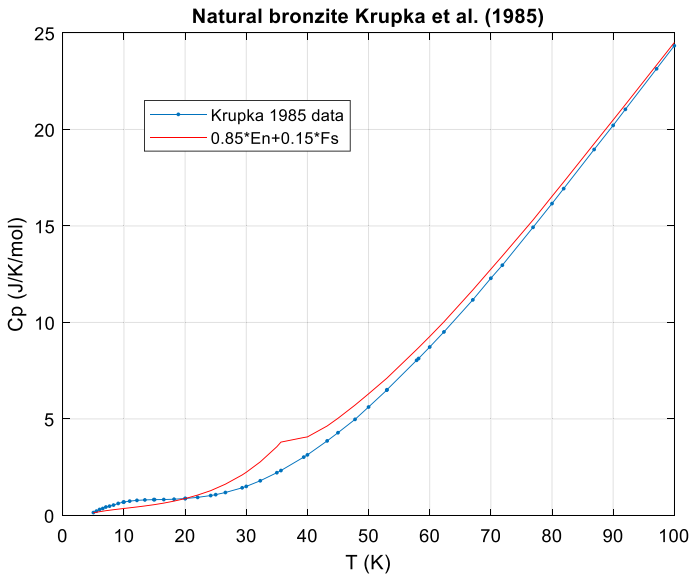


Fig. 5 Bronzite [92], low T , data, and ideal c_p calculated for the ideal composition. The F_s transition at 38 K and the Schottky peak of bronzite near 12 K do not scale linearly

The rate of solid diffusion required for reconstructive and order–order phase transitions follows approximately an Arrhenius equation, $\propto \exp(-E/RT)$ with E the activation energy. To give an example, for the Al/Si disorder rate in albite and microcline, activation energies between 280 and 360 kJ·mol⁻¹ have been determined and a 50 % transformation time of 5 days at 1050 °C [107]. From this it can be estimated that below ~400 °C, the phases are ‘frozen in’ over timescales comparable with the age of the solar system (4.5 Ga).

For other atoms in solids, much lower activation energies of the order of ~60 kJ·mol⁻¹ have been determined. The atomic migrations of Al and Si in feldspars are probably slower than those of any of the other major ions, including oxygen, at least when water is present [108]; hence the migrations of these species may be rate limiting for a number of processes in feldspars. There are no data for Al or Si diffusion in feldspar because the rates are so slow, but studies of Al–Si order–disorder kinetics are one way to get at this problem [107]. For the coupled substitution (Na,K) + Si = Ca + Al, where the tetraeder system is involved, a diffusion coefficient of 10⁻²² cm · s⁻¹ at 800 °C has been determined [109, 110].

There are also high-pressure polymorphs of minerals, e.g., for forsterite,⁵ wadsleyite, and ringwoodite which have been reported from shocked meteorites. Depending on the cooling history, both high-temperature and high-pressure modifications, although metastable, can remain ‘frozen in’ for billions of years.

Phase transitions can also be caused by (or coupled to) magnetic effects [112, 113]; other transitional behavior includes Verwey, Jahn–Teller, metal–insulator, superconductivity, electrical, plastic, and ‘crystalline liquid’ phenomena that show up as anomalies in the $C_p(T)$ curve [38, 114–117].

2.1.2.1 Modeling of Phase Transitions The most commonly adopted thermodynamic classification of phase transitions still follows the Ehrenfest [118, 119] terminology, by assigning the order of the transition appropriate to the order of the derivative of the Gibbs function (with P or T) showing a finite discontinuity. A 1st-order phase transition (1-O) is characterized by a latent heat (=energy is absorbed or released by a substance during a change in its physical state without changing its temperature). The fact that the temperature is not changed during the 1-O phase transition causes C_p to go to infinity (theoretically). The explanation for the presence of the latent heat is that chemical bonds are broken during the (heating) transition (melting of a crystal, vaporizing of a liquid) and this is responsible for the absorption of energy without increasing the temperature, thus, a vertical jump of enthalpy at the transition temperature T_c , thus $C_p(T_c) = \infty$ (but with a finite integral = phase change enthalpy ΔH). A simple 1-O phase transition ideally produces a δ -peak in C_p ; experimentally, due to non-zero thermal homogeneity, the peak has always a finite width ϵ , order of 1 K. This can be described by the Gaussian approximation to the Dirac δ -function, $\Delta C_p(T) = \frac{\Delta H}{\sqrt{2\pi\epsilon}} \exp(-[T - T_0]^2/2\epsilon)$.

⁵ Mg₂[SiO₄] is trimorph, α =forsterite and high-pressure phases (metastable at low pressure; usually shocked but not melted forsterite), ringwoodite (γ -(Mg,Fe)₂[SiO₄]) and wadsleyite (β -(Mg,Fe)₂[SiO₄]). Small differences of the $C_p(T)$ curves (α,β,γ) have been measured by [111]

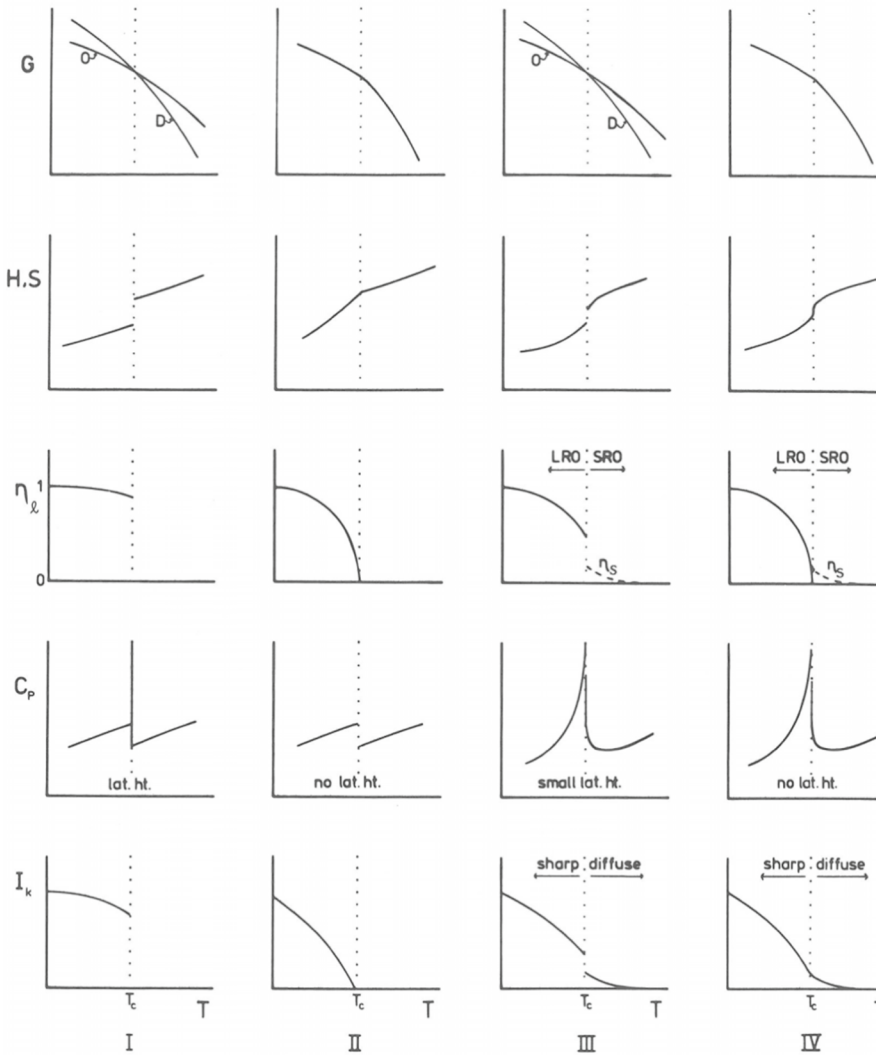


Fig. 6 After [127] Schematic form of the principal thermodynamic parameters through a phase transformation at T_c . Column I=first order; column II=second order; column III= λ transformation with a small first-order break at T_c ; column IV= λ transformation with no first-order break. G=free energy, H=enthalpy, S=entropy, η_l =long-range order parameter, η_s =short-range order parameter describing precursor ordering above T_c ; C_p =specific heat; I_k =integrated intensity of a superlattice reflection. D=disordered state, O=ordered state. LRO=long-range order, SRO=short-range order. Volume is not shown, but must be continuous or discontinuous in some manner analogous to H and S

The Ehrenfest higher-order transitions have received much evolution since 1933 [118]. It became clear that not only the existence of discontinuities in thermodynamic derivatives but also the actual nature of the discontinuity of the m th derivative of the Gibbs free energy at the transition point is important, whether, for example, c_p appears to go to infinity at the transition point or is merely one which is finite

but very large [120–125]. See Fig. 6 for a schematic overview. 1st-order transitions (other than melting) are rare in minerals (Quartz probably) as are strictly 2nd-order transitions; most are ‘in-between.’

Summarizing, phase transitions other than first order [called second order (2-O) or, maybe better, continuous] including tricritical phase transitions [126] are less well understood and rarely analytically tractable. A strictly 2nd-order phase transition has no latent heat and hence C_p does *not* go to infinity. It describes displacive phase transitions without breaking chemical bonds. This is also true for magnetic phase transitions (magnetic ordering gives rise to a distortion of the lattice).

Transitions with finite discontinuities in specific heat at a definite transition temperature (classical 2-O) are extremely rare [106]. Phase transitions which are not 1st order, yet which show (probably) infinite heat capacity, are called λ -transitions, with no or small first-order break at T_c [127], see also the provocative papers by Mnyukh [128, 129]. The heat capacity of the system increases (coming from $T < T_c$) long before the critical temperature T_c and typically falls off much faster. Examples are order/disorder transitions in alloys or solid solutions, ferromagnetism, and the transition from liquid to superfluid helium. A famous example is ammonium chloride, NH_4Cl . Lambda (λ) transitions are very common and may be distinguished from classical second-order (2-O) phase transitions in that heat capacity C_p (not C_v) tends toward infinity as the transition temperature is approached. Some transitions are ‘mixed’ or ‘superimposed’ as, for example, the ferroelectric transition in KH_2PO_4 (KDP) at about 122 K is mixed displacive and order–disorder with one transition triggering the other [106].

A very careful analysis of the lambda transition in quartz is given by [130].

Lambda transitions can often be treated in the framework of the Landau theory [131, 132]:

$$C_p(T) = C_{p,L}(T) + \begin{cases} \frac{a^{3/2}}{4c^{1/2}} \frac{T}{\sqrt{T_d - T}}; & T < T_c \\ 0; & T > T_c \end{cases}$$

Here, $C_{p,L}$ is the lattice heat capacity, T_c is the temperature for which the experimental specific heat curve has the maximum value, and T_d is the metastability limit on cooling, a, c , are constants.

Long-range correlations and fluctuation effects can be semi-empirically modeled (‘critical exponents’), by an additive term C_λ [95, 133, 134],

$$C_\lambda(\varepsilon) = \begin{cases} A' \varepsilon^{-\alpha'}, & T < T_c \\ A \varepsilon^{-\alpha}, & T > T_c, \end{cases}$$

$$\varepsilon = |T - T_c|/T_c$$

where the critical exponents α, α' can be slowly varying functions of (reduced) temperature ε or $\log(\varepsilon)$. Note that fits usually give slightly different T_c, T_c' , for the portions above and below the peak.

Dachs et al. [135] applied the C_λ model successfully to the magnetic phase transition of almandine. Some compilations of mineral thermodynamic data (e.g., [40]) represent transition peaks either with Landau parameters or with the parameters of

the Bragg–Williams theory (see [136, 137]). Improved theories for ferro- or antiferromagnetic transitions are available [138, 139].

The heat capacity behavior related to a phase transition depends on the degree of crystallinity of the crystal (e.g., the concentration of imperfections), is rate-dependent, and has hysteresis.

Thus, the shape of the corresponding peak is very likely sample dependent (impurity content, grain size) and whether the temperature is raised or lowered through T_c and how fast [140]. The so-called Verwey transition in magnetite near 125 K is an example of a displacive structural transition coupled to a magnetic phase transition. The temperature and shape of the Verwey transition peak are highly sensitive to the stress state of magnetite and to the stoichiometry; non-stoichiometry in the form of metal cation substitution or partial oxidation can lower the transition temperature or suppress it entirely. Similarly, in wüstite, Fe_{1-x}O (a classical example of a non-stoichiometric phase) the antiferromagnetic/displacive lambda peak near 190 K is strongly composition dependent [141, 142].

2.2 Useful Approximations

2.2.1 The Neumann–Kopp Rule and Estimation Models

The so-called Neumann–Kopp rule is just stating the obvious, namely, that heat capacities of mixtures are additive and that C_V scales with n , the number of atoms per formula unit, and c_V (and c_p) scales with n/M_r , thus with $1/\bar{A}_r$; \bar{A}_r is the average atomic mass of the elements involved, $\bar{A}_r = M_r/n$. The \bar{A}_r of silicates is of the order of 20 $\text{g}\cdot\text{mol}^{-1}$, which explains why meteoritic iron ($\bar{A}_r \approx 56 \text{ g}\cdot\text{mol}^{-1}$) has a c_p about half of the C_p of silicates. It also explains that per unit of mass, heat capacity is rather similar in all rocks, while the molar heat capacity can assume rather high values if n is high.

The approximate scaling of c_p with $1/\bar{A}_r$ is very useful to estimate the specific heat of a mineral that is not in the database, but an isostructural mineral with similar composition is extension: principle of corresponding states (see, e.g., in [92]).

The additivity is used for the subtraction of impurities (secondary phases) from experimental c_p data [e.g., 143] and for deviation from endmember stoichiometry [144, 145]:

$$c_{p,\text{miner}} = \frac{c_{p,\text{sample}} - \sum_i x_i c_{p,i}}{x_{\text{miner}}},$$

where x_{miner} is the mass fraction of the mineral, $c_{p,\text{sample}}$ the heat capacity of the sample, x_i the mass fraction of impurity i , and $c_{p,i}$ the heat capacity of impurity i , all in $\text{J}\cdot\text{kg}^{-1}\cdot\text{K}^{-1}$.

The Neumann–Kopp rule is also invoked to roughly estimate the heat capacity of compounds from known heat capacities of constituent compounds [114], e.g., $C_p(\text{MgAl}_2\text{O}_4) \approx C_p(\text{MgO}) + C_p(\text{Al}_2\text{O}_3)$. Leitner et al. [73] discuss the extensions to the empirical Neumann–Kopp rule, a combination of an additive and a

contribution method to estimate the heat capacity of complex compounds. See also [146, 147].

Indeed, several schemes have been devised to estimate the thermodynamic properties of minerals for which they are unknown. These models are all based on the premise that the thermodynamic properties of minerals can be described as a stoichiometric combination of the fractional properties of their constituents: $X = \sum n_i x_i$, where X is the property of interest, x_i are the fractional properties of each constituent, and n_i are the stoichiometric amounts of that constituent in the mineral. Different building blocks are used in the models ranging from elements [148], oxides [45, 149], isostructural minerals [150] to elements in their respective crystallographic coordination (the polyhedron method [151–153]) and other schemes [154]. Up to now, all these models have been made only for the high-temperature range, ≥ 298 K (interesting for terrestrial geophysics), the temperature dependence conveniently cast into one of the usual polynomial representations (see Sect. 2.2.3). However, it should also be possible to extract a $C_p(T)$ polyhedron-‘kit’ from the many existing low- T data, or the $C_p(T)$ of ‘exchange vectors,’ i.e., the change of C_p by substitution from a well-known (or DFT-calculated) endmember. To the best of our knowledge, this has not been done (or tried) yet.

If there are no experimental c_p data for a particular mineral, all these estimation methods are certainly better than nothing; the crux is that the a priori uncertainty of the predicted c_p values is rather unpredictable.

2.2.2 Modeling C_p – C_v

The relative difference of C_p and C_v is usually, for silicates, of the order of < 1 % below room temperature, and of the order of 4 % at 700 K. The part due to thermal expansion can be modeled [76, 155, 156], eqn., if the thermal volume coefficient of expansion α , bulk modulus $B = 1/\text{isothermal compressibility}$ are known as a function of temperature.

A perfect knowledge of α and B is still not sufficient to calculate C_p – C_v exactly, because of the additional contribution of the anharmonicity which has the approximate form $c_{p,anh} = c_{p,harm}(1 + aT)$ (crude average over all vibrational modes, see [74, 157]).

In practice, after [158–163], we write

$$\begin{aligned} C_p &= C_v(1 + \alpha(T)\gamma_G T) \quad \text{or, since } \alpha\gamma_G \propto C_p, \\ C_p - C_v &= AC_p^2 T, \\ C_p &= \frac{1 - \sqrt{1 - 4ATC_v}}{2AT} \end{aligned} \quad (11)$$

with γ_G the thermodynamic Grüneisen parameter [164]. A and γ_G can be taken as approximately constant, over a wide range of temperatures $T > \theta_D$ (for $T < \theta_D$ $C_p - C_v$ is, fortunately, usually small). The second formula is known as the Nernst–Lindemann relation. The unit of A is $\text{mol}\cdot\text{J}^{-1}$ (or $\text{kg}\cdot\text{J}^{-1}$, for c_p).

Table 2 Common high-T polynomial fit equations for C_p

$C_p = a + bT + \frac{c}{T^2}$	(1) Maier and Kelley (1932)
$C_p = a + bT + \frac{d}{T^{1/2}}$	(2) Chipman and Fontana (1935)
$C_p = a + bT + \frac{c}{T^2} + \frac{d}{T^{1/2}} + eT^2$	(3) Haas and Fisher (1976) and Robie (1978)
$C_p = k_0 + \frac{k_{0.5}}{T^{1/2}} + \frac{k_2}{T^2} + \frac{k_3}{T^3}$	(4) Berman and Brown (1985)
$C_p = k_0 + bT + \frac{k_1}{T} + \frac{k_2}{T^2} + \frac{k_3}{T^3}$	(5) Fei and Saxena (1987)
$C_p = k_0 + k_{ln} \ln T + \frac{k_1}{T} + \frac{k_2}{T^2} + \frac{k_3}{T^3}$	(6) Richet and Fiquet (1991)
$C_p = a + bT + \frac{c}{T^2} + \frac{d}{T^{1/2}}$	(7) Holland (1981)

The various empirical equations are commonly known by the author/date citations in the table. The numbered references for each are given in the table footer

(1) [167], (2) [168], (3) [42, 169], (4) [45], (5) [166], (6) [170], (7) [171]

Parameter A may be crudely estimated from melting temperature T_m by [165] $A \approx 1 \times 10^{-10} [\text{mol}^{-1} \cdot \text{J}^{-1} \cdot \text{K}^{-1}] T_m [\text{K}]$. If data on the thermal expansion coefficient and compressibility at one temperature $T \rightarrow 0$ are available, A may be calculated as

$$A \cong \frac{V(T_0)\alpha(T_0)^2B(T_0)}{C_p^2(T_0)}$$

Alternatively, A can be estimated from high-temperature C_p data alone, by invoking the empirical constraint that the effective Debye temperature \approx constant at the highest temperatures $\gg \theta_D$. This A then also includes the effects of anharmonicity in an approximate way.

2.2.3 Polynomial Expressions for c_p at High Temperatures

Various empirical polynomials are in use (see Table 2), they have been discussed by [45], see Table 3. They all diverge for

$$T \rightarrow 0$$

and are only useful for $T > 100$ K to 300 K and only if no transition peaks appear in the fitted range.

Fei and Saxena [166] recommend a semi-empirical expression $C_p = 3Rn(1 + k_1T^{-1} + k_2T^{-2} + k_3T^{-3}) + (A + BT) + \Delta C_p$.

R and n are the gas constant and the number of atoms in the chemical formulae, respectively. A and B are calculated from thermal expansion coefficient and isothermal bulk modulus data. The k_i are determined by fitting the measured low-temperature heat capacity data. ΔC_p is the departure from the $3Rn$ limit for some substances due to anharmonicity, and possibly electronic contributions or cation disordering.

Equation 7, by Holland [171], retains the extrapolatory merits of the Maier–Kelley equation while allowing superior representation of the measured heat capacities. However, the added flexibility of such a polynomial requires that one or two dummy

Table 3 Summary of the merits of C_p equations [75, 76]

	Eq. 1	Eq. 3	Eq. 4	Eq. 5	Eq. 6
Reference	[167]	[42, 169]	[45]	[166]	[170]
Representation of measurements	Mediocre	Excellent	Good	Excellent	Excellent
Low-temperature extrapolation ^a	Good	Mediocre	Bad	Bad	Bad
High-temperature extrapolation of DSC measurements	Bad	Bad	Mediocre	Mediocre	Mediocre
Drop calorimetry data up to 1800 K	Mediocre	Bad	Good	Good	Excellent

^aExtrapolation to lower temperatures for phases that are stable at high temperatures only

data points at high temperatures (\sim linear extrapolation, low weight) be used in the fitting procedure (or constraint $b \geq 0$).

At low temperatures, $c_p \propto T^3$ (Debye limit, without effects like magnetic, spin, electronic contributions, see Table 1 for that); $c_p(0) \equiv 0$ in any case. We find that the type of equation best suited for a particular dataset depends on the data and their accuracy and the temperature range. In practice, a case-by-case approach is best. One can start with the Maier and Kelley equation and add terms (all possible permutations) until (with the smallest number of terms) the fit does not improve any more (but does not start to oscillate, either), for example measured by a minimum in the Akaike information criterion [172] AIC for n data points, data uncertainties σ_i and k parameters:

$$AIC = n(\ln(2\pi \chi^2/n) + 1) + 2k + 2k(k+1)/(n-k-1)$$

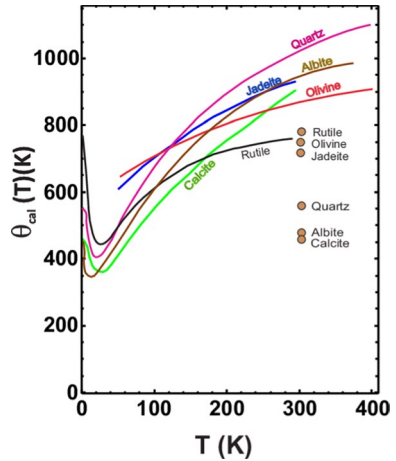
$$\chi^2 = \sum_i \frac{c_{p,fitted,i} - c_{p,observed,i}}{\sigma_i}$$

2.2.3.1 Debye Function Approximation The Debye integral can be evaluated by numerical quadrature. It is not generally known that it is tractable analytically in terms of a finite sum of polylogarithms [173–175], see Online Appendix A.1. We found, however, that the evaluation of polylogarithms is computationally even more inefficient than quadrature. There are also rational approximants [176] and an analytic expression by [177], the first one being only accurate for $T/\theta_D > 0.1$ and the latter deviating up to 6.5 % at $T/\theta_D < 0.2$. Padé approximations provide a convenient and very fast alternative [178, 179]. The Padé approximant that fits both the high- and low- T power law asymptotes of $C_v(T/\theta_D)$ and has additional terms in powers of $1/T$ in the numerator and denominator to fit the intermediate T range is

$$C_v/R = \frac{\sum_m N_m/x^n}{\sum_m D_m/x^m}, \quad x = \frac{T}{\theta_D}, \quad m = n + 3$$

The approximant by Goetsch, Anand et al. [179] does not deviate from the normalized Debye function by more than 2×10^{-4} at any T . By construction, the deviation goes to zero at both low and high T . The relative error has its maximum magnitude of 0.3 % at low T . We have constructed an even more accurate Padé

Fig. 7 Values of $\theta_D(T)$ for representative minerals. room temperature elastic values θ_D are shown by circles at 300 K; they are assumed to apply, approximately, at low temperatures, $T \rightarrow 0$, as well. After [61]



approximant ($n=8, m=11$; 17 independent coefficients; maximum relative deviation to true Debye= 5.755×10^{-6} at $T/\theta_D \sim 0.1$); full information is given in the Online Appendix.

2.2.3.2 ‘Calorimetric’ Debye Temperatures and Their Fit The calorimetric Debye temperature θ_D by definition leads to the same C_p (actually C_V) that was measured calorimetrically. Note that one can also define, after Grimvall [180] an ‘entropy’ Debye temperature, which leads to the measured $S(T)$; it is different from the calorimetric (heat capacity) Debye temperature we will discuss here.

Since we fit a function C_{exp} that depends on $3nZ$ vibrational degrees of freedom to a model having a single free parameter θ_D , it is obvious that we must pay a price, i.e., θ_D will vary with the particular temperature at which the fit is done. Typical $\theta_D(T)$ curves for minerals are shown in Fig. 5.

What is observed, for calorimetric Debye temperatures (from C_V !) is typically (e.g., [57], see Fig. 7).

- (i) Rapid fall from their $T \rightarrow 0$ limiting $\theta_D(0)$ plateau starting at a few K, to a minimum, $\theta_{D,min}$ at a temperature of the order of $\theta_D(0)/24$
- (ii) Subsequent rise to $\theta_D(\infty) = const.$, if anharmonic effects are negligible or have been removed.

Empirically, we found that $\theta_{cal}(T)$ can often be fitted very well with

$$\theta_{cal}(T) = a_1 \exp(-b_1 T) + a_2 [1 - \exp(-b_2 T^n)] + c \tag{12}$$

(Example Anorthite: $a_1=440.2$ K, $a_2=647$ K, $b_1=0.1384$ K⁻¹, $b_2=0.002616$ K⁻ⁿ, $c=330.7$ K, $n=1.19$).

Often, the calorimetric Debye temperature shows a plateau for $T < 5$ K to 10 K, with a limiting value of $\theta_{D,0\text{ K}}$ which can be estimated from the Debye temperature calculated from elastic constants (mean sound speed) and molar volume measured at room temperature⁶ [, see Eq. (1.2)].¹⁸¹

Our extended analytical model can capture this (paper II); however, this is usually only relevant for $T < 10$ K.

2.2.3.3 Determination of Lattice Heat Capacity In order to isolate a heat capacity anomaly, e.g., a transition peak, it is necessary to estimate the pure vibrational ('lattice') heat capacity in the complete temperature range where the anomaly has a significant effect. Various methods, more or less empirical, exist:

- The procedure described by Robie et al. [182, 183].
- The Komada–Westrum model [66, 67] fit to temperature regions not affected by the anomaly, extrapolation assuming a constant KW temperature.
- The principle of corresponding states [184, 185] with respect to an isostructural⁷ mineral. That is, the ratio of the low-temperature c_p to the c_p of the pure isostructural mineral can be used for a smooth extrapolation to zero Kelvin, see, e.g., in Krupka [92].
- We mostly use Eqs. 11 and 12, much easier to use than the KW model and more physical than the empirical methods in Robie or Krupka.

2.2.3.4 Practical Fitting of C_p and H Data, A Brief Review Gurevich et al. [186] describe the practical fitting of C_p and H data with a combination of Debye, Einstein, and Kieffer functions plus an additive $b_0TC_V^2$ term for expansion and anharmonicity. Something similar is also advocated by Boerio-Goates et al. [187] and Yong et al. [188], who propose the 'DES function'

$$C_p = nD(\theta_D/T) + mE(\theta_E/T) + n_S S(\theta_S/T),$$

where D is the (3D) Debye function, E the Einstein function, and a dramatic improvement of the fit could be achieved by including a two-level Schottky function S

$$S = \frac{(\theta_S/T)^2 \exp(-\theta_S/T)}{[1 + \exp(-\theta_S/T)]^2} \quad (\text{in units of } R)$$

⁶ Since v_p and v_s , decrease with increasing T , θ_D also decreases with increasing T . For typical minerals, θ_D (acoustic, 0 K) is about 22 K higher than at 300 K ($-0.07 \text{ K}\cdot\text{K}^{-1}$ at 300 K [181], Fig. 1, p. 81).

⁷ Two crystals are called isostructural, if they have the same structure, but not necessarily the same cell dimensions nor the same chemical composition, and with a 'comparable' variability in the atomic coordinates to that of the cell dimensions and chemical composition. For instance, calcite CaCO_3 , sodium nitrate NaNO_3 , and iron borate FeBO_3 are isostructural. One also speaks of isostructural series, or of isostructural polymorphs or isostructural phase transitions.

with the degeneracies of both levels set to one. No physical significance is attributed to the Schottky function. $n + m$ should approximate the number Z of atoms per unit cell, and for many silicates the Debye temperature is of the order of 400 K, the Einstein temperature of the order of 500 K to 1300 K, and the Schottky temperature θ_S is about 90 K. Maybe it is useful to add an expansion ($C_p - C_v$) multiplicative term like $(1 + A * T + B * T^2)$ which must be positive. Most experimental data can only be fit well if the temperature range is broken into at least a low- T and a high- T range, with individual fits joined at the best overlap point, typically around 150 K.

2.2.3.5 Adopted Procedure to Represent Experimental Data We can determine, by weighted non-linear least squares, the parameters of $\theta_{cal}(T)$, Eq. 12 which allows to calculate C_v , and with the Ernst–Lindemann relation (parameter A), C_p to which the experimental data are fitted.

We find that our model of $\theta_{cal}(T)$, evaluating the Debye function with a fast high-precision Padé approximant and with $C_p(C_v)$ calculated by (11) can very well fit experimental (lattice) heat capacities from 0 K to melting (decomposition) temperature to usually $\ll 1\%$ systematic accuracy. Of course, any ΔC_p from anomalies, lambda peaks, etc., have to be smoothed/fitted/represented on a case-by-case basis, and this is the reason why we store the final $c_p(T)$ curves, at least for low temperatures, in our database in tabular form, not as coefficients of some correlation equation; for datasets with anomalies, we often smooth the merged, weighted experimental data with orthogonal polynomials (in $\log c_p$ vs. $\log T$). Since there is no good fit function or theoretical description for the $c_p(T)$ for all minerals over all temperatures, it is best to represent smoothed $c_p(T)$ data in (electronic) tables and to use 1D interpolation on these tables. We will show that a suitable (and very fast) interpolation of the tabular data is able to reproduce any original fitted or smoothed (merged) dataset to very high accuracy in the complete temperature range. Usually, we join the low-temperature tabulated data with high-temperature polynomial correlations at some temperature close to 300 K where there is no jump in c_p and at most a very small change of slope dc_p/dT .

2.2.3.6 Representation of c_p in Tables, Temperature, and Pressure Sensitivity We have performed numerous numerical experiments on the best temperature spacing and interpolation method (see paper II)—suffice to say here that c_p is not very sensitive to temperature except of course near transition peaks, such that the effects of different temperature scales (e.g., ITS-90 vs. IPTS-68/48) are negligible and that the pressure dependence is negligible—so we can use C_p measured at 1 bar for the surfaces of atmosphere-less bodies as well as for a rocky subsurface down to many km on a terrestrial planet.

2.3 Practicalities: Atomic Masses, Mineralogical Composition, Conversion of Mass, Volume, Mole Fractions

Note that *atomic masses* are not constant in natural samples and have vastly different uncertainties [189, 190]. Since experimental C_p determinations actually measure

sample mass, thus, c_p , it is best to use the assumed molecular weight used in the original paper to convert back molar heat capacities C_p to specific heats c_p . Otherwise, we use the IUPAC (2013) atomic masses of elements common in minerals [189], where IUPAC gives ranges, the most likely value for rocks and minerals has been used.

2.3.1 Mineral Composition

The formulae of mineral can either be written as simplified formulas, e.g., (Ca,Mg,Fe)(Mg,Fe)Si₂O₆ indicating the possible substitutions (and vacancies □), the number of atoms in the substitution brackets not being specified, or as empirical formula. The latter can have fractional subscripts, but cations and anions must be charge-balanced; this is common for solid solutions. Example: Ca_{0.25}Mg₂FeAl_{0.5}Si_{3.5}O₁₀(OH)₂ (a saponite). We prefer, wherever possible, ideal formulas of the endmembers, even though these ideal compositions rarely exist in nature. For complex minerals, Hawthorne [191] discusses the correct and recommended endmember formula syntax.

The empirical chemical formula can be calculated from the elemental (or oxide) composition (mass fractions), which is rather straightforward for one mineral. For mixtures of minerals, *normative analysis* estimates the *idealized mineralogy* of a rock based on a quantitative chemical analysis according to the principles of geochemistry (i.e., likely reactions during formation). Normative mineral calculations can be done via the CIPW Norm [192] or other schemes [193]. Note that normative mineralogy is merely a calculation scheme based on predefined chemical entities (not all of which have mineralogical analogs) and thus provides an estimate of the hypothetical mineralogy of an igneous rock (a rock that crystallized from a melt). Its merit lies in the geochemical comparison of various igneous rocks suites, but it usually differs from the visually observable mineralogy (*modal analysis*).

Quantitative *modal analysis*, which we prefer, is used to determine the volumetric proportions of the minerals that make up the sample; it is estimated by identification and fractional area count of distinct minerals in thin sections, and gives volume fractions of these minerals in the sample. Densities of minerals ρ_i need to be known to convert volume fractions φ_i into mass fractions w_i .

To relate atomic percent x and weight percent w , aka mole (atomic) fraction and mass fraction:

$$\text{Mean molecular mass of mixture : } M = \sum x_j M_j = \left(\sum w_j / M_j \right)^{-1} \quad (13)$$

$$\text{Mole fraction (at.\%) : } x_j = (w_j / M_j) / \sum w_j / M_j = w_j \frac{M}{M_j} \quad (14)$$

$$\text{Mass fraction (wt\%) : } w_j = x_j M_j / M \quad (15)$$

Relationship between volume fraction φ (vol-%) and mass fraction w (mass%):

$$w_i = \frac{\rho_i}{\rho^0} \varphi_i \quad \text{with } \rho^0 = \sum \varphi_i \rho_i. \quad (16)$$

Note that there is an occasional confusion and inaccurate use of various concentration units, in particular where volume and mass quantities are mixed. Volume quantities depend on temperature (negligible for solid minerals, though) and on whether ideal or non-ideal mixtures are assumed (i.e., whether the volume of the solution after mixing is used as the reference or the sum of volumes of constituents prior to mixing).

We will use $[p, T = \text{const}]$:

$$\text{Volume fraction : } \varphi_j = \frac{V_j}{V_0}, \quad V_0 = \sum V_j, \quad \sum \varphi_j = 1$$

Volume concentration : $\sigma_j = \frac{V_j}{V}$, where V is the volume of the mixture, V_j is the volume of solute *prior* to mixing, and ρ is the density of the mixture.

Then (n : total number of mol)

$V^E = V - V_0$ excess volume (usually given as molar excess volume V^E/n , can be up to about $\pm 1 \text{ cm}^3 \cdot \text{mol}^{-1}$), $V_m = M/\rho$ ($\text{m}^3 \cdot \text{mol}^{-1}$). $\sigma_j \neq \varphi_j$ in general (equality only for ideal solutions).

$$\begin{aligned} \sigma_j &= w_j \frac{\rho}{\rho_j}, & w_j &= \sigma_j \frac{\rho_j}{\rho} \\ \varphi_j &= \frac{w_j / \rho_j}{\sum w_j / \rho_j}, & w_j &= \varphi_j \frac{\rho_j}{\sum w_j / \rho_j} = \varphi_j \frac{\rho_j}{\sum \varphi_j \cdot \rho_j} \end{aligned} \quad (17)$$

Mass concentration γ is defined as the mass of a constituent m_j divided by the volume of the mixture V :

$$\gamma_j = \frac{m_j}{V}, \quad w_j = \frac{\rho_j}{\rho}$$

For the automation of stoichiometric calculations (e.g., for thermal alteration decomposition reactions or composition from oxide content), see Anderson and Bjedov [194]; we use the convenient MATLAB[®] tool, *stoichtool* [195].

2.4 Experimental Methods and Their Accuracies

Background: mineralogists are interested in low-temperature C_p data, because these are needed to calculate the zero-point (i.e., third-law) entropy S^0 : $S^0 - S^{T=0K} = S^0 = \int_0^{298.15K} \frac{C_p}{T} dT$.

In terms of silicate minerals, it has been standard practice prior to about 2005, to measure their low temperature $C_p(T)$ behavior (often only once) using adiabatic calorimetry. Nowadays, a number of different devices is available that allow C_p coverage from ~ 0 K to roughly 2,000 K.

It is usually sufficiently accurate, for S^0 , to measure C_p down to about 5 K to 20 K and extrapolate C_p/T vs. T^2 (approximately straight line for most minerals and metals) to perform the C_p integration for the range 0 K to lowest measured temperature. Lower temperatures than 5 or 10 K are sometimes needed, if there are magnetic transitions in this range. The bulk of mineral c_p data is available down to 10 K or (with lesser accuracy) 5 K since ca. 1955, but often only to ~ 15 K. Before ca. 1950, the limit was typically 50 K. Accurate data for minerals appear since about 1935. Many mineral c_p data have been measured or re-measured since 1985. A good survey, reference, and recommendations for the various calorimetric techniques for solids can be found in [38, 196, 197]. There are various calorimetric standard substances to calibrate calorimeters, such as corundum (Al_2O_3 , *aka* alumina, synthetic sapphire, SRM720), benzoic acid, and copper; we have re-analyzed and re-fitted all available data on these standard substances (paper II). Their relative c_p accuracy can be as low as 0.05 % (corundum at medium temperatures [198]). In the following, we briefly present the main methods for accurate c_p measurements, in particular to give the reader a feeling on the typical experimental uncertainties. See also [16, 114] for a more detailed overview.

2.4.1 Low-Temperature Adiabatic Calorimetry ('Low-TAC') for up to ~ 340 K \pm 40 K

Low-temperature adiabatic calorimetry, which is typically carried out between about 5 and 400 K, is capable of delivering an experimental precision of about 0.1 % in the heat capacity. It requires rather large samples (order of 10 g to 30 g) and is complicated and time-consuming [199]. This method has been used extensively to measure the heat capacity of silicates and oxides and the compilation of Robie and Hemingway [43] summarizes results obtained over many years of study. Adiabatic calorimeters are not available commercially and there are only a few laboratories worldwide that are capable of making such measurements. Many of the data found in [43] derive from investigations made at the U.S. Bureau of Mines (U.S.B.M.) from 1940 to about 1970. Real accuracies, including systematic errors and non-reproducibility of samples, tend to be rather 5 % at 10 K, 2% at 15 K, 1 % at 20 K, and $\sim 0.2\%$ above 40 K [200].

2.4.2 Heat-Pulse Relaxation Calorimetry (PPMS) for 2 K to 400 K

New techniques and devices for small sample calorimetry (in the mg range) were developed in the 1970s. Based on this and later work [201] Quantum Design[®] [202] constructed a commercial relaxation calorimeter (available since ca. 1998 to 2003), implemented as the heat capacity option of the Physical Properties Measurement System (PPMS) [202]. Technical details of the instrument, as well its measuring procedures and performance, have been described in detail [203, 204]. PPMS measurements can be automated to a large extent; the accuracy is comparable to that of DSC. Older PPMS measurements (before 2005) often have higher uncertainties at the low temperatures (e.g., 1 % above 10 K, 5 % at 10 K) and failed at 1st-order phase transitions (due to automatic evaluation of the raw data with 2 relaxation constants). Kennedy et al. [205] showed that the accuracy of heat capacity determinations using the

QD PPMS can be within 1 % for $5 \text{ K} < T < 300 \text{ K}$ and 5 % for $0.7 \text{ K} < T < 5 \text{ K}$ under ideal conditions. Otherwise, significantly higher uncertainties were quoted [205]. Dachs and Benisek [206] found that the accuracy of C_p data obtained from powder measurements using the PPMS is generally lower compared to single crystal measurements. It is 1 % to 2 % for not too low temperatures and critically depends on sample geometry and sample mass, similarly to what Kennedy et al. [205] found. At best, the accuracy that could be obtained for powders calibrated to DSC at RT: 10 % @ 20 K, 3 % @ 40 K, 1 % for $> 60 \text{ K}$.

However, the methods continues to improve [16], e.g., improvements in accuracy on loose powders can be achieved by undertaking measurements on powder samples wrapped and pressed into thin and light Al-foil holders weighing $\sim 5.5 \text{ mg}$ (see also [207]) such that nowadays the accuracy of low-TAC can be similar, PPMS even better for $T < 15 \text{ K}$ [16].

Since ca. 2000, more and more data appear down to 1.9 K (lowest temperature for PPMS; recently 0.4 K with ^3He cooling). The required sample amount is typically 1 to 100 mg. Very careful handling is required for good accuracy $< 60 \text{ K}$ [208]. For further details of PPMS techniques, see [68, 203, 205].

2.4.3 Differential Scanning Calorimetry (DSC)

There are two basic types of DSC methods: heat flux and power compensation DSC. In heat flux DSC calorimeters, the sample and the reference are heated in the same furnace while measuring the temperature difference between sample and reference. The temperature difference is converted to a difference in power using a calibration. Such calorimeters can be operated between ca. 100 and 1800 K. In spite of this large temperature range, these calorimeters are not often used for measuring the heat capacity, because of their only moderate accuracy. In power compensation DSC, sample and reference are heated separately by micro furnaces. These are maintained at the same temperature during heating while measuring the difference in heating power (heat flow). A power compensation DSC [209–212] can be operated between ca. 100 K and 1000 K with better accuracy ($\sim 1 \%$ to 2%), enabling rather precise heat capacity measurements; commercial DSCs are widely used in industry and science and are often very conveniently automated. DSC techniques for very high (e.g., up to 1500 K [60, 213]) and low (down to ca. 1 K [60]) have been developed, but most measurements with commercial instruments are conducted within the range 100 K to 700 K.

A principal disadvantage of DSC is [38] that because it is so easy to use it is also very easy to abuse: It has been said [196] that the very ease of obtaining data by DSC can lead to work which is of questionable accuracy if the operator fails to observe many necessary and rigorous principles. For accurate measurements, the 3-curve method with (not necessarily overlapping) temperature scans (step-scanning) and baseline postprocessing is recommended, see [214–216].

Note that DSC measurements are inherently dynamic, as the sample temperature is a (linear) function of time; thermodynamic equilibrium is never attained, meaning that in practice (due to finite thermal conductivities) the sample is never at a uniform temperature [183, 212, 217–219]. With typical instruments, heating rates

of $\sim 10 \text{ K}\cdot\text{min}^{-1}$ are used; with a sample mass of $\sim 30 \text{ mg}$ in powdered form, typical thermal inhomogeneities in the sample are of the order of $\sim 1 \text{ K}$, thus broadening features (like an actually sharp peak) accordingly.

2.4.4 Drop Calorimetry

Drop calorimetry (e.g., [155]) is used to measure the heat capacity at temperatures higher than ca. 900 K. In this calorimetric technique, a sample (equilibrated to e.g., room temperature, T_1) is dropped into the calorimeter, whose high temperature (T_2) is controlled by a surrounding furnace. The small temporary temperature decrease generated by dropping the sample into the calorimeter is recorded as a function of time. Integrating these data and applying a calibration yields the absolute heat content (enthalpy H change) of the sample when heated from T_1 to T_2 . Heat capacity is then calculated from differentiating the $H(T)$ curve; the difficulty here is to estimate reasonable uncertainties of C_p .

A simple and elegant but not very accurate variation of drop calorimetry for the non-destructive measurement of the c_p (at $\sim 180 \text{ K}$) of meteorites has been devised by Consolmagno et al. [23] using liquid nitrogen vaporization; basically, the enthalpy difference between 77 K and 'room temperature' is determined, with random and systematic uncertainties of $\sim 2\%$ and $\sim 4\%$, respectively.

2.4.5 Important Notes for Experimental c_p Data

Homogeneity PPMS and DSC require only $\sim 3 \text{ mg}$ to 30 mg of sample. Consequently, high purity and homogeneity of the sample are required for the measurement to be representative of the whole sample.

Curvature correction The true heat capacity at temperature T is given by $C_p = \lim_{\Delta T \rightarrow 0} \Delta H / \Delta T = dH/dT$.

The result of classical, stepwise measurements is the mean heat capacity, $C_{p,mean} = \Delta H / (T_2 - T_1)$, associated with the mean temperature of the interval, $T_m = (T_1 + T_2) / 2$. Deviation from linearity in the C_p versus T curve will therefore require adjustment of the mean heat capacity by a curvature correction [200] to yield the true heat capacity at T_m , or, equivalently, a correction to T_m . The curvature correction can often be neglected if ΔT is only a few K and if there is no transition peak.

Sample preparation, humidity control Handling of the sample in humid laboratory air can change the (sorption or crystal water) content of a sample. Dehydrated phyllosilicates can adsorb of the order of 10 % terrestrial water rapidly, which changes specific heat significantly. Drying the sample to a defined state is mandatory, and frost depositing on cold sample or calorimeter surfaces must be avoided.

Premelting Most substances studied today by accurate calorimetric methods are pure enough to render the effect of impurities on the observed heat capacity data negligible except in the region just below the melting point. In some minerals, an abnormal increase in enthalpy and C_p well below the melting point has been

observed [170], which can be caused by structural changes, by Frenkel thermal vacancies [220] or by classical impurity premelting.

The effect of temperature uncertainty (including the temperature scale used, ITPS-27, ITPS-48, ITPS-68, ITS-90, and various low-temperature extensions for example) is significant only at low temperatures (or in the vicinity of first-order or sharp lambda peak). The absolute T uncertainty leads to typical C_p uncertainties of the order of 1 % to 2 % at 1 K, 0.3 % at 10 K, and ~ 0.01 % at $T > 100$ K. Note that for commercial DSC at high temperatures, the temperature uncertainty including non-isothermality of the sample can be up to 1 K [215]—the relative error introduced by this is < 1 % for $T > 100$ K and $< 0.2\%$ for $T > 300$ K. This leads us to.

Temperature resolution of $C_p(T)$ curves a temperature range in the sample volume is inherent for the dynamic (PPMS and DSC) techniques. Conversely, $C_p(T)$ is averaged, in the sample volume, over a finite temperature range ΔT in low-TAC or drop calorimetry; ΔT can be chosen by the experimenter, but of course there is a trade-off with noise/accuracy. This means that sharp $C_p(T)$ peaks invariably get distorted (lower peak heights and broader peaks, shift of peak temperature), cf. [212, 217–219].

Differences between natural and synthetic crystals It is possible that slight differences in $C_p(T)$ behavior could exist between some natural and synthetic crystals. The latter could be more structurally ‘disordered’ than their natural analogs due to the shorter times and often higher temperatures associated with their crystallization. Grossular $\text{Ca}_3\text{Al}_2\text{Si}_3\text{O}_{12}$ has been well studied [16]; the relative C_p difference at low T (< 100 or 200 K) for various natural grossular versus synthetic grossular reaches is small but measurable, reaching ~ 10 % at 40 K and ~ 20 % at 20 K. Internal stresses and strains in natural materials are also known to influence transition features. Not to be confused with the effect of compositional zoning in a sample volume. For olivines, the $C_p(T)$ behavior of the natural, well-crystallized forsterite $\text{Fo}_{0.894}\text{Fa}_{0.106}$ and a crystalline synthetic $\text{Fo}_{90}\text{Fa}_{10}$ sample are in excellent agreement between about 7 and 300 K [221]. It would appear that any phonon difference arising from possible variations in Fe^{2+} -Mg order–disorder are minimal to nil despite their contrasting crystallization histories and small differences in chemistry.

3 Minerals in the Solar System

Here, we briefly have a look which mineral could be important in the solar system, apart from those known to be common (at a mass fraction > 1 % or so) in meteorites. For the latter, see e.g., the excellent review on meteoritic minerals by Rubin and Ma [222]; about 435 mineral species have been identified in meteorites, of which only a few are significant for c_p (Table 4).

Table 4 Probable rocks and minerals on the surface of Mercury, Venus, and Mars, compilation from various references

Body	Rocks and minerals																																												
Mercury	<p><i>Fe, Ti-rich anorthosites</i> [230];</p> <p>Plagioclase, forsterite, enstatite, some graphite and sulfides. Poor in Fe²⁺ [234]</p> <p>Fe, Ti-rich <i>anorthosites</i>. 38–58 wt% albite, up to 37 wt% enstatite, up to 22 wt% diopside, up to 33 wt% forsterite, and up to 8 wt% quartz along with some graphite and minor sulfide (plausibly oldhamite, niningerite, keilite, troilite, and wassonite). Olivine and pyroxene on Mercury must be very magnesian. It is plausible that mercurian <i>rocks</i> contain high-pressure phases formed from common minerals: e.g., ringwoodite from olivine, majorite from low-Ca pyroxene, coesite, stishovite (and perhaps other high-density polymorphs) from silica, and lingunite (NaAlSi₃O₈) from plagioclase [235]</p>																																												
Venus	<p><i>K-rich basalts, olivine gabbro-norite</i> (calcium-rich plagioclase labradorite, orthopyroxene, and olivine) [230];</p> <p>Probably mostly <i>felsic</i>; common felsic minerals include quartz, muscovite, orthoclase, and the sodium-rich plagioclase feldspars (albite-rich). Possibly dehydrated saponite, montmorillonite; ferric oxide; likely sulfides, sulfates (anhydrite!). ~ 11 % Fa in olivines, ~ 22 % Fs in pyroxene. + likely carbonates (less calcite because this converts mostly to anhydrite, but dolomite, magnesite). [236]</p> <p>Normative compositions based on Venera probes [237]:</p> <table border="1"> <thead> <tr> <th>Mineral</th> <th>Venera 13</th> <th>Venera 14</th> <th>Vega 2</th> </tr> </thead> <tbody> <tr> <td>Orthopyroxene</td> <td>–</td> <td>18.2</td> <td>25.4*</td> </tr> <tr> <td>Clinopyroxene</td> <td>–</td> <td>–</td> <td>2.5[†]</td> </tr> <tr> <td>Diopside</td> <td>10.2</td> <td>9.9</td> <td>–</td> </tr> <tr> <td>Olivine</td> <td>26.6</td> <td>9.1</td> <td>13.9[‡]</td> </tr> <tr> <td>Anorthite</td> <td>24.2</td> <td>38.6</td> <td>38.3</td> </tr> <tr> <td>Albite</td> <td>3.0</td> <td>20.7</td> <td>18.9</td> </tr> <tr> <td>Orthoclase</td> <td>25.0</td> <td>1.2</td> <td>0.5</td> </tr> <tr> <td>Nepheline</td> <td>8.0</td> <td>–</td> <td>–</td> </tr> <tr> <td>Ilmenite</td> <td>3.0</td> <td>2.3</td> <td>0.5</td> </tr> <tr> <td>Total</td> <td>100.0</td> <td></td> <td>100.0</td> </tr> </tbody> </table> <p>*75 mol% En [†]1.2 mol% Wo, 0.9 mol% En, 0.4 mol% Fs [‡]75 mol% Fo</p> <p>Plains units (~80 % of the surface): <i>basaltic lava flows, alkaline basalt</i> (Venera 13) and <i>tholeiitic basalt</i> (Venera 14 and Vega 2); we can infer that major minerals in the crust include calcium-rich plagioclase, orthopyroxene, Ca-pyroxene and olivine.</p> <p>Some regions of Venus (the tessera) are assumed to be more <i>felsic</i> (based on their relatively low ~1 μm emissivity values) and might contain silica minerals.</p> <p>The rest is guesswork: anhydrite (CaSO₄) is stable at the surface. Pyrite (FeS₂) may also occur; moderately ferroan olivine and low-Ca pyroxene are also stable. Weathering of phases containing ferrous iron could produce magnetite, hematite, and/or maghemite, hematite being probably the dominant (if not exclusive) iron oxide on Venus, consistent with the visible and near-infrared spectra obtained by the landers Venera 9, Venera 10. [235]</p>	Mineral	Venera 13	Venera 14	Vega 2	Orthopyroxene	–	18.2	25.4*	Clinopyroxene	–	–	2.5 [†]	Diopside	10.2	9.9	–	Olivine	26.6	9.1	13.9 [‡]	Anorthite	24.2	38.6	38.3	Albite	3.0	20.7	18.9	Orthoclase	25.0	1.2	0.5	Nepheline	8.0	–	–	Ilmenite	3.0	2.3	0.5	Total	100.0		100.0
Mineral	Venera 13	Venera 14	Vega 2																																										
Orthopyroxene	–	18.2	25.4*																																										
Clinopyroxene	–	–	2.5 [†]																																										
Diopside	10.2	9.9	–																																										
Olivine	26.6	9.1	13.9 [‡]																																										
Anorthite	24.2	38.6	38.3																																										
Albite	3.0	20.7	18.9																																										
Orthoclase	25.0	1.2	0.5																																										
Nepheline	8.0	–	–																																										
Ilmenite	3.0	2.3	0.5																																										
Total	100.0		100.0																																										
Mars	<p>H₂O ice, CO₂ ice (polar caps).</p> <p><i>Andesites and basalts</i> with plagioclase, pigeonite, augite, enstatite, olivine, magnetite</p> <p><i>Secondary rocks</i> with pyrrhotite, phyllosilicates (smectite), goethite, jarosite, gypsum, montmorillonite [230]</p>																																												

4 Background: Description of Minerals and Compounds

A mineral or mineral species is a naturally occurring, macroscopically homogeneous solid chemical compound with a fairly well-defined chemical composition and a

Table 4 (continued)

	<p>In situ (rovers): Mineralogy seems highly variable with location. The most abundant minerals in the <i>igneous rocks, andesites and basalts</i>, are plagioclase, olivine, pigeonite, augite, and magnetite. The <i>sedimentary rocks and soils</i> contain phyllosilicates (smectites like montmorillonite), gypsum, anhydrite, pyrrhotite, magnetite, goethite, hematite, jarosite, opal, Mg-rich carbonate (probably dolomite), siderite, epsomite, halides, tridymite [235].</p> <p>Martian meteorites: the most abundant variety of martian meteorite is the group of <i>shergottites</i> and related rocks. The most abundant phases are compositionally zoned pyroxene (augite, subcalcic augite, pigeonite and/or orthopyroxene), olivine (Fa24–40), and maskelynite and/or plagioclase (Ab30–50) [235].</p>
Moon	<p>Most lunar samples are mare material, i.e., <i>basaltic</i>, with a few samples from highland material, which is mostly <i>anorthositic</i> (end member mineral: anorthite $\text{CaAl}_2\text{Si}_2\text{O}_8$). Mare <i>basalts</i> are further distinguished as ‘Low-Ti’, 1.5 % to 9 % of TiO_2, and ‘high-Ti’, > 9 % TiO_2. The <i>mare basalts</i> are richer in TiO_2 than the <i>highland rocks</i> (0 % to 5 %). Ilmenite (FeTiO_3) is one of the minerals which have been detected widespread on the surface of the Moon. The abundances of ilmenite in high-Ti basaltic lava are higher (9 % to 19 %) than in high-Ti mare soil (< 10 %) [238].</p> <p>Lunar minerals in order of importance [238]</p> <ul style="list-style-type: none"> • Pyroxene (Ca,Fe,Mg)$_2\text{Si}_2\text{O}_6$ • Plagioclase feldspar (Ca,Na)(Al,Si)$_4\text{O}_8$, mostly anorthite (90 mol%), rest albite • Olivine (Mg,Fe)$_2\text{SiO}_4$; most mare basalt olivines have compositions in the range Fa20–Fa70 • Potassium feldspar (orthoclase/microcline) (KAlSi_3O_8) • Mineraloids are present, up to ~ 30 vol%, as various glasses, either ‘highland glasses’, mostly anorthositic plagioclase glass with some iron oxide or ‘mare (lowland) glasses’, mostly basaltic (pyroxene glass). • Ilmenite (Fe,Mg)TiO_3 • Spinel (various compositions, e.g. MgAl_2O_4) • Rare: silica minerals SiO_2, only cristobalite, quartz, tridymite), < 1 % usually; the most common silica mineral in mare basalt lavas is not quartz but cristobalite, which can constitute up to 5 vol% of some basalts. • There are no Fe^{3+} compounds, no hydrated minerals like clays, micas, amphiboles • Armalcolite (Fe,Mg)Ti_2O_5 only in Ti-rich basalts • Native iron (Fe, ~ 0.3 % by mass) and troilite (FeS) < 1 %

specific crystal structure. Traditionally amorphous substances which fulfill the other criteria are included but called mineraloids. Minerals can be elements, organic or inorganic compounds—some minerals in fact are among the most complex inorganic compounds known. Of the ~6000 mineral species recognized today, most are inorganic and are silicates. Many minerals form solid solution (substitution) series, ‘joins,’ and usually we seek the physical properties of the endmember minerals of a series. Note that, for e.g., ‘olivine’ is not a mineral, but a mineral group; but an olivine with a specified composition, like $\text{Fo}_{90}\text{Fa}_{10}$, is a mineral. Solid solutions can be considered in terms of three categories: complete solid solutions without structural ordering, solid solutions with structural ordering, and partial solid solutions. The recommended mineral nomenclature in each of these categories is discussed in [229].

A solid solution may be defined as a homogeneous phase composed of different chemical substances whose concentrations may be varied without the precipitation of a new phase. This variation can be classified in three types: substitutional (by far the most important, includes multicomponent and coupled substitutions), interstitial

(example: tridymite, SiO_2 , toward nepheline, $\text{NaAlSi}_3\text{O}_8$), and omissions (example: wüstite Fe_{1-x}O).

In this paper, we include condensed gases like methane and carbon dioxide because on some cold outer solar system bodies they are believed to form the bulk of the surface material. We also include the enigmatic tholins, ‘complex abiotic organic gunk’ [13] for the same reason.

Two common classifications, ‘Dana’ and ‘Strunz’ in short, are used for minerals; both rely on composition, specifically with regard to important chemical groups, and structure. Dana, as of 1997, is in its eighth edition [230]. The less commonly used (Nickel-)Strunz classification [231] is based on the Dana system, but combines both chemical and structural criteria, the latter with regard to distribution of chemical bonds.

The International Mineralogical Association (IMA) is the generally recognized standard body for the definition and nomenclature of mineral species. The *IMA Database of Mineral Properties* <https://rruff.info/ima/>, is representing the ‘official’ IMA list of minerals on the web. For detailed mineral descriptions and properties, it is linked to the following useful websites:

- Handbook of Mineralogy, pdf online version, <http://www.handbookofmineralogy.org/> [232]
- American Mineralogist Crystal Structure Database, <https://rruff.geo.arizona.edu/AMS/amcsd.php> [233]
- RRUFF™ database, <https://rruff.info/>, <https://rruff.geo.arizona.edu/doclib/hom> for pdf summaries [234]
- mindat.org page, the world’s largest open database of minerals, rocks, meteorites, and the localities they come from. Mindat.org is run by the not-for-profit Hudson Institute of Mineralogy [235]
- webmineral.com, © 1997–2014 by David Barthelmy [236]

Crystallographic, thermal expansion and elastic data for many minerals have been compiled in [181].

In this chapter, we describe the most common/important mineral groups that, to our current knowledge, occur in extra-terrestrial regoliths. What we present here, in an order only loosely resembling the IMA classification, is (with some exceptions) not new but rather a condensed and simplified textbook (e.g., [223]) knowledge. In fact we often employ the same sources as *Wikipedia, The Free Encyclopedia*, <https://en.wikipedia.org/> (which is a usually a high-quality source if it comes to minerals). We believe that this condensed background is useful for the non-mineralogist, since the terminology of mineral species can be quite complex (in particular for the so-called clay minerals, or phyllosilicates), and there are often conventional/historical names in addition to the official ones. Even the official mineral names can be quite exotic! For minerals with variable compositions caused by solid solutions we will identify and treat normally only the (idealized) endmembers. We will focus, besides definition and composition, on describing the properties relevant for specific heat (polymorphs, phase transitions, or and dehydration/decomposition/melting at elevated temperatures).

In literature describing the mineralogy of, e.g., meteorites, the reader will often encounter component's mineral names which are not in our database (and won't ever be). On the one hand, this has historical reasons, some minerals have had different names until the IMA came to an official recommendation; yet mostly, analytic methods do not well resolve composition within solid solution series, and there are numerous names for minerals of intermediate composition between (2, 3, or more) endmembers, some of them obsolete, some very common. We mention, for example, feldspars (plagioclase, anorthoclase, oligoclase, andesine, labradorite, bytownite), pyroxenes (augite, pigeonite, hypersthene, bronzite), olivine, hornblende, and many others.⁸

Phyllosilicates belong to the most complex inorganic compounds. It is therefore not surprising, that for example in modal analysis, the exact empirical formulas of the observed phyllosilicates very often cannot be given, and only a broad categorization into 'saponite' and 'serpentine' is done. What exactly these terms mean is not uniform in literature and depends also on context information, like iron content.

Table 5, an abridged version of a much more detailed 'master table,' gives an overview of our minerals and compounds database to date. The entries are alphabetically sorted alphabetically (1) after mineral group, (2) after subgroup (if any; not shown), (3) after name.

4.1 Feldspars (Framework (Tecto-)silicates)

Framework silicates comprise the feldspar group, the quartz family (treated separately in this paper), the feldspathoids like leucite, nepheline, sodalite, the scapolite group, and the zeolite family (not found yet in astro-materials).

Feldspars proper are the most common rock-forming minerals. 'It is an understatement to claim that feldspar structures are complicated' [223] and this is why we spend some effort to explain the feldspar polymorphs in this section.

There are three main feldspar endmembers (Fig. 8):

- Orthoclase, potassium feldspar (K-feldspar) endmember KAlSi_3O_8 , and polymorphs
- Albite, sodium feldspar (Na-feldspar), endmember $\text{NaAlSi}_3\text{O}_8$, and polymorphs
- Anorthite, calcium endmember $\text{CaAl}_2\text{Si}_2\text{O}_8$.

Only limited solid solution occurs between K-feldspar and anorthite, and in the two other solid solutions, immiscibility occurs at temperatures common in the crust of the Earth; solid solutions between K-feldspar and Na-feldspar are called 'alkali feldspars'

⁸ The old name '*hypersthene*' is an orthopyroxene with ~30 % En and rest Fs. *Bronzite* is also a member of the pyroxene group of minerals, belonging with enstatite and hypersthene to the orthorhombic series of the group. Rather than a distinct species, it is really a ferriferous variety of enstatite. $(\text{Mg,Fe})\text{SiO}_3$, the iron(II) oxide ranges from about 12 % to 30 %. *Hornblende* is an IMA-CNMNC defined amphibole root-name with strict chemical boundaries but is often confused with the more loosely defined 'hornblende,' which is a term used by petrologists and mineral collectors for any black undefined amphibole in the calcium (and sometimes in the sodium-calcium) subgroups [235]

Table 5 Abridged database—overview

No.	Abbr	Name	Group	Formula	ρ (g·cm ⁻³ , 25 °C)
1	Fact	Ferro-actinolite	Amphibole	C ₂₂ Fe ₃ Si ₈ O ₂₂ (OH) ₂	3.34
2	Tr	Tremolite	Amphibole	C ₂₂ Mg ₅ Si ₈ O ₂₂ (OH) ₂	2.98
3	Cum	(Magnesio-)Cumming-tonite	Amphibole	□Mg ₇ Si ₈ O ₂₂ (OH) ₂	2.97
4	Gru	Grunerite	Amphibole	□(Fe ²⁺) ₇ Si ₈ O ₂₂ (OH) ₂	3.53
5	Ath	Anthophyllite	Amphibole	□Mg ₇ Si ₈ O ₂₂ (OH) ₂	2.86
6	Fath	Ferro-anthophyllite	Amphibole	□(Fe ²⁺) ₇ Si ₈ O ₂₂ (OH) ₂	3.59
7	Cal	Calcite	Carbonates	CaCO ₃	2.71
8	Dol	Dolomite	Carbonates	CaMg(CO ₃) ₂	2.87
9	Mgs	Magnesite	Carbonates	MgCO ₃	3.01
11	Sd	Siderite	Carbonates	FeCO ₃	3.94
10	Na2CO3	Sodium carbonate, anh	Carbonates	Na ₂ CO ₃	2.54
12	Ab	Albite	Feldspars	NaAlSi ₃ O ₈	2.62
13	An	Anorthite	Feldspars	CaAl ₂ Si ₂ O ₈	2.76
14	Or	Orthoclase	Feldspars	KAlSi ₃ O ₈	2.56
15	Nph	Nepheline	feldspathoid	(Na ₃ K)Al ₄ Si ₄ O ₁₆	2.59
16	Alm	Almandine	Garnets	Fe ₃ Al ₂ (SiO ₄) ₃	4.32
17	Adr	Andradite	Garnets	C ₃ Fe ₂ Si ₃ O ₁₂	3.86
18	Grs	Grossular(ite)	Garnets	C ₃ Al ₂ (SiO ₄) ₃	3.59
19	Ptp	Pyrope	Garnets	Mg ₃ Al ₂ (SiO ₄) ₃	3.58
20	Sps	Spessartine	Garnets	Mn ²⁺ ₃ Al ₂ (SiO ₄) ₃	4.19
21	Uv	Uvarovite	Garnets	Ca ₃ Cr ₂ (SiO ₄) ₃	3.83
22	HI	Halite	Halides	NaCl	2.16
23	Syl	Sylvite	Halides	KCl	1.99
24	CO2	Carbon dioxide	Ices	CO ₂	1.10
25	CO	Carbon monoxide	Ices	CO	0.92
26	C2H6	Ethane	Ices	C ₂ H ₆	0.60

Table 5 (continued)

No.	Abbr	Name	Group	Formula	ρ (g·cm ⁻³ , 25 °C)
27	C2H5OH	Ethanol	Ices	C ₂ H ₅ OH	1.03
28	Ice	Ice Ih	Ices	H ₂ O	0.92
29	CH4	Methane	Ices	CH ₄	0.50
30	CH3OH	Methanol	Ices	CH ₃ OH	0.70
31	N2	Nitrogen	Ices	N ₂	0.95
32	Al	Aluminum	Metals	Al	2.70
33	Cu	Copper	Metals	Cu	8.92
34	Fe	Iron	Metals	Fe	7.88
35	Kamc	Kamacite	Metals	α FeNi	7.90
36	FeNi	Meteoritic iron	Metals	FeNi	8.00
37	Ni	Nickel	Metals	Ni	8.91
38	Tae	Taenite	Metals	γ FeNi	8.30
39	Tta	Tetraetaenite	Metals	L10-FeNi	8.30
42	Fa	Fayalite	Olivines	Fe ₂ SiO ₄	4.39
43	Fo	Forsterite	Olivines	Mg ₂ SiO ₄	3.21
44	Hem	Hematite	Ox-/hydroxides	Fe ₂ O ₃	5.28
45	Ilm	Ilmenite	Ox-/hydroxides	FeTiO ₃	4.79
46	Mgh	Maghemite, Fe(II)-deficient magnetite	Ox-/hydroxides	γ-Fe ₂ O ₃	4.86
47	Mag	Magnetite	Ox-/hydroxides	Fe ₃ O ₄ , Fe ²⁺ (Fe ³⁺) ₂ O ₄	5.20
48	Wüts	Wüstite	Ox-/hydroxides	FeO	5.99
49	Fhy	2-line ferrhydroite	Ox-/hydroxides	FeOOH·0.027H ₂ O	3.80
50	Aka	Akaganéite	Ox-/hydroxides	β FeOOH·0.652H ₂ O	3.52
51	Cor	Corundum	Ox-/hydroxides	Al ₂ O ₃	3.99
52	Bse	Bunsenite	Ox-/hydroxides	NiO	6.67

Table 5 (continued)

No.	Abbr	Name	Group	Formula	ρ (g·cm ⁻³ , 25 °C)
53	Lm	Lime, calcium oxide anh	Ox-/hydroxides	CaO	3.34
54	Per	Periclase	Ox-/hydroxides	MgO	3.58
55	Rt	Rutile	Ox-/hydroxides	TiO ₂	4.24
56	Fap	Fluorapatite	Phosphates	Ca ₁₀ (PO ₄) ₆ F ₂	3.20
57	Hap	Hydroxyapatite	Phosphates	Ca ₁₀ (PO ₄) ₆ (OH) ₂	3.16
58	Chm	Chamosite	Phyllosilicates	(Fe ²⁺ , Mg) ₂ Al ₂ (AlSi ₃ O ₁₀)(OH) ₈	3.13
59	Clc_L	Clinchlore (Mg-Chl)	Phyllosilicates	(Mg _{0.097} Fe ²⁺ _{0.903}) ₅ Al(Si ₃ Al)O ₁₀ (OH) ₈	2.72
60	Clc_M	Clinchlore (Fe-Chl M)	Phyllosilicates	(Mg _{0.594} Fe ²⁺ _{0.406}) ₅ Al(Si ₃ Al)O ₁₀ (OH) ₈	3.32
61	Clc_W	Clinchlore (Fe-Chl W)	Phyllosilicates	(Mg _{0.589} Fe ²⁺ _{0.411}) ₅ Al(Si ₃ Al)O ₁₀ (OH) ₈	3.05
62	Kln	Kaolinite	Phyllosilicates	Al ₂ Si ₂ O ₅ (OH) ₄	2.62
63	Pri	Pyrophyllite	Phyllosilicates	Al ₂ Si ₄ O ₁₀ (OH) ₂	2.78
64	Tlc	Talc	Phyllosilicates	Mg ₃ Si ₄ O ₁₀ (OH) ₂	2.78
65	Ilt	Illite (group)	Phyllosilicates	K _{0.65} Al ₂ 0 ₆₅ Al _{0.65} Si _{3.35} O ₁₀ (OH) ₂ n(H ₂ O)	2.80
66	Ms	Muscovite 2M1	Phyllosilicates	KAl ₂ (AlSi ₃ O ₁₀)(OH) ₂	2.83
67	Ann	Annite	Phyllosilicates	KFe ₃ ²⁺ AlSi ₃ O ₁₀ (OH) ₂	3.36
68	Eas	Eastonite	Phyllosilicates	KAlMg ₂ (Si ₂ Al ₂)O ₁₀ (OH) ₂	2.59
69	Phl	Phlogopite	Phyllosilicates	KMg ₃ AlSi ₃ O ₁₀ (OH) ₂	2.79
70	Sid	Siderophyllite	Phyllosilicates	KFe ²⁺ Al ₂ (Al ₂ Si ₂ O ₁₀)(OH) ₂	3.18
71	Atg	Antigorite/Lizardite, Chrysotile	Phyllosilicates	Mg ₃ Si ₂ O ₅ (OH) ₄	2.59
72	Plg	Attapulgite = Palygorskite	Phyllosilicates	Mg _{1.5} Al _{0.5} Si ₄ O ₁₀ (OH) ₄ (H ₂ O)	2.40
73	Brh	Berthierite	Phyllosilicates	(Fe _{2.5} Al _{0.5})Si _{1.5} Al _{0.5} O ₅ (OH) ₄	3.00
74	Vrm	Vermiculite	Phyllosilicates	Mg _{0.7} (Mg,Fe,Al) ₆ (Si ₁₄) ₈ O ₂₀ (OH) ₄ ·8H ₂ O	2.26
75	Bei	Beidellite	Phyllosilicates	Na _{0.5} Al _{2.5} Si _{3.5} O ₁₀ (OH) ₂ ·(H ₂ O)	2.00

Table 5 (continued)

No.	Abbr	Name	Group	Formula	ρ (g·cm ⁻³ , 25 °C)
76	Mnt	Montmorillonite	Phyllosilicates	(Na,Ca) _{0.33} (Al,Mg) ₂ (Si ₄ O ₁₀)(OH) ₂ ·n(H ₂ O)	1.85
77	Non	Nontronite	Phyllosilicates	Na _{0.3} Fe ₂ (Si,Al) ₄ O ₁₀ (OH) ₂ ·n(H ₂ O)	2.25
78	Sap	Saponite	Phyllosilicates	Ca _{0.25} (Mg,Fe) ₃ (Si,Al) ₄ O ₁₀ (OH) ₂ ·n(H ₂ O)	2.27
79	Ks	Kuishirote (Ca-Tschermak)	Pyroxenes	CaAlAlSiO ₆	3.43
80	Aeg	Aegirine (Acmite)	Pyroxenes	(NaFe ³⁺)Si ₂ O ₆	3.58
81	Wo	Wollastonite	Pyroxenes	Ca ₂ Si ₂ O ₆	2.91
82	Di	Diopside	Pyroxenes	CaMgSi ₂ O ₆	3.28
83	En	Enstatite	Pyroxenes	Mg ₂ Si ₂ O ₆	3.19
84	Fs	Ferrosilite	Pyroxenes	Fe ₂ Si ₂ O ₆	4.00
85	Hd	Hedenbergite	Pyroxenes	CaFeSi ₂ O ₆	3.65
86	Lch	Lechatelierite	Silicates	SiO ₂ , amorphous	2.20
87	Qz	Quartz	Silicates	SiO ₂	2.65
89	Nam	Sodium Metasilicate	Silicates	Na ₂ SiO ₃	2.61
91	Spl	(Magnesio-)Spinel	Spinel	MgAl ₂ O ₄	3.58
92	Chr	Chromite	Spinel	FeCr ₂ O ₄	5.10
93	Hc	Hercynite	Spinel	FeAl ₂ O ₄	4.34
94	Anh	Anhydrite	Sulfates	CaSO ₄	2.96
95	Esm	Epsomite	Sulfates	MgSO ₄ ·6.868H ₂ O	1.68
96	Gp	Gypsum	Sulfates	CaSO ₄ ·2H ₂ O	2.31
97	FeSO4	Iron(II)sulfate, anh	Sulfates	FeSO ₄	3.65
98	MgSO4	Magnesium sulfate anh	Sulfates	MgSO ₄	2.66
99	Ph	Pentlandite	Sulfides	(Fe,Ni) ₉ S ₈	4.80
100	Py	Pyrite	Sulfides	FeS ₂	5.01
101	Po	Pyrrhotite	Sulfides	Fe _{0.9} S; Fe _{1-x} S, x = 0 - 0.2	4.63

Table 5 (continued)

No.	Abbr	Name	Group	Formula	ρ (g·cm ⁻³ , 25 °C)
102	Tro	Troilite	Sulfides	FeS	4.83
40	Dia	Diamond	C-rich matter	C (cubic)	3.53
41	Gr	Graphite	C-rich matter	C (hexagonal)	2.23
103	ICOM	Complex organic matter	C-rich matter	C,H,O,N, ...	0.90
104	Coal	sub-bituminous coal	C-rich matter	C,H,O,N, ...	1.35
105	ANG	Apiezon® N grease	Other	C ₁₁₁ H ₂₀₈	0.91
106	Bza	Benzoic acid	Other	C ₇ H ₆ O ₂	1.27
107	PE	Polyethylene	Other	(C ₂ H ₄) _n , polymeric	0.92
108	Adh	Ammonia dihydrate	Other	NH ₃ ·2H ₂ O	0.99
109	Cem	Cementite, iron carbide	Other	Fe ₃ C	7.69
110	Coh	Cohenite, FeNi carbide	Other	(Fe,Ni) ₃ C ₃	7.65
111	Wlh	Hydrate water/ice-like	Other	H ₂ O	0.92
112	WZeo	Hydrate water/zeolitic	Other	H ₂ O	0.92

Here, we list all minerals and substances currently contained in the c_p database (full version, incl. molar mass, molar volume, theoretical density, references for c_p (low T, high T), peaks if any (temperature, type, enthalpy), melting and/or decomposition temperature (or triple point), melting (or sublimation) enthalpy, comments) see paper II SOM (and, for future updates, in the data repository). The formula given here is the actually used formula for the c_p in the database if different from the ideal endmember formula. The abbreviation, which is also used for the software and data file names, follows [237] wherever possible; in some cases, we use the chemical formula or invented a new abbreviation. The densities are important for the conversion of modal mineralogy into mass fractions and are taken from various sources [235, 236, 238]; they refer to a temperature of 25 °C, except in the case of ices, where they refer to a temperature midway between 0 K and triple point temperature tr triple point, *anh* anhydrous, P density, \square (atom) vacancy

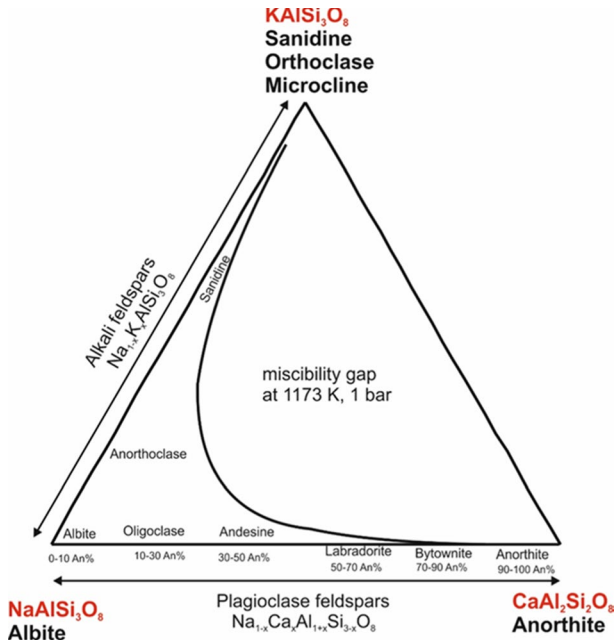


Fig. 8 Compositional phase diagram of the different minerals that constitute the feldspar solid solution. Ternary phase diagram of the feldspars (at 900 °C). Miscibility gap line after (Benisek, Dachs et al. 2010c)

(anorthoclase) and solid solutions between albite and anorthite are called ‘plagioclases’ and have traditional names according to Ca mole fraction x (see Fig. 8).

In extra-terrestrial materials, plagioclase is by far the most abundant feldspar. Sanidine is present but much less abundant.

4.1.1 The Feldspar Polymorphs

We discuss the feldspar polymorphs mainly to clarify the complicated nomenclature. The heat capacity difference Δc_p of the various polymorphs of a feldspar endmember is small, and we will neglect it (using the arithmetic average of c_p data of the polymorphs of a given endmember, where available).

Ordering/disordering reactions of Al and Si on the tetrahedral sites results in the different feldspar polymorphs. For the potassium feldspars, *sanidine*, monoclinic, is the high-temperature form with a disordered Al/Si distribution on the tetrahedral sites. It is found most typically in felsic volcanic rocks such as obsidian, rhyolite, and trachyte. *Orthoclase* is a monoclinic polymorph stable at lower temperatures. Slowly cooled K-feldspar gives *microcline* with a triclinic structure and stable at yet lower temperatures.

For the Na-feldspars, it is generally accepted that there are two stable and one metastable modifications [239]:

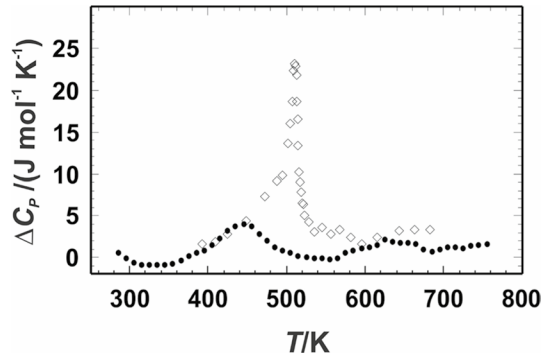


Fig. 9 Excess heat capacity (ΔC_p) of the ordering transition in anorthite, which was defined as C_p Monte Somma— C_p An100 (solid circles) and C_p Pasma— C_p An100 (open symbols), respectively. An100 is a synthetic anorthite crystallized at 1573 K, Monte Somma is a volcanic anorthite (An98), and Pasma is a metamorphic anorthite (An100). From [243]. The average C_p (without the peak) at 510 K is $\sim 272 \text{ J}\cdot\text{mol}^{-1}\cdot\text{K}^{-1}$

(a) Stable modifications monalbite and albite

monalbite [240]: disordered; topochemical and actual symmetry: monoclinic ($C2/m$), corresponding to high sanidine; stable above 1290 °C. Below this temperature it transforms by a displacive transition to a triclinic (C1) albite structure. The most important feature of this transition is that it is very strongly coupled to the degree of Al,Si order. The Al,Si ordering transition is extremely slow compared with the unquenchable displacive transition. The effect on c_p of these transitions is low: the heat capacity difference between ordered albite and analbite is 1.5 % at most, the order–disorder transition at 416 K produces a c_p -step (low > high) of ~ 1 % and the predicted Δc_p peak of albite in thermal equilibrium, originating from the structural phase transition (~ 17 % at 950 K [241]), is so slow that it is unobservable. Thus, we will use average c_p values for all polymorphs of albite.

albite: topochemical and actual symmetry: triclinic $\bar{C}1$; low albite, corresponding to low microcline, ordered form, stable below ≈ 950 °C; high albite, corresponding to high microcline, disordered form, stable between ≈ 950 °C and 1251 °C [241].

(b) Metastable modification analbite

If monalbite is rapidly quenched, it undergoes a rapid displacive transformation to triclinic analbite $C\bar{C}1$ at $T_{displ} \approx 930$ °C to 980 °C (range of literature data). The diffusive transition (ordering of Al/Si distribution) needs time. Because analbite is topochemically monoclinic (with a disordered Al/Si distribution), but metrically triclinic, it is unstable at any temperature.

Summarizing, monalbite and high sanidine are the high-temperature, disordered polymorphs; low albite and low microcline the low-temperature, fully ordered polymorphs; high albite and high microcline the low-temperature, polymorphs with a

slightly disordered Al/Si distribution; and analbite the low-temperature metastable polymorph with disordered Al/Si distribution.

In contrast to Na-feldspar, a K-feldspar that cooled fast from high temperatures (volcanic) will preserve its Al/Si distribution as well as its monoclinic structure because the larger K atom keeps the structure open; sanidine forms from really fast cooling, or later exsolution during metamorphism. Orthoclase (Or) forms from slow cooling.

There is a significant $\bar{C1}$ phase transition in $c_p(T)$ in anorthite at ~ 510 K, which is displacive (fast), but to occur at all, the precise composition and degree of Al/Si ordering is important, it only happens in pure or almost pure anorthite [242]. In ordered anorthite $T_c = 510$ K and the transition is tricritical; in slightly less well-ordered anorthite $T_c^* = 530$ K and the transition is second order.

The effect of this phase transition can be relatively large (Fig. 9, after [243]): The heat capacities of three different anorthite samples show large differences in the temperature range 400 K to 600 K. *Natural An* can show a ~ 500 K structural phase transition ΔC_p in the range 430 K to 580 K peaking at $\sim 23 \text{ J}\cdot\text{mol}^{-1}\cdot\text{K}^{-1}$ ($\sim 8.5\%$), see Fig. 9. No peak was observed in synthetic An by [97]. The 500 K peak is not included in our database for anorthite.

4.1.2 Feldspathoids

Feldspathoids resemble feldspars but have a different structure and much lower silica content. They are a family of rock-forming minerals consisting of aluminosilicates of sodium, potassium, or calcium and having too little silica to form feldspar. There is considerable structural variation, so it is not a true group. We consider nepheline $\text{Na}_3\text{K}(\text{Al}_4\text{Si}_4\text{O}_{16})$, as a common feldspathoid, in the database.

4.2 Pyroxenes (Single Chain Inosilicates)

Pyroxenes are, besides olivines, the primary mineral phases in most primitive meteorites and in many types of non-chondritic meteorites.

Pyroxenes are a group of minerals that share the chemical formula $(\text{M}_2)(\text{M}_1)(\text{Si}, \text{Al})_2\text{O}_6$ [232, 234, 235]. Three pyroxene subgroups have been defined [244] based on occupancy of the M2 site. In low-Ca pyroxenes, the M2 site is occupied by Fe or Mg, in high-Ca pyroxenes by Ca, and in the less common sodium pyroxenes by Na. Because high-Ca pyroxenes (solid solution series between endmembers diopside, $\text{CaMgSi}_2\text{O}_6$, and hedenbergite, $\text{CaFeSi}_2\text{O}_6$) have monoclinic symmetries, they are often referred to as clinopyroxenes. The term orthopyroxenes is commonly used for the orthorhombic low-Ca pyroxene solid solution series with endmembers enstatite ($\text{Mg}_2\text{Si}_2\text{O}_6$) and ferrosilite ($\text{Fe}_2\text{Si}_2\text{O}_6$). See Fig. 10, the well-known ‘pyroxene quadrilateral.’

The enstatite–ferrosilite series ($[\text{Mg}, \text{Fe}]\text{SiO}_3$) contains up to 5 mol.% calcium and exists in three polymorphs, orthorhombic orthoenstatite and (at high temperatures only protoenstatite) and monoclinic clinoenstatite (and the ferrosilite equivalent clinoferrosilite). Increasing the calcium content prevents the formation of the

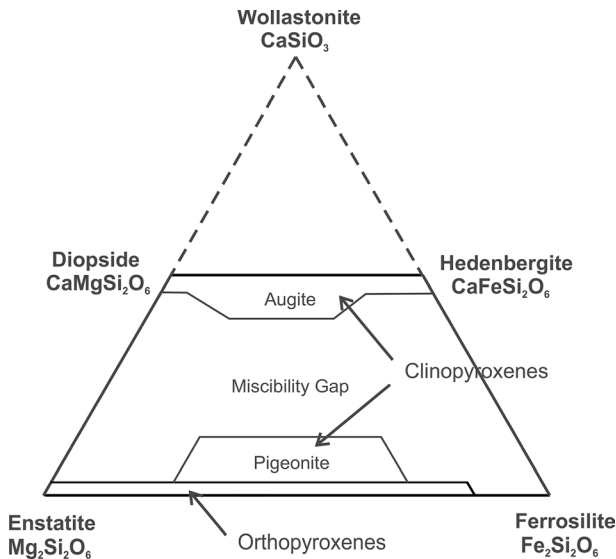


Fig. 10 Pyroxene quadrilateral. Note that the old name ‘hypersthene’ is an orthopyroxene with ~30 % En and rest Fs. Macke (2018 priv. comm.) takes diopside for hypersthene, which is incorrect. Bronzite is a member of the pyroxene group of minerals, belonging with enstatite and hypersthene to the orthorhombic series of the group. Rather than a distinct species, it is really a ferriferous (12 to 30 % iron(II) oxide) variety of enstatite. The augites (Di–Hed) are monoclinic: ‘clinopyroxenes.’ In natural orthopyroxenes, a small amount of Ca (<2%) is always present in the structure

orthorhombic phases and pigeonite ($[\text{Mg,Fe,Ca}][\text{Mg,Fe}]\text{Si}_2\text{O}_6$) only crystallizes in the monoclinic system.

Wollastonite CaSiO_3 and its high-temperature polymorph pseudowollastonite are not really pyroxenes but pyroxenoids.

Other pyroxene families exist; most importantly, the ones containing aluminum. Diopsidic pyroxene in many terrestrial rocks and meteorites commonly contains Al_2O_3 , and the mineral was traditionally called fassaite [245]. Its fully aluminum endmember is Ca-Al-pyroxene CaAlAlSiO_6 = ‘calcium Tschermak’; its official name is now Kushiroite. It is an important mineral in CAIs of carbonaceous chondrites [246]. It forms solid solutions with diopside [98].

Iron-bearing pyroxenes show (magnetic) C_p peaks at cryogenic temperatures.

Aegirine is a member of the sodium-pyroxene family. It is rather rare. Monoclinic aegirine is the sodium-iron endmember of the jadeite–aegirine series and has the chemical formula $\text{NaFeSi}_2\text{O}_6$ in which the iron is present as Fe^{3+} . It is also known as *acmite*.

4.3 Olivines (Neo (Ortho-)silicates)

Olivine $(\text{Mg}^{2+}, \text{Fe}^{2+})_2\text{SiO}_4$ is a common mineral in the Earth’s mantle but weathers quickly on the surface. Olivine rock is called Dunite (>90 % olivine, Fo_{90}). Mg-rich olivine has also been discovered in meteorites (chondrites, pallasites), on the Moon

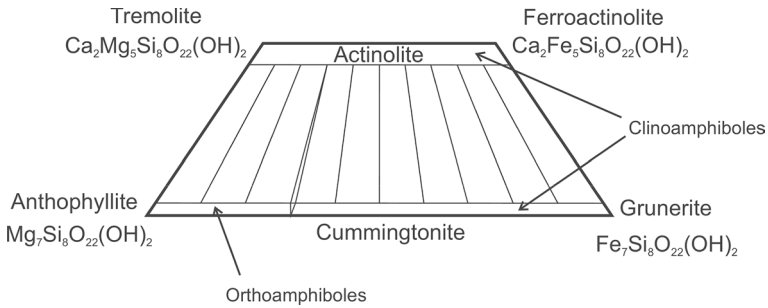


Fig. 11 Amphibole quadrilateral. The orthorhombic anthophyllites (low Ca, ≤ 3.8 at.%) extend up to ~ 30 at.% Fe, the monoclinic cummingtonite–grunerite (low Ca, ≤ 4.5 at.%) series from ~ 30 at.% to 100 at.% Fe. The calcium content of the actinolite series is centered around $2/7 \approx 29$ at.% (referred to total metal cations)

and Mars, falling into infant stars, as well as on asteroid 25,143 Itokawa [232, 234, 235].

The ratio of magnesium and iron varies between the two endmembers of the solid solution series: forsterite (Mg endmember: Mg_2SiO_4) and fayalite (Fe endmember: Fe_2SiO_4). Compositions of olivine are commonly expressed as molar percentages of forsterite (Fo) or fayalite (Fa) (e.g., $\text{Fo}_{70}\text{Fa}_{30}$). Forsterite has a high melting temperature at atmospheric pressure 2163 K, but the melting temperature of fayalite is much lower (about 1490 K). The melting temperature varies smoothly between the two endmembers, as do other properties. Olivine generally incorporates only minor amounts of elements other than oxygen, silicon, magnesium, and iron; in extra-terrestrial materials, Ca is more abundant than Mn or Cr and the Ca-rich kirschsteinite is occasionally present as a secondary phase in chondrites.

4.4 Amphiboles (Double Chain Inosilicates Supergroup)

Amphiboles are found in some meteorites, including SNCs and some chondrites. Hornblende is the most commonly reported but others have also been seen [247].

Amphiboles crystallize into two crystal systems, monoclinic and orthorhombic. In chemical composition and general characteristics, they are similar to the pyroxenes. The chief differences from pyroxenes are that (i) amphiboles contain essential hydroxyl (OH) or halogen (F, Cl) and (ii) the basic structure is a double chain of tetrahedra (as opposed to the single chain structure of pyroxene). Amphiboles (as phyllosilicates) often have cation vacancies, symbolized by \square in chemical formulas [232, 234, 235].

Four of the amphibole minerals are among the minerals commonly called asbestos, they are anthophyllite, riebeckite, the cummingtonite/grunerite series, and the important actinolite/tremolite series (see Fig. 11) Those, however, are very rare to absent in known astro-materials, save for actinolite–tremolite (which is just ‘rare’). Note that another mineral commonly called ‘asbestos’ and common in C chondrites, *chrysotile* $\text{Mg}_3(\text{Si}_2\text{O}_5)(\text{OH})_4$, is *not* an amphibole but a serpentine (Phyllosilicate/Kaolinite–serpentine group).

Hornblende is a complex monoclinic inosilicate series of minerals (ferrohornblende–magnesianhornblende). It is not a recognized mineral in its own right, but the name is used as a general or field term, to refer to a dark amphibole. It can usually be considered an isomorphous mixture of three molecules; a calcium-iron-magnesium silicate, an aluminum-iron-magnesium silicate, and an iron-magnesium silicate [232, 234, 235]. The general formula⁹ can be given as $(K,Na)_{0-1}(Ca,Na,Fe,Mg)_2(Mg,Fe,Al)_5(Al,Si)_8O_{22}(OH)_2$ or $\square(Ca_2)(Z^{2+}_4Z^{3+})(AlSi_7O_{22})(OH,F,Cl)_2$, simpler as $Ca_2(Mg, Fe, Al)_5 (Al, Si)_8O_{22}(OH)_2$.

Simplifying, (no Na, no F), the physical properties of these hornblende endmembers are so similar that using two the following endmembers will be sufficient:

Ferrohornblende: $\square\{Ca_2\}\{Fe^{2+}_4Al\}(AlSi_7O_{22})(OH)_2$.

Magnesianhornblende: $\square\{Ca_2\}\{Mg_4Al\}(AlSi_7O_{22})(OH)_2$.

4.5 Oxides and Hydroxides

4.5.1 Simple Oxides

Here, we have first corundum Al_2O_3 , periclase MgO , rutile TiO_2 , quartz SiO_2 (see below), which are rather inert minerals with high melting points and simple stoichiometry. Lime, (anhydrous) CaO on the other hand, is quite reactive.

Note that TiO_2 occurs naturally in three phases: rutile, anatase, and brookite. Both rutile and anatase are accessory minerals that form small percentages of a vast array of rocks, soils, and sediments. Brookite is much rarer. Rutile is the most common phase in nature, and anatase transforms into rutile above 400 °C to 600 °C.

4.5.2 Quartz and Its Polymorphs

While quartz, SiO_2 , a tectosilicate, oxide and silica mineral, is ubiquitous on Earth (think of common sand), it is, surprisingly, probably not an important phase anywhere else. In meteorites, in lunar regolith: almost no quartz. Apparently not on Mercury [224]. Only locally on Mars, due to aqueous alteration [249]. Maybe Venus has, as suggested by [226] a felsic crust that contains quartz, but the Venera probes have detected no evidence of it in-situ [227].

Quartz has many polymorphs with complicated transformation paths; under low or zero pressure, only α/β -quartz and cristobalite are relevant. Low (α) quartz transforms instantly and reversibly at 843 K into high (β) quartz; above ~1143 K β -tridymite, above 1743 K β -cristobalite is stable, the latter melting at ~1978 K. Metastable cristobalite and tridymite can exist at $T < 1000$ K. High-pressure

⁹ to be precise, a differentiation is necessary depending on normalization to 15 or 13 cations. For normalization to 13 cations: $13 = Si + Ti + Al + Fe + Mn + Mg$ in the T and C (M1, M2, M3) sites. This method excludes Ca from the C sites and Fe^{2+} , Mn and Mg from the B (M4) site. In contrast, for normalization to 15 cations: $15 = Si + Ti + Al + Fe + Mn + Mg + Ca$ in the T, C, and B sites [248].

polymorphs (shocked quartz) are coesite and stishovite, which are metastable at low temperature and pressure.

Just for completeness (and comparison to terrestrial analogs that may contain significant amounts of quartz), the database contains the heat capacity of α -quartz (trigonal low-temperature form), β -quartz (hexagonal high-temperature form, > 573 °C, fast and reversible structural transition lambda peak), tridymite, cristobalite, and amorphous SiO_2 , (silica, lechatelierite) as well as the industrial compound sodium metasilicate (Na_2SiO_3) which has been used in analog materials (regolith simulants, see, e.g., Online Appendix Sect. 5).

4.5.3 Iron Oxides and Hydroxides

Iron forms rather complicated, but fascinating oxides and hydroxides. Iron oxides exist as several different polymorphs which can be divided into two groups: anhydrous (oxides) and hydrous (oxyhydroxides). The more common anhydrous forms include hematite ($\alpha\text{-Fe}_2\text{O}_3$), maghemite ($\gamma\text{-Fe}_2\text{O}_3$), magnetite (Fe_3O_4), and wüstite ($\text{Fe}_{(1-x)}\text{O}$) with magnetite and wüstite containing both ferrous and ferric iron. Stoichiometric wüstite FeO is called ferrous oxide [250].

Magnetite = $\text{FeO}\cdot\text{Fe}_2\text{O}_3 = \text{Fe}^{2+}\text{Fe}^{3+}_2\text{O}_4$, rather than Fe_3O_4 . Mix of Fe-II and Fe-III. At low temperatures, magnetite undergoes a crystal structure phase transition (from a monoclinic structure to a cubic structure) known as the Verwey transition. The Verwey transition occurs around 124 K and the precise temperature, shape, and magnitude of the lambda peak is dependent on grain size, domain state, residual stresses, and the iron–oxygen stoichiometry in complicated, not fully understood ways [115, 141]. The Curie temperature of magnetite is 858 K, producing there a large λ peak in C_p .

Hematite, Fe_2O_3 can be obtained in various polymorphs. $\alpha\text{-Fe}_2\text{O}_3$ has the rhombohedral, corundum ($\alpha\text{-Al}_2\text{O}_3$) structure and is the most common form. It is antiferromagnetic below ~ 263 K (Morin or spin-flip transition temperature), and exhibits weak ferromagnetism between 263 K and the Néel temperature, 955 K. It shows three interesting C_p features, an anomaly at ~ 10 K, visible in the effective Debye- T plot, a very broad bump around 500 K (< 4 %) and a strong λ -peak near 955 K. There is no λ -peak nor anomaly at the Morin temperature.

$\gamma\text{-Fe}_2\text{O}_3$, maghemite, is the ferromagnetic polymorph of hematite. It is Fe-II-deficient, has a cubic structure; it is metastable and converted from the α phase at high temperatures.

Wüstite = Fe_{1-y}O , ideally $y=0$, FeO , is particularly complicated. It is the most reduced variant, ferrous oxide, only Fe^{2+} (and metallic Fe if further reduced). It is typically iron-deficient (classical example of a non-stoichiometric phase, $y > 0$) with compositions ranging from $\text{Fe}_{0.84}\text{O}$ to $\text{Fe}_{0.95}\text{O}$ (eutectoid composition is $\text{Fe}_{0.932\pm 0.004}\text{O}$). Wüstite forms from Fe and Fe_3O_4 (magnetite) at the eutectoid temperature of (847 ± 7) K [142]. It is quenchable and remains metastable at ambient conditions for extended periods, tending to disproportionate to metal and Fe_3O_4 : $4\text{FeO} \rightarrow \text{Fe} + \text{Fe}_3\text{O}_4$ but no transformation was observed at 200 °C and lower [251].

Below 190 K antiferromagnetic ordering is observed in wüstite. It is accompanied by a slight rhombohedral deformation and a peak in C_p , which depends strongly on composition [141, 142].

The oxide-hydroxides of iron may occur in anhydrous ($\text{FeO}(\text{OH})$) or hydrated ($\text{FeO}(\text{OH})\cdot n\text{H}_2\text{O}$) forms. The monohydrate ($\text{FeO}(\text{OH})\cdot\text{H}_2\text{O}$) might otherwise be described as iron(III) hydroxide ($\text{Fe}(\text{OH})_3$), and is also known as hydrated iron oxide or yellow iron oxide.

Iron(III) oxide-hydroxide occurs naturally as four minerals, the polymorphs denoted by the Greek letters α , β , γ , and δ . Goethite (α - FeOOH), lepidocrocite (γ - FeOOH), and akaganéite (β - FeOOH) comprise the majority of the hydrous polymorphs with these materials often containing excess water. One of the most hydrated forms is semi-amorphous ferrihydrite $\text{FeOOH}\cdot n\text{H}_2\text{O}$ but with widely variable hydration [250].

Goethite, α - $\text{FeO}(\text{OH})$, is the main component of rust and bog iron ore.

Akaganéite is the β polymorph, formed by weathering and noted for its presence in some meteorites and the lunar surface. Cl is always present in akaganéite, serving to stabilize the molecular framework (e.g., 0.34 % chlorine by mass [250]). Decomposes > 230 °C.

The γ polymorph *lepidocrocite* is commonly encountered as rust on the inside of steel water pipes and tanks. *Feroxyhyte* (δ) is formed under the high-pressure conditions of sea and ocean floors, being thermodynamically unstable with respect to the α polymorph (goethite) at surface conditions.

Ferrihydrite (Fh) $\text{FeOOH}\cdot n\text{H}_2\text{O}$, officially $\text{Fe}^{3+}_{10}\text{O}_{14}(\text{OH})_2$, also written $(\text{Fe}^{3+})_2\text{O}_3\cdot 0.5\text{H}_2\text{O}$, is a widespread hydrous ferric oxyhydroxide mineral at the Earth's surface, and a (weathering product?) constituent in extra-terrestrial materials. Ferrihydrite only exists as a fine-grained and highly defective nanomaterial. The powder X-ray diffraction pattern of Fh contains two scattering bands in its most disordered state, and a maximum of six strong lines in its most crystalline state. The principal difference between these two diffractions endmembers, commonly named *two-line* and *six-line* ferrihydrites, is the size of the constitutive crystallites. The two-line form is also called hydrous ferric oxides (HFO). Ferrihydrite is a metastable mineral.

Finally, we mention bunsenite, NiO, which is notable as being the only well-characterized oxide of nickel.

4.6 Carbonates, Halides, and Brine Salts

The well-known rock-forming carbonates are of course calcite CaCO_3 , dolomite $\text{CaMg}[\text{CO}_3]_2$, and magnesite MgCO_3 . Iron carbonate, siderite FeCO_3 , is (on Earth) commonly found in hydrothermal veins.

Water-soluble carbonates form *evaporites*: Natrite, Na_2CO_3 (anhydrous; various hydrates have mineral names, e.g., $\cdot 1\text{H}_2\text{O}$ thermonatrite, $\cdot 10\text{H}_2\text{O}$ natron), and the bicarbonate nahcolite, NaHCO_3 .

Brine salts Ceres' most famous bright faculae in Occator Crater probably originated from the recent crystallization of brines that reached the surface from below;

the brine composition is thought to be [252] a mixture of $\text{NaCl}\cdot 2\text{H}_2\text{O}$ (hydrohalite) with smaller amounts of NH_4Cl (ammonium chloride), Na_2CO_3 (natrite), and ammonium bicarbonate (NH_4HCO_3).

Thus, we include also the halides halite NaCl , and sylvite KCl , as well as the ammonia salts NH_4Cl (ammonium chloride) and ammonium bicarbonate (NH_4HCO_3) in the database.

4.7 Phosphates, Sulfates, and Related Minerals

As common *phosphate minerals*, we include fluorapatite $\text{Ca}_{10}(\text{PO}_4)_6\text{F}_2$ and hydroxyapatite $\text{Ca}_{10}(\text{PO}_4)_6(\text{OH})_2$; they form a solid solution series.

The most common *sulfates* are the ones of calcium, magnesium, and iron: anhydrite CaSO_4 , gypsum $\text{CaSO}_4\cdot 2\text{H}_2\text{O}$, anhydrous magnesium sulfate MgSO_4 and epsomite $\text{MgSO}_4\cdot 7\text{H}_2\text{O}$, and iron(II)sulfate FeSO_4 . Note that epsomite is extremely soluble in water, and loses crystal water already slightly over room temperature.

Iron(II)sulfate FeSO_4 is a weathering product of FeS (or meteoritic iron with acid rain) in meteorite finds and is usually hydrated, $\text{FeSO}_4\cdot n(\text{H}_2\text{O})$. These compounds exist most commonly as the heptahydrate ($n=7$) but are known for several values of n ($n=1, 4, 5, 6, 7$: Szomolnokit, Rozenite, Siderotil, Ferrohexahydrate, Melanterite) [232, 234, 235].

4.8 Sulfides and Related Minerals

Sulfides are an important accessory mineral in meteorites, we list troilite FeS , pyrite FeS_2 , pyrrhotite $\text{Fe}_{1-x}\text{S}_x$ ($x=0 \dots 0.2$), and pentlandite $(\text{Fe},\text{Ni})_9\text{S}_8$.

4.8.1 Pyrite FeS_2

Iron (II) Disulfide FeS_2 , is used as a replacement for troilite in meteorite analogs. It is dimorph, with pyrite (cubic) and marcasite (orthorhombic) phases; the latter is less stable than pyrite and decays in ambient air within a few years; heating marcasite $> 400^\circ\text{C}$ produces pyrite.

Decomposition of pyrite into pyrrhotite and elemental sulfur starts at 813 K to 843 K; at around 973 K, $p(\text{S}_2)$ is about 1 atm [235].

4.8.2 Pentlandite $\text{Fe}_{4.5}\text{Ni}_{4.5}\text{S}_8$

It is the most common terrestrial iron–nickel sulfide, compare troilite. It is non-magnetic.

Berezovskii et al. [77] measured the c_p of pentlandite ($\text{Fe}_{4.60}\text{Ni}_{4.54}\text{S}_8$) between 6 and 306 K. There are no observable phase transitions in this temperature range, but a clear γT term indicating electronic heat capacity typical of conductors. The metal–sulfur ratio of pentlandite implies unusual valence of Fe and Ni atoms; metal bonding has been proposed. According to Warner et al. [253], pentlandite has a 2nd-order lambda transition between 323 and 473 K. According to Sugaki and

Table 6 Phases of meteoritic iron [232]

Mineral	Formula	Nickel (Mass-%)	Crystal structure	Notes
Antitaenite	$\gamma_{\text{Low Spin}}^-(\text{Ni},\text{Fe}); \text{Fe}_{-3}\text{Ni}$	20 to 40	fcc	Only approved as a variety of taenite by the IMA. Low magnetic moment
Kamacite	$\alpha\text{-(Fe,Ni)}; \text{Fe} \sim_{0.9}\text{Ni} \sim_{0.1}$	5 to 10	bcc	Same structure as <i>ferrite</i>
Taenite	$\gamma\text{-(Ni,Fe)}; \text{Ni}_{-0.5}\text{Fe}_{-0.5}$	20 to 65	fcc	Same structure as austenite High magnetic moment
Tetrataenite	(FeNi)	48 to 57	Tetragonal	< 320 °C
Awaruite	Ni_3Fe	~ 1/3	Cubic	

Kitakaze [254] there is a low phase < 584 °C, an order–order phase transition in the range 580 °C to 620 °C; decomposition starts at 613 °C, pentlandite melts over the range 865 °C to 952 °C.

4.8.3 Troilite FeS, Pyrrhotite Fe_{1-x}S

Troilite FeS is a typical example for a non-stoichiometric compound; it is rarely found on Earth as $\text{Fe}_{1.00}\text{S}$ but rather pyrrhotite Fe_{1-x}S , while it is near-stoichiometric in iron meteorites (where it is in equilibrium with metallic Fe). Most troilite on Earth is of meteoritic origin. One iron meteorite, Mundrabilla, contains 25 to 35 volume percent troilite [255]. The most famous troilite-containing meteorite is Canyon Diablo. As troilite lacks the iron deficiency which gives pyrrhotite its characteristic magnetism, troilite is non-magnetic [232, 234, 235].

Iron-deficient pyrrhotite has the formula $\text{Fe}_{(1-x)}\text{S}$ ($x=0$ to 0.2). Thermodynamic properties of the α/β phase transformation in terrestrial troilite vary systematically with prior thermal history of the troilite; both the transition temperature and enthalpy change for the α/β transformation decrease with increasing maximum temperature of prior heat treatment. DSC measurements on troilite from various meteorites indicate clear differences in the α/β thermodynamic properties that are consistent with differences in the natural thermal histories of the meteorites [256].

The heat capacity of troilite has been measured [257] for 5 to 1000 K. It exhibits transitions due to disappearance of the lower-temperature antiferromagnetic or ferromagnetic phase. Stoichiometric FeS shows three transitions in the temperature range 300 K to 1000 K, with heat capacity maxima at 419.6 K, 440 K, and 590 K; the Néel temperature is near 590 K. The low-temperature transition originates from structural changes, whereas the higher ones are mainly of magnetic origin. For $\text{Fe}_{0.98}\text{S}$ only one additional transition takes place, with maximum heat capacity at $T=405$ K. $\text{Fe}_{0.89}\text{S}$ exhibits a transition 30 K below the Néel temperature. The maximum heat capacity at $T=560$ K is due to a structural transition coupled to a magnetic-order-to-order transition. In addition, a smaller effect, related to a phase reaction, is observed in the range $T=650$ K to 760 K.

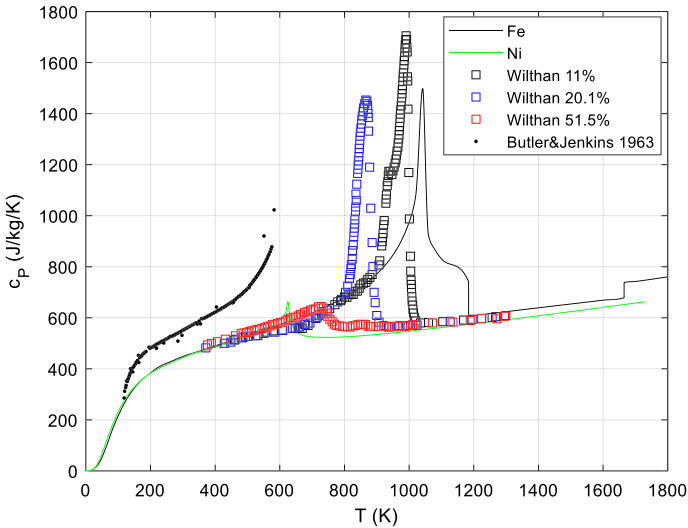


Fig. 12 Specific heat of FeNi alloys [261] together with the curves for pure Fe and pure Ni. In alloys, the iron $\alpha \rightarrow \gamma$ transition at ~ 1190 K seems to vanish and the amplitude and position of the magnetic Ni transition varies systematically with composition. The black dots are the (digitized) data of [262], they seem systematically off

4.9 Meteoritic Iron

Meteoritic iron FeNi is mainly composed of iron and nickel, with Ni content up to 65 % and minor cobalt (0.25 % to 0.77 % Co; Fe + Ni + Co make > 95 %). The bulk of meteoric iron consists of *taenite* and *kamacite*. Taenite is a face-centered cubic and kamacite a body-centered cubic iron–nickel alloy (plessite is a fine-grained intergrowth of kamacite and taenite), see Table 6.

Meteoritic iron can be distinguished from telluric iron by its high Ni content and by its microstructure, notably, the famous Widmanstätten patterns, interleaving of kamacite and taenite bands or ribbons called lamellae. They form when meteoric iron cools and kamacite is exsolved from taenite. They appear, however, only in octahedrites, with an average Ni content of 5 % to 18 %, not in hexahedrites which contain only kamacite with 4 % to 7 % average Ni content, nor in ataxites (only taenite) with average Ni content > 15 % [232].

Yang et al. [258] determined the Ni content and crystal structure of the various regions in meteoritic metal with < 50 nm resolution, revealing a very clear compositional zoning.

The typical composition of meteoritic iron is [259]

- 64 % to 98 % kamacite [260], rest taenite/plessite, and sometimes 58 % to 8 % cohenite and graphite, minor sulfides
- Ni content in kamacite: 6.8 % to 8.2% (average 7.1 ± 0.7), a bit lower (6.0 %) near taenite borders
- Ni content in taenite: 29 % to 60 %

- For example, the Canyon Diablo meteorite has typically 87 % kamacite with 6.8 % Ni, 2.1 % taenite with ~46 % Ni, 1.1 % plessite with ~26 % Ni, 6.5 % cohenite, thus on average 7.17 % metallic Ni as measured. Often, meteoritic iron is associated with schreibersite (Fe,Ni)₃P.

Using a ‘typical’ meteoritic iron $c_p(T)$ curve for ~10 % Ni is possible below ~400 K, since at low temperatures the composition dependence is small (see Fig. 12). At higher temperatures, the magnetic transition peak depends strongly on composition (both peak temperature and shape).

Since the c_p of FeNi is much smaller (factor 2) than that of silicates, meteorites (or regolith) containing FeNi have also a lower c_p . However, weathering of meteorites can change the specific heat significantly, if the meteorite contains elemental iron and nickel (the c_p of the oxides is significantly higher than the c_p of the elemental metals), see [27]. Even without knowing the composition (the content of metal), the bulk or grain density ρ correlates well with c_p , since FeNi is also much denser (7800 kg·m⁻³ compared to ~3000 kg/m³ for silicates) and $c_p(\rho)$ may be approximated by the relation [263]: $c_p = a + b/\rho_b$, where a and b are constants (at 298.15 K we calculate $a = 262.81$ J/(kg·K), and $b = 1.4616 \cdot 10^6$ J/(K·m³)).

There is a dearth of accurate experimental data on meteoritic iron, we only found Butler and Jenkins [262] who used an octahedrite sample of the Canyon Diablo meteorite. These data, obtained by a Xe lamp flash method, seem to be ~40 % too high systematically (Fig. 12).

In the field of meteoritics, the equilibrium Fe–Ni phase diagram is of great importance. The phase relations between the alpha phase (kamacite) and the gamma phase (taenite) are best described by means of the Fe–Ni phase diagram [258, 264]. The low-temperature region of the phase diagram has been constructed with the help of meteoritic iron analyses, since this metal took ~10⁸ years to cool [265] and is closest to equilibrium (even if actually metastable). At 300 °C, it takes more than 10⁴ years for one atomic jump to occur; atomic diffusion is already very slow at 400 °C and effectively ceases at 200 °C [266].

The Curie point of the α -phase (Kamacite) is about $T_c^{bcc}(\text{K}) = 1043x_{Fe} + 456x_{Ni} + 385.8x_{Fe}x_{Ni}$, with nickel and iron content x_{Ni} , x_{Fe} in atomic fraction. The Curie temperature of the fcc (γ) ferromagnetic cubic phase varies with nickel content in a complicated fashion between less than 300 K (actually 0 for metastable phases) and close to 900 K [267]. If at least two main phases are present in meteoritic iron (α , γ), two magnetic phase transitions at different temperatures are expected, at ~1030 K for α and ~800 K for the γ phases.

Modeling the specific heat of FeNi alloys with arbitrary Ni content for the phases could possibly be done using the empirical CALPHAD approach described in [268] based on [269].

4.9.1 Metal Carbides: Cohenite and Cementite

Carbides are found associated to meteoritic iron FeNi: Cementite, iron carbide Fe₃C and more general cohenite, iron–nickel carbide (Fe,Ni)₃C. For example, the Canyon Diablo meteorite contains 5 % to 8 % c cohenite [259].

The limit of Ni solubility in cohenite (Fe,Ni,Co)₃C is not known experimentally. Lunar cohenite containing 7.0 wt.% Ni has been observed in Apollo 17 soil fines. Meteoritic cohenite apparently has a Ni content of 2 wt% to 3 wt%. Terrestrial samples contain just over 3 wt.% Ni. However, since pure Ni₃C has been synthesized it is reasonable to expect a continuous solid solution series between Fe₃C and Ni₃C [270].

Pure iron carbide Fe₃C is called cementite. It is opaque and strongly ferromagnetic below the Curie point, 485 ± 5 K. For both carbides, the melting point ≈ 2110 K. Cohenite decomposes > 996 K.

While cementite is thermodynamically unstable for $p < 40$ kbar, eventually and very slowly being converted to Austenite/Kamacite and graphite, it does not decompose on heating at temperatures below the eutectoid temperature (723 °C).

4.10 Phyllosilicates (Sheet Silicates)

The nomenclature of phyllosilicates (and ‘clay minerals’) is complicated and changed over time. All phyllosilicate minerals are hydrated, with hydroxyl groups and water (in the case of clays) attached; they can form by aqueous alteration. However, carbonaceous chondrites frequently contain partly or completely dehydrated phyllosilicates, and such phases are likely present on asteroids Ryugu and Bennu [271]. In meteorites, the serpentines and montmorillonites (especially saponite) are the most frequently encountered phyllosilicates, micas are rare—mineral composition tables, however, often only list the constituents in some broad category, like ‘saponite’ or ‘serpentine.’

Phyllosilicates are divided in a number of groups and subgroups, with mineral species making up the subgroups. We just describe the most relevant ones. Note that nomenclature is not fully consistent in the literature; presently recommended is [272]. In a phyllosilicate (sheet silicate), a ‘sheet’ or layer can be composed either of 1 tetrahedral: 1 octahedral sheet (1:1 layer), 2 tetrahedral: 1 octahedral sheet (2:1 layer), or the latter with a brucitic sheet in the interlayer (2:1:1 layer type).

Phyllosilicates, especially the smectite (clay) minerals, are among the most complex inorganic compounds in nature. They display a complex and variable composition and (like amphiboles) often contain lattice vacancies; endmember compositions can often be not easily defined or the sheer number of ideal endmembers would be overwhelming. Thus, specific heat data are not available for any possible composition of a phyllosilicate we find naturally. We sometimes have to improvise, using analog minerals as proxies (possibly scaled for mean atomic mass) or used predicted c_p values from models (e.g., [154]) or ab initio calculation (DFT). Measured specific heat data from the literature are often not directly usable; natural samples often do not have a ‘reasonable’ endmember composition, and impurities have to be determined and quantified such that the contribution of impurities can be subtracted from the measured properties. The hydration state of the mineral is another important point to consider, particularly for swelling clay minerals. Indeed, hydration energies are not negligible and depend on the nature of the clay mineral, interlayer cations, and relative humidity (RH). Calorimetric measurements have to be performed for

a fixed and known hydration state. Blanc et al. propose a consistent suite of models for the prediction of (among other properties) $C_p(T)$ for anhydrous clay minerals, parameterized using calorimetric data from the literature [154]. Starting from the anhydrous state, the C_p of a given hydration state can be calculated by adding the contribution of hydrate water to specific heat (details see chapter 2.12.1 below).

The *serpentine–kaolinite group* has two subgroups, serpentines and kaolinites.

The *serpentines* describe a group of common rock-forming hydrous magnesium iron phyllosilicate $(\text{Mg, Fe})_3\text{Si}_2\text{O}_5(\text{OH})_4$ minerals. Common are iron-bearing cronstedtite, Mg-bearing antigorite/lizardite/chrysotile (‘asbestos’) $\text{Mg}_3\text{Si}_2\text{O}_5(\text{OH})_4$, berthierine, and others. They decompose at $\sim 750^\circ\text{C}$ (chrysotile).

Cronstedtite is a complex, iron-rich serpentine, $\text{Fe}^{2+}_2\text{Fe}^{3+}(\text{Si, Fe}^{3+})\text{O}_5(\text{OH})_4$, substitution between Si and Fe^{3+} is variable, we assume Fe:Si 1:1 at least: $\text{Fe}^{2+}_2\text{Fe}^{3+}_2\text{SiO}_5(\text{OH})_4$ but rather $\text{Fe}^{2+}_2\text{Fe}^{3+}(\text{SiFe}^{3+})\text{O}_5(\text{OH})_4 = \text{Fe}^{2+}_2\text{Fe}^{3+}_2\text{SiO}_5(\text{OH})_4$

Kaolinite $\text{Al}_2\text{Si}_2\text{O}_5(\text{OH})_4$ has one tetrahedral sheet of silica (SiO_4) linked through oxygen atoms to one octahedral sheet of alumina (AlO_6) octahedra. Kaolinite undergoes a series of phase transformations upon thermal treatment in air at atmospheric pressure. Any c_p must state the water content and is restricted to $\leq 550^\circ\text{C}$, where non-reversible dehydration begins.

The *pyrophyllite/talc group* contains *Talc* as its most relevant member.: $\text{Mg}_3\text{Si}_4\text{O}_{10}(\text{OH})_2$ (iron-bearing: $\text{Fe}^{2+}_3\text{Si}_4\text{O}_{10}(\text{OH})_2$, Tschermak: $\text{Mg}_2\text{Al}_2\text{Si}_3\text{O}_{10}(\text{OH})_2$). Pyrophyllite is $\text{Al}_2\text{Si}_4\text{O}_{10}(\text{OH})_2$.

The *chlorite*¹⁰ *group* The name *chlorite* is from the Greek *chloros* ($\chi\lambda\omega\rho\acute{o}\varsigma$), meaning ‘green,’ in reference to its color. They do not contain the element chlorine, also named from the same Greek root. Layer type 2:1:1. The typical general formula is $(\text{Mg, Fe})_3(\text{Si, Al})_4\text{O}_{10}(\text{OH})_2 \cdot (\text{Mg, Fe})_3(\text{OH})_6$. Most relevant are clinocllore, Mg-rich, and chamosite which is Fe-rich.

The *Mica Group and Subgroups*

Muscovite $\text{KAl}_2[(\text{OH, F})_2|\text{AlSi}_3\text{O}_{10}]$ is the most common mica.

Biotite $\text{K}(\text{Mg, Fe})_3\text{AlSi}_3\text{O}_{10}(\text{F, OH})_2$, or $\text{K}(\text{Mg, Fe}^{2+}, \text{Mn}^{2+})_3[(\text{OH, F})_2|(\text{Al, Fe}^{3+}, \text{Ti}^{3+})\text{Si}_3\text{O}_{10}]$, is another common mica, primarily a solid solution series between the iron-endmember *annite* $\text{KFe}_3^{2+}\text{AlSi}_3\text{O}_{10}(\text{OH})_2$, and the magnesium-endmember *phlogopite* $\text{KMg}_3\text{AlSi}_3\text{O}_{10}(\text{OH})_2$; more aluminous endmembers include *siderophyllite* $\text{KFe}^{2+}_2\text{Al}(\text{Al}_2\text{Si}_2)\text{O}_{10}(\text{F, OH})_2$ (rare).

The chemical variability of biotites is dominated by Fe–Mg exchange, and the Tschermak substitution $[(\text{Fe, Mg})^{\text{oct}} + \text{Si}^{\text{tet}} = \text{Al}^{\text{oct}} + \text{Al}^{\text{tet}}]$. There are four end-member components used to describe such biotite compositions:

¹⁰ There is some confusion concerning the nomenclature of serpentine and chlorite minerals: In the older literature, the term chamosite was generally applied to minerals in ironstone deposits which frequently contain both Fe serpentine and Fe chlorite. Following [272] we propose to use “clinocllore” and “chamosite” for the Mg and Fe endmembers of the chlorite group minerals, and “amesite” and “berthierine” for their analogs in the serpentine subgroup minerals.

Table 7 Assumed reference (simplified, idealized) formulae for common phyllosilicates in modal analyses of meteorites

Chrysotile	$Mg_3(Si_2O_5)(OH)_4$
Berthierine	$(Fe^{2+}, Fe^{3+}, Al)_3(Si, Al)_2O_5(OH)_4$
Cronstedtite	$(Fe^{2+}Fe^{3+})_3(Si, Fe^{3+})_2O_5(OH)_4$ iron end; but usually contains some Mg: $(Mg, Fe)_3Si_2O_5(OH)_4$
Saponite–serpentine	$Mg_3(Al, Si_{4-x}O_{10})(OH)_2 \cdot 4H_2O$, $x \sim 0.33$
Saponite, general formula	$(Ca_{0.5}Na)_{0.3}(Mg Fe^{2+})_3(Si Al)_4O_{10}(OH)_2 \cdot 4H_2O$ [232] or $Ca_{0.25}(Mg, Fe)_3((Si, Al)_4O_{10})(OH)_2 \cdot n(H_2O)$, typically 3:1 for Si:Al and 1:1 or 1:2 for Mg:Fe, thus (next line)
Saponite, typical ^a	$Ca_{0.25}MgFe_2Si_3AlO_{10}(OH)_2 \cdot 4(H_2O)$, molar mass $451.2613 + n \cdot 18.0153 \text{ g} \cdot \text{mol}^{-1}$
Saponite (Orgueil ^a)	$(Mg_{2.55}Fe^{2+}_{0.45})(Si_{3.46}Al_{0.54})O_{10}(OH)_2 \cdot nH_2O$ ($n \approx 4$ if fully hydrated)
Serpentine (Orgueil ^a)	$(Mg_{2.55}Fe_{0.45})Si_2O_5(OH)_4$ (no crystal water)

^aAfter Bland, Cressey et al. [273] who use the Orgueil average serpentine and saponite compositions of Tomeoka and Buseck [1, Table 2].274

$KFe_3[(OH)_2AlSi_3O_{10}]$: Annite (Ann)
 $KMg_3[(OH)_2AlSi_3O_{10}]$: Phlogopite (Phl)
 $KAlFe_2[(OH)_2Al_2Si_2O_{10}]$: Siderophyllite (Sid)
 $KAlMg_2[(OH)_2Al_2Si_2O_{10}]$: Eastonite (Eas)

Smectites (often imprecisely called *clay minerals*) are hydrous aluminum phyllosilicates, sometimes with variable amounts of iron, magnesium, alkali metals, alkaline earths, and other cations, $A_{0.3}D_{2-3}[T_4O_{10}]Z_2 \cdot nH_2O$. Subgroups include montmorillonite, saponite, nontronite, and vermiculite.

Montmorillonite $(Na, Ca)_{0.33}(Al, Mg)_2(Si_4O_{10})(OH)_2 \cdot n(H_2O)$ is a 2:1 phyllosilicate mineral (meaning that it has two tetrahedral sheets of silica sandwiching a central octahedral sheet of alumina) characterized as having greater than 50 % octahedral charge.

Saponite is trioctahedral. $Ca_{0.25}(Mg, Fe)_3((Si, Al)_4O_{10})(OH)_2 \cdot n(H_2O)$

Vermiculite, $Mg_{0.7}(Mg, Fe, Al)_6(Si, Al)_8O_{20}(OH)_4 \cdot 8(H_2O)$ forms by the weathering or hydrothermal alteration of biotite or phlogopite. It undergoes significant expansion, then exfoliation when heated.

Other important phyllosilicates

Palygorskite, also known as *Attapulgitite*, is $(Mg, Al)_4[OH](Si, Al)_4O_{10}]_2 \cdot (4+4) H_2O$.

Illite is a group of closely related non-expanding clay minerals similar to micas. Structurally, illite is quite similar to muscovite with slightly more silicon, magnesium, iron, and water and slightly less tetrahedral aluminum and interlayer potassium. The chemical formula is given as $(K, H_3O)(Al, Mg, Fe)_2(Si, Al)_4O_{10}[(OH)_2, (H_2O)]$, but there is considerable ion (isomorphic) substitu-

tion. The iron-rich member of the illite group is glauconite. A typical empirical formula is $K_{0.65}Al_{2.0}Al_{0.65}Si_{3.35}O_{10}(OH)_2$.

In Table 7 we list the simplified reference formulae, for some common phyllosilicates, we assume if in modal analyses for example, no explicit empirical formula is given.

4.11 Hydrated Minerals

Dehydrated phyllosilicates are common among carbonaceous chondrites, and are probably present in the regoliths of many asteroids. For example, the carbonaceous chondrite material in HED meteorites includes dehydrated materials, probably heated during impact into the regoliths. On the other hand, all possible hydration stages are found in certain natural phyllosilicates, so we need a correlation for the heat capacity of a given amount of hydrate (crystal) water (note that, e.g., serpentine does not have crystal or hydrate water). Swelling clay minerals can incorporate, between their sheet silicate layers, much more hydration water, of the order of 10 % by mass or more. The thermodynamics of hydration of clays is in fact an active research field and quite complex [143, 154, 275, 276]. Note that from meteorites, one can never be sure that the hydrate water found is only extra-terrestrial!

The ‘water content’ of a ‘hydrated’ mineral can be misleading [277]. It usually means ‘all mass loss upon heating to ~770 °C’ which comprises molecular water (adsorbed), mesopore, or crystal water, release of H₂O from (oxy-)hydroxide minerals like ferrihydrite and goethite, but also hydroxyl groups (–OH) from phyllosilicates.

According to Garenne et al. [277] the loss of mass¹¹ between 25 °C and 200 °C is due to the adsorbed water and the water in 2 nm to 50 nm pores (mesopores) and this range is most easily contaminated by terrestrial water.¹²

The hydrogen quantity in carbonaceous chondrites can be inferred from TGA as different hosts:

- (i) weakly bonded H₂O (loss between 25 and 200 °C),
- (ii) H₂O in hydroxides (200 °C to 400 °C),
- (iii) –OH from phyllosilicates (400 °C to 770 °C) and
- (iv) a high *T* loss (calcium carbonates and sulfates, 770 °C to 900 °C).

For anhydrous clay minerals dihydroxylation begins at temperatures, depending on the mineral, of 300 °C to 600 °C. For hydrated phases, loss of water may begin close to 300 K [143]. For the hydrous serpentine cronstedtite, MacKenzie and Berezowski [279] found only loss (i) of ~0.7 % of surface adsorbed water up to 200 °C; oxidation of Fe²⁺ to Fe³⁺ sets between 200 and 320 °C, and a further loss

¹¹ 0.3 % to 5 %, sometimes up to 10 %, depending on mineral, grain size, mesoporosity and heating rate [278]

¹² which can be removed by heating to 127 °C, in high vacuum, for 3 days [278]

of hydroxyl water for > 400 °C. Natural smectites like saponites start to metamorphose in the range 200 °C to 250 °C in chlorites and illite, while their mass loss below 200 °C (~ 10 %) corresponds to the desorption of physically adsorbed water and interlayer water associated with interlayer cations [280].

We will focus on (i) here, weakly bonded H_2O .

Example for hydrate water mass fraction: a typical saponite is $Ca_{0.25}(Mg_{0.8}Fe_{0.2})_3Al_{0.5}Si_{3.5}O_{10}(OH)_2 \cdot n(H_2O)$; $M = 407.66 + n \cdot 18.015$. If $n = 4$, we have 17.7 % by mass water in the saponite, and with a typical saponite content of say 33 % in a CI meteorite, there is 5.8 weight-% ‘saponite hydrate’ water in the meteorite.

4.11.1 The Specific Heat Contribution of Water in Hydrated Minerals

Physisorbed, excess¹³ or crystal water in minerals has a reproducible specific heat contribution $C_p(\text{water})$ so we can write:

$$C_p(\text{anhydrous}, X) = C_p(\text{hydrated}, X \cdot nH_2O) - n \cdot C_p(\text{water}) \quad (18)$$

Water adsorbed at the 2 to 3 lower ‘layers’ behaves quite differently from bulk water. It is at least partially ordered, does not freeze, and its molecular mobility was shown to depend largely on hydrogen bond interactions between the adsorbed water molecules and the $-OH$ groups on the surface. The fourth layer is transitional, and further layers are similar to bulk water [281, 282]. Also proper crystal water is normally ordered, ‘ice-like.’ Thus, $C_p(\text{water})$ can be treated as $C_p(\text{ice Ih})$, just extrapolated for $T > 273.16$ K which is not too problematic as the ice $C_p(T)$ curve is fairly linear there.

Majzlan et al. [283] fitted the bulk Ih C_p data to the following approximate correlation equation

$$C_p(\text{ice Ih}) = n_1 D(\theta_1/T) + n_2 D(\theta_2/T) + m_1 E(T_{E,1}/T) + m_2 E(T_{E,2}/T) \quad (19)$$

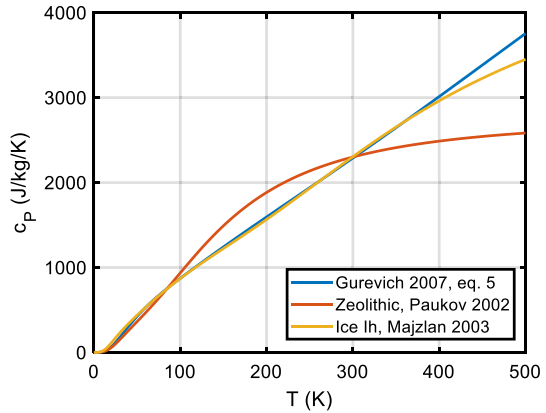
with D and E the Debye resp. Einstein functions, $\theta_1 = 126.77$ K, $n_1 = 0.3103$; $\theta_2 = 392.77$ K, $n_2 = 0.60133$; $T_{E,1} = 652.91$ K, $m_1 = 0.52$, $T_{E,2} = 1388.98$ K, $m_2 = 2.105$.

Note the rather high specific heat of water (ice) compared to silicates adding water almost always increases c_p of a sample!

Using these equations, the heat capacity of water ice Ih at 298.15 K is predicted to be 41.28 J/(mol·K). Note that there are possible phase transitions of water (ice) in larger pores which include a glass transition of amorphous ice (Ia) at 120 K to 140 K and subsequent crystallization to cubic ice (Ic); transformation of cubic ice to hexagonal ice (Ih) at 160 K to 210 K; melting of ice Ih at 273.15 K [283]. None of these transitions are observed in the heat capacity of excess or hydrate water.

¹³ I.e., water that is retained even after prolonged evacuation and storage in argon.

Fig. 13 Bounds on crystal water CP contribution. It appears that the curve given by Gurevich 2007 is a good estimate for crystal water, we use it as our default



Experimentally, from the measured C_p of epsomite and anhydrous magnesium sulfate, Gurevich et al. [284] derived the C_p of crystal hydrate water in the range 0 K to 303 K (and probably higher temperatures as extrapolation) as

$$C_p^0(T)\{H_2O(cr)\} = a_0 T(C_V)^2 + C_V$$

$$C_V = 3 \left[(1/3) \sum_{j=1}^3 a_j D_j(\theta_j/T) + a_4 E(\theta_E/T) + a_5 K(\theta_L/T, \theta_U/T) \right] \tag{20}$$

with the Debye, Einstein, and Kieffer¹⁴ functions $D(\theta_j/T)$, $E(\theta_E/T)$, $K(\theta_L/T, \theta_U/T)$ and the fitted constants:

$$a_0 \text{ (J}\cdot\text{mol}^{-1}) \quad 1.4689 \times 10^{-5}$$

$$a_1 \quad 0.33333$$

$$a_2 \quad 0.33333$$

$$a_3 \quad 0.33333$$

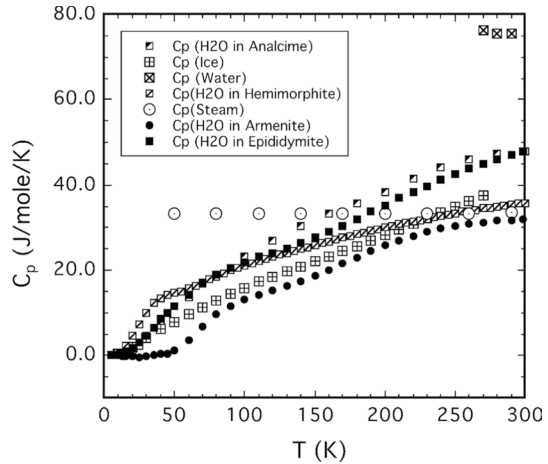
$$a_5 \quad 0.33333$$

$$a_5 \quad 0.33333$$

$$a_5 \quad 0.33333$$

¹⁴ ‘optical continuum’ [61]. The integral, Eq. 21 can also be very precisely approximated by a new Padé approximant, see Online Appendix 1.1.

Fig. 14 Heat capacity behaviour of confined H₂O in armenite and epididymite as well as for hemimorphite [289] and analcime [286] at 0 K < T < 300 K. The squares with e+ symbol are the C_p of ice [290], the squares with the symbol the C_p of super-cooled liquid water [291] and the circles with the symbol the C_p of ideal H₂O gas [292]. (from [287], their Fig. 9)



θ_1 (K)	171
θ_2 (K)	287
θ_3 (K)	671
θ_E (K)	2047
θ_L (K)	484
θ_U (K)	1444

$$K(\theta_L/T, \theta_U/T) \equiv \frac{3R}{\theta_L/T - \theta_U/T} \int_{\theta_L/T}^{\theta_U/T} \frac{x^2 \exp(x)}{(\exp(x) - 1)^2} dx \tag{21}$$

This correlation for the heat capacity of crystal water gives a curve very similar to that for ice Ih of Majzlan et al. [283], see Fig. 13. We use Eq. 20 as our standard curve for adsorbed, excess, and hydrate water. It can probably be used with reasonable accuracy (better 10 %) up to ~500 K. For even higher temperatures, one can use the general H₂O curve of Robertson [99], $C_p [J \cdot mol^{-1} \cdot K^{-1}] = 85.285 - 0.00155 T - 537000/T^2 - 620.9/\sqrt{T} - 1.226 \times 10^{-6} T^2$, 298 K to 1500 K. More specifically, for all smectite endmembers as well as Ca- and Mg-muscovite and -phlogopite the high-temperature C_p, as a function of hydration, has been modeled by Vidal and Dubacq [275].

Viellard [276] gives detailed C_p mostly for clays, but also other minerals, in the high-temperature range.

The heat capacity of water in zeolites (not a common mineral group in astro-material) or microporous minerals is different to the standard correlation (compare Fig. 13), it has been measured and fitted to Eq. 22 by Paukov et al. [285] on

the paranatrolite–tetranatrolite pair and the analcime–dehydrated analcime data of [286].

$$\Delta C_p^{zeo}(T) = \frac{1}{3}D(\theta_l/T) + \frac{2}{3}D(\theta_{tr}/T) + E(T_E/T) \quad [\text{J} \cdot \text{mol}^{-1} \cdot \text{K}^{-1}] \quad (22)$$

This ‘zeolithic’ water heat capacity is, however, not well constrained above ~ 200 K, where an anomalous behavior resembling a glass transition appears in the data.

With the fitted constants for natrolite, $\theta_l = 175$ K, $\theta_{tr} = 450$ K, and $T_E = 583$ K (and for analcime, $\theta_l = 230$ K, $\theta_{tr} = 230$ K, and $T_E = 525$ K).

A more physical analysis has been performed by Geiger et al. [287] who also measured the water heat capacity in various minerals with microporous networks (see also [288]).

A collection of results is shown in Fig. 14, from which we conclude that, at least for microporous minerals, the actual water heat capacity depends on the mineral and can vary by roughly $\pm(4.3 + 0.014 T)$ J/mol/K, $30 \leq T \leq 300$ K.

4.12 Rare Minerals

They do appear sometimes in astro-materials. We collected C_p data on the following minerals (non-exhaustive list) [232, 234, 235].

4.12.1 Garnets

Garnets are hard, abrasive nesosilicates having the general formula $X_3Y_2(\text{SiO}_4)_3$. The X site is usually occupied by divalent cations (Ca, Mg, Fe, Mn)²⁺ and the Y site by trivalent cations (Al, Fe, Cr)³⁺. The garnet endmember minerals pyrope $\text{Mg}_3\text{Al}_2(\text{SiO}_4)_3$, almandine $\text{Fe}_3\text{Al}_2(\text{SiO}_4)_3$, spessartine $\text{Mn}^{2+}_3\text{Al}_2(\text{SiO}_4)_3$; grossular $\text{Ca}_3\text{Al}_2(\text{SiO}_4)_3$, rare uvarovite $\text{Ca}_3\text{Cr}_2(\text{SiO}_4)_3$, and andradite $\text{Ca}_3\text{Fe}_2\text{Si}_3\text{O}_{12}$ make up two solid solution series: pyrope–almandine–spessartine and uvarovite–grossular–andradite.

4.12.2 Spinel

Magnesio-iron spinel (Mg,Fe)Al₂O₄ is a common mineral in the Ca–Al-rich inclusions (CAIs) in some chondritic meteorites [293].

Chromite is iron chromium oxide, FeCr₂O₄. It is an oxide mineral belonging to the spinel structural group.¹⁵ The element magnesium can substitute for iron in variable amounts as it forms a solid solution with *magnesiochromite* MgCr₂O₄. A substitution of the element aluminum can also occur, leading to *hercynite* FeAl₂O₄.

¹⁵ Note the common usage of words like ‘spinel,’ ‘halite,’ ‘perovskite,’ ‘garnet’ not for compositionally related minerals, but for having the same structure as the name-giving mineral. For example, chromite FeCr₂O₄ has a spinel structure.

We consider the three most common endmember spinels in the substitution $(\text{Mg,Fe})(\text{Al,Cr})_2\text{O}_4$:

Magnesia-spinel ('spinel proper') MgAl_2O_4 , chromite FeCr_2O_4 , and hercynite FeAl_2O_4 .

4.12.3 Other Rare Minerals

Carlsbergite is a nitride mineral that has the chemical formula CrN , or chromium nitride. It occurs in meteorites along the grain boundaries of kamacite or troilite in the form of tiny plates. It occurs associated with kamacite, taenite, daubreelite, troilite, and sphalerite.

Schreibersite, $(\text{Fe,Ni})_3\text{P}$, is generally a rare iron–nickel phosphide mineral though common in iron–nickel meteorites. Even there it is a minor constituent, as there is only 0.50 wt% to 1.3 wt% P in iron meteorites [294]. Schreibersite and other meteoric phosphorus bearing minerals may be the ultimate source for the phosphorus on Earth.

Tridymite is a high-temperature polymorph of silica SiO_2 and usually occurs as minute tabular white or colorless pseudo-hexagonal crystals, or scales, in cavities in felsic volcanic rocks. It was found on Mars and probably is evidence for Martian silicic volcanism [295].

Hibonite, $\text{CaAl}_{12}\text{O}_{19}$ or, more generally, $(\text{Ca,Ce})(\text{Mg,Fe}^{2+})\text{Al}_{10}(\text{Ti}^{4+},\text{Al})\text{O}_{19}$ has been found in the Allende meteorite and in CAIs;

Melilite, $(\text{Ca,Na})_2(\text{Al,Mg,Fe}^{2+})(\text{Si,Al})_2\text{O}_7$ in CAIs. Both hibonite and melilite are thought to have condensed very early during the cooling of the solar nebula, so they represent some of the most primordial minerals in the solar system [223]. Hibonite is even one of the minerals in presolar grains (besides silicate minerals (olivines and pyroxenes), corundum (Al_2O_3), spinel (MgAl_2O_4), graphite (C), diamond (C), titanium oxide (TiO_2), silicon carbide (SiC), titanium carbide (TiC) and other carbides within C and SiC grains, silicon nitride (Si_3N_4) [296].

Moissanite SiC, *bridgmanite* $(\text{Mg,Fe})\text{SiO}_3$, *ringwoodite* $\gamma\text{-(Mg,Fe)}_2\text{SiO}_4$, *majorite* $\text{Mg}_3(\text{MgSi})\text{Si}_3\text{O}_{12}$, and *wadsleyite* $\beta\text{-Mg}_2\text{SiO}_4$ are high-pressure polymorphs and rare minerals found only in meteorites but thought to be significant components of the deep Earth [223].

4.13 Carbon and Carbon-Rich/Organic Matter

Significant amounts of carbonaceous materials are contained in carbonaceous chondrites, mainly as solvent unextractable macromolecular matter, analogous to terrestrial kerogen or poorly crystalline graphite. During heating, these kerogen-type carbonaceous materials lose their labile fractions, and become more and more graphitized [297]. Note that 'carbonaceous' is a bit of a misnomer since the carbon content of some *carbonaceous* chondrites does not exceed 3 to 4 % [298]; ureilite

achondrites, on the other hand, tend to have a similar fraction of carbon (~3 %) but in the form of graphite and trace amounts of nanodiamonds.

Elemental, 'native,' stable carbon, graphite, has a well-known $c_p(T)$ curve up to temperatures of ~4000 K. Imperfect graphite, like 'lamp black' with numerous stacking faults and small crystallites exhibits an excess C_p at low temperatures, significant only at <10 K. Just for the sake of completeness, we include diamond in the database; diamond has an extremely high Debye Temperature, thus a smaller C_p than most substances (except Be) over a wide range of temperatures.

For ill-defined, hydrogen-bearing, partly volatile and partly macromolecular carbonaceous material, we use two analogs: coal and ICOM ('ill-defined complex organic matter').

The specific heat capacity of coal is the highest of any mineral, being roughly 50 % higher than that of graphite in the range 300 K to 600 K. Typical 'Sub-bituminous coal' proposed as a kerogen substitute has the following composition [299]: total volatile matter 30 % to 40 %, ash 10 %, moisture a few %. c_p is referred to 'daf' composition, =dry, ash-free matter (i.e., the c_p contribution of water and ash have been removed).

In the case of coal at elevated temperatures, irreversible changes of carbonaceous material associated with the release of volatile matter: *coal* → *solid carbonaceous material* + *released volatiles* takes place. For this reason, the specific heat capacity of coal as a function of temperature is complex one; for example, our reference curve (which is the initial c_p upon heating) has a maximum at ~900 K, decreasing at higher temperatures when the volatiles have mostly been liberated; it is then not reproducible but will become closer to the c_p of graphite.

ICOM, or kerogen on Earth (a solid organic matter in sedimentary rocks), is insoluble in normal organic solvents because of the high molecular weight (upwards of 1,000 dalton) of its component compounds. It does not have a specific chemical formula. The soluble portion of kerogen is known as bitumen [297].

For most natural organic matter, at best the elemental composition (mass or at.% of C, H, O, N, S etc.) is known. Laštovka, Fulem et al. [300] have shown that $c_p(T)$ of most solid hydrocarbons (ICOM) can be well predicted from 0 K to the melting point based on a parametrization in $1/(\text{mean atomic weight}) = \alpha$, to an accuracy of ~ 6 % rms (relative deviations max. 18 %). The prediction is good for molar masses exceeding 200 g/mol and compounds with low mass fractions of hetero-atoms (O,N,S). On the high- T end, c_p predictions with values exceeding 2500 J/kg/K are not likely to be quantitative. The correlation equation has been trained with pure substances $0.10 \leq \alpha \leq 0.22$ mol/g, i.e., mean atomic weight from 4.5 to 10. The $c_p(T)$ curves of complex solid hydrocarbons look very different than those of silicates, almost linear with T , often with a slight bump at low temperatures, reminiscent of solid ammonia hydrate, water ice Ih, and polymers.

We set, a bit arbitrarily, $\alpha = 0.138$ (mean atomic mass 7.26 found in literature) and calculate $c_p(T)$ after Laštovka, Fulem et al. [300]. This will be the default $c_p(T)$ for 'organic matter' (if not dominated by elemental carbon, i.e., graphite).

There is also volatile organic matter. Some fresh carbonaceous chondrite meteorites smell of 'tar,' so there is obviously some highly volatile organic fraction in there, VOC, that is released already at room temperature in minute amounts.

However, the mass fraction of VOC seems to be irrelevant for c_p (not-macromolecular organic compounds < 1000 ppm in total [298]; ~ 100 ppm VOC in Murchison (CM-2) released from 20 °C to 300 °C [301]).

Summarizing the thermal alteration for organic matter, decomposition or pyrolysis begins to be significant at ~200 °C (coal: 250 °C). It is complete at ~1000 °C. Volatile organic matter desorbs already at room T , but in insignificant amounts for c_p (< 0.1 % by mass).

4.14 Glasses

Some minerals in their amorphous state (structural glasses) form from quenched (silicate) melts, that is, cooled very quickly, e.g., after impact events or volcanic eruptions. Lunar regolith (in most Apollo samples) contains a significant mass fraction of this type of glass. These glasses usually have a significantly lower density than their crystalline polymorphs.

Another type forms from impact shock, either as dense diaplectic glass (formed by a high-pressure solid–solid transition [302]), or also permanently densified glass, which can form by the quenching of dense mineral melts produced by high-pressure shock waves. The amorphous feldspar maskelynite (with a plagioclase composition AbAn_{70-90}) is abundant in Martian meteorites (shergottites) but it is not clear whether it is a densified glass from melt [303] or diaplectic [304].

Our terminology will only consider composition, thus for example an anorthite crystal, molten and subsequently quenched, becomes anorthite glass.

Glasses are in principle metastable, and can devitrify over geological timescales if they contain water (over time transforming to fine-grained mineral crystal fibers, observable in water-containing glasses like obsidian on the Earth's surface; no terrestrial specimens older than Cretaceous age are known). For the Moon, however, glass usually remains glass: the maximum water content of lunar volcanic glass is 100 ppm, for agglutinate glass it is effectively zero (Ryan Zeigler, pers. comm. 2019 to MZ). Thus, the lunar glasses do not really devitrify, because of the low water content. There is glass in meteorites that is 4.5 billion years old.

Glasses and other amorphous materials show typical anomalies in c_p at (very) low temperatures though it is surprising that $c_p(T)$ of a solid lacking a crystal lattice is still quite similar to that of the crystallized variant. Obviously, the peaks in c_p associated to lattice phase transitions are lacking in glasses.

Compared to the expected low-temperature Debye contribution, in glasses there are additional modes of vibration—one can be described by a two-level system (TLS), and some extra modes. In glasses, a quasilinear term in $C_p(T)$ comes from the contribution of the TLS, which results in an excess to the T^3 heat capacity $C_D(T)$ expected from the Debye theory. On top of the low-temperature quasilinear TLS term, often a so-called ‘Boson peak’ appears around 10 K with a long tail to higher temperatures (see below).

The specific heat of densified and diaplectic glasses seems to tend to the C_p of the crystalline polymorph; C_p differences between the normal and the high density glass exist, but seem to become significant only below ~90 K [305], reaching 50 % below

Fig. 15 Schematic C_p curve of a glass, T_G is the glass transition temperature, T_M the melting point. After [181]. The heat capacity of the liquid, or the glass for $T > T_G$, is always greater than the heat capacity of the solid [89]

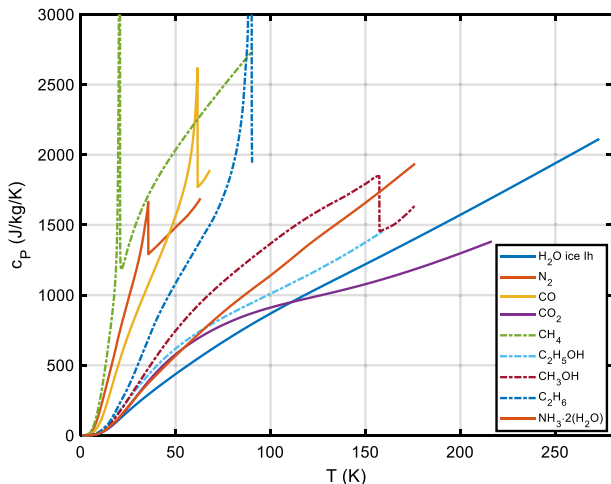
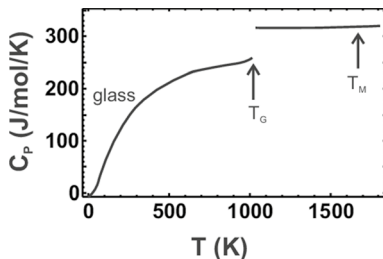


Fig. 16 Overview: $c_p(T)$ of common solar system ices. The curious dip for methanol at 157.34 K is real, it is the α/β conversion ‘from crystal II to crystal I’ just before melting

10 K, that is, the densified glass shows less of the additional heat capacity found in normal glass.

Summarizing, it is found that, in all glasses similarly,

- (1) below 1 K and 2 K: additive \sim superlinear term $\propto T^{(1+\delta)}$, $0 \leq \delta < 0.5$. At very low temperatures C_p can also depend on its cooling history and the number density of defects
- (2) ‘Boson peak’ excess C_p at around ~ 10 K extending to the order of 90 K
- (3) Suppression of lambda peaks caused by phase transitions present in the crystalline form (example Hed)
- (4) $C_p - C_V$ allowed to be different for the glassy state compared to the crystalline polymorph, since thermal expansion and compressibility change, in general
- (5) At high temperatures, the onset of the glass transition (between 900 and 1000 K, typically well below the melting temperature of the crystalline variety) produces a broad c_p peak or step (configurational heat capacity) of the order of ~ 8 J/g-atom/K, see Fig. 15. Typical curves for hydrous basaltic glasses are given in [84].

4.15 Solar System Ices

Ices relevant in the solar system (comets, icy moons, TNOs) and reviewed for our database are water ice Ih, carbon dioxide CO₂, carbon monoxide CO, methane CH₄, ethane C₂H₆, nitrogen N₂, ammonia dihydrate NH₃·2H₂O, ethanol C₂H₅OH, and methanol CH₃OH. Except CO₂ and ethanol, all have transitions in their *c_p(T)* curve. Figure 16 provides an overview; the curves end at the respective triple points.

Note that the specific heat of most ices at low temperatures (say 40 K) is much higher (factor 3 to 20) than the *c_p* of silicates at the same temperature! It is instructive to see why—There is two components: first, volatiles, having a much lower melting point than silicates, also have a much lower Debye temperature. Second, most volatiles have a lower average atomic mass *A_{av}* (3 ...14) than silicates (~22), and *c_p* scales with 1/*A_{av}*. More quantitatively, we recall the famous Lindemann formula, which can be written *T_m* ≅ *cAθ²a²* [306] with *T_m* melting temperature in K, *θ* Debye temperature (taken, e.g., at a temperature *T** when *C_v(T*)* = 1/2 *C_v(T → ∞)*), a typical interatomic distance (typically cube root of the volume per atom = (*M/ρ/N_A*)^{1/3}). Also, *c_p* ∝ 1/*A_{av}*. Thus, the ratio of the heat capacities at some low, fixed temperature *T* is approximately (*D* is the Debye function)

$$\frac{c_{p,1}}{c_{p,2}} \cong \frac{A_{av,2}D(\theta_1/T)}{A_{av,1}D(\theta_2/T)}; \quad \frac{\theta_1}{\theta_2} \cong \sqrt{\frac{T_{m,1} A_{av,2} a_2^2}{T_{m,2} A_{av,1} a_1^2}}$$

Typical volatiles have *T_m* = 150 K, *a* = 3.7 Å, and *A_{av}* = 8.5 u, while typical silicates have *T_m* = 1500 K, *a* = 4.7 Å, and *A_{av}* = 22 u. Thus, the ratio of Debye temperatures is expected to be approx. 0.65 (actually it is rather ~0.25).

At 40 K, silicates have typical Debye temperatures of 400 K; volatiles have typically 100 K. Again at 40 K, the *D* ratios is thus *D*(100/40)/*D*(400/40) ≈ 10. The ratio mean atomic mass is 22/8.5 ≈ 2.6; thus, at 40 K, volatiles typically have a *c_p* that is predicted to be ~26 times higher than that of silicates at the same temperature (actually rather 34 times!).

Note that we here compile the *c_p* of the crystalline state of cryocrystals. Many complex ices (methanol, ethanol) have a variety of polymorphs including amorphous and ‘glassy crystal’ states, with a *c_p* that is typically 1.5× to 2× higher above the glass transition temperature and ~1 % to 2% below compared to that of the thermodynamically stable crystal at the same temperature. It is not clear whether or under which conditions solar system ices exist in the glassy or crystalline state.

4.16 Tholins

Frequently, a very low thermal inertia $\Gamma(T) = \sqrt{\rho(T)k(T)c_p(T)}$ (as low as 0.1 to 3 J·m⁻²·K⁻¹·s^{-1/2}) is observed for comets and TNOs [, and references therein]. While surface material bulk densities are not so different than on other bodies, and amorphous ice with a lower thermal conductivity than crystalline ice may be present and, for granular media, the radiative part ∝ 307, 308*T*³ of thermal conductivity is smaller at low temperatures, an important effect comes from the specific heat: directly, since

Table 8 Some lab tholins [315]

References	Stoichiometry	C/N ratio	Conditions	α (mol/g)
Sagan et al. (1984)	$C_8H_{13}N_4$	1.9	Low P	0.151
Coll et al. (1995)	$C_{11}H_{11}N$	11	Low T	0.146
McKay (1996)	$C_{11}H_{11}N_2$	5.5	High T,P	0.140
Coll et al. (1999)	$C_{11}H_4N_{14}$	2.8	Low T,P	0.0873

α is the inverse of the average atomic mass

$\Gamma \propto \sqrt{c_p}$, and indirectly, since solid state thermal conductivity scales with c_p at cryogenic temperatures (that is, below the maximum in k for well-crystallized solids, e.g., [309]).

Objects beyond the ice line (comets, notably) and TNOs in particular are believed to contain a substantial fraction of frozen volatiles in their surface material. Small TNOs are thought to be low-density mixtures of rock and ice with some organic (carbon-containing) surface material such as ‘tholins,’ detected in their spectra. The composition of some small TNOs could be similar to that of comets. The optical surfaces of small bodies are subject to modification by intense radiation, solar wind, and micrometeorites. Consequently, the thin optical surface layer could be quite different from the icy regolith underneath, and not representative of the bulk composition of the body.

De Bergh et al. in [310], note that on the brightest TNOs and Centaurs (with VIS–NIR spectroscopy) several surface ices have been detected: H_2O , CH_4 , N_2 , CH_3OH , C_2H_6 , CO_2 , $NH_3 \cdot nH_2O$, and possibly HCN, in various combinations; water ice is by far the most common. Crystalline water ice, and possibly ammonia ice, have been found from spectroscopic observations of the TNO Orcus between 1.4 μm and 2.4 μm [311]. So, outer solar system body surfaces could be modeled as a mixture of ices (H_2O , CO_2 , CO , CH_4 , N_2 , ethanol, methanol, ammonia dihydrate), maybe amorphous carbon, tholins, and silicate ‘dust’ as a simple mechanical mixture.

The enigmatic tholins are believed to be created by intense radiation. Tholins are apparently found in great abundance on the surface of icy bodies in the outer solar system. Four major tholins have been proposed to fit the reddening slope [312]:

- Titan tholin, believed to be produced from a mixture of 90 % N_2 and 10 % CH_4 (gaseous methane)
- Triton tholin, as above but with very low (0.1 %) methane content
- (ethane) Ice tholin I, believed to be produced from a mixture of 86 % H_2O and 14 % C_2H_6 (ethane)
- (methanol) Ice tholin II, 80 % H_2O , 16 % CH_3OH (methanol) and 3 % CO_2

As an illustration of the two extreme TNO color classes BB and RR, the following compositions have been suggested [313]

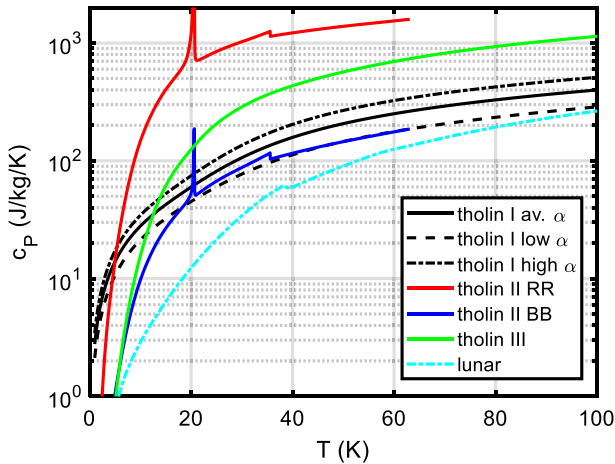


Fig. 17 Overview, specific heat of some model tholins. The range of specific heat at low temperatures is about one order of magnitude. The large λ peak at ~ 20 K is due to methane, the small anomaly near 35 K due to nitrogen. For comparison with common silicates, our lunar regolith curve is given

- for Sedna (*RR* very red): 24 % Triton tholin, 7 % carbon, 10 % N_2 , 26 % methanol, and 33 % methane
- for Orcus (*BB*, gray/blue): 85 % amorphous carbon, + 4 % Titan tholin, and 11 % H_2O ice

Tholins ('complex abiotic organic gunk' [13]) are not one specific compound but rather are descriptive of a spectrum of molecules that give a reddish, organic surface covering on certain planetary surfaces. See, e.g., [314]. The typical composition of laboratory 'Titan tholins' is 35 at.% C, 15 at.% to 30 at.% N, rest H. They are probably macromolecular and not soluble; no specific heat data are available.

McKay et al. [315] report that 'a detailed analysis of the organic compounds contained in tholin ... show that they include a complex organic mix of simple alkanes, aromatic compounds, heteropolymers, and amino acid precursors.' If that is so, tholins could be modeled like ill-defined complex organic matter based on elemental composition alone (α value) (Table 8).

4.17 Other Compounds

For hydrate and crystal water: see Sect. 2.12.1.

Calorimetric reference substances: we include some useful elements or compounds which are commonly used either as specific heat or temperature calibration materials or whose specific heat has to be known precisely for correcting C_p measurements (copper Cu, aluminum Al, vacuum grease Apiezon[®] N, etc.)

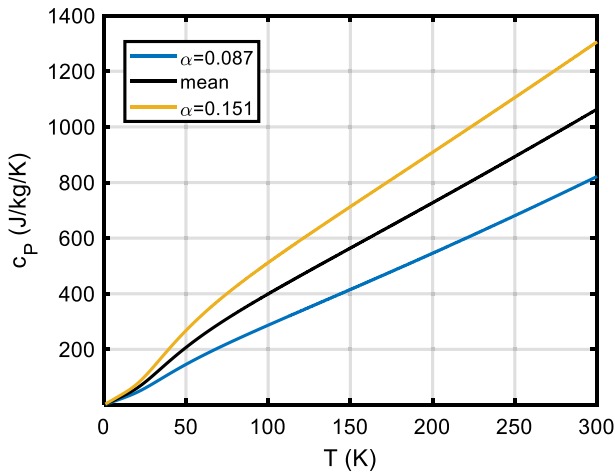


Fig. 18 The c_p of tholins, model 1. The blue and dark yellow curves indicate the likely range, the black curve is just the average of the blue and red ones

Table 9 Basic tholins, composition [312]

Ice type abbreviation	Type	Composition
T1	Titan	90 % N ₂ , 10 % CH ₄
T2	Triton	N ₂ (0.1 % CH ₄ is negligible for c_p)
T3	Ice tholin I	86 % H ₂ O ice, 14 % ethane C ₂ H ₆
T4	Ice tholin II	80 % H ₂ O ice, 16 % CH ₃ OH, 3 % CO ₂

Table 10 Composition for extreme spectral type of tholins [313]

Spectral type	Composition	Example
RR, very red	24 % T1 ice, 7 % graphite, 10 % T2 ice (N ₂), 26 % methanol, 33 % CH ₄	Sedna
BB, gray-blue	85 % graphite, 4 % T1 ice, 11 % H ₂ O ice	Orcus

5 Some Example Applications

In this chapter, we demonstrate some applications of the c_p database.

5.1 The $c_p(T)$ of Tholin Analogs

In this section, we present the calculated $c_p(T)$ curves of the tholin analogs discussed in Sect. 3.17.

Figure 17 gives an overview of the $c_p(T)$ curves of our various model tholins we will discuss hereunder. One sees that there is a large variation between models, but

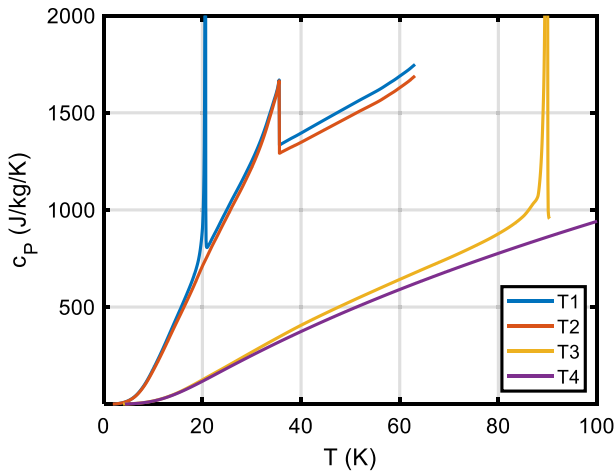


Fig. 19 The $c_p(T)$ of basic tholins, model 2

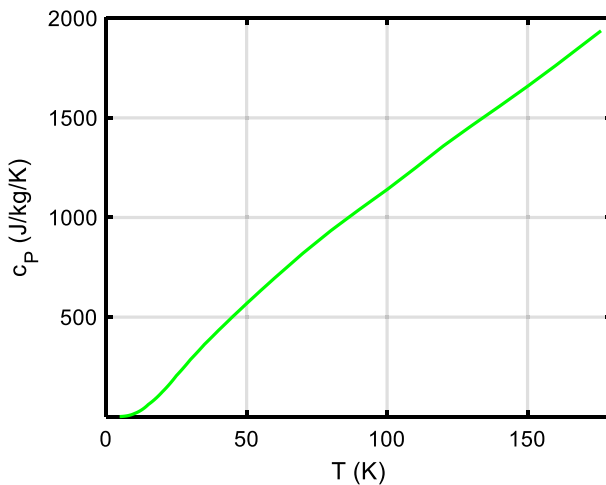


Fig. 20 Tholin model 3, specific heat of solid ammonia dihydrate, data of [316]

that a silicate (e.g., lunar regolith) $c_p(T)$ curve is certainly not appropriate, it would be about an order of magnitude too low.

5.1.1 Tholin Model 1: Ill-Defined Organic Matter

We use the model of [300] with the parameter α (inverse of average atomic mass) varying between 0.087 and 0.151 (compare Table 7 and [314]), the result is shown in Fig. 18. Calculated c_p values are much lower than for model 3 (ammonia dihydrate).

Table 11 Minerals and their mass fractions assumed for the $c_p(T)$ of DI regolith simulants

CM-1		CM-2		CI-1		CI-2		C2-1		CR-1	
Abbr	w	Abbr	w	Abbr	w	Abbr	w	Abbr	w	Abbr	w
Fa	0.57	Atg	0.7	Atg	0.365	Atg	0.48	Atg	0.305	Atg	0.09
Atg	0.22	Mag	0.1	Eps	0.15	Eps	0.06	Fo	0.225	En	0.2325
Fo	0.0729	Fo	0.0675	Mag	0.115	Mag	0.135	Fa	0.025	Fs	0.0775
Fa	0.0081	Fa	0.0075	Plg	0.09	Plg	0.05	Mag	0.22	Mag	0.14
Coal	0.035	Coal	0.035	Fo	0.063	Fo	0.063	Py	0.085	FeNi	0.05
Py	0.025	Py	0.025	Fa	0.007	Fa	0.007	Coal	0.05	Fo	0.2475
En	0.015	En	0.015	Py	0.06	Py	0.065	Vrm	0.04	Fa	0.0825
Fs	0.005	Fs	0.005	Vrm	0.05	Vrm	0.09	Plg	0.04	Py	0.04
Mag	0.01	Sms	0.035	Sd	0.04	Coal	0.05	Dol	0.01	Sms	0.02
Dol	0.01	Sd	0.01	Coal	0.035					Coal	0.02
Sms	0.029			Gp	0.025						

Some minerals appear more than once since they are part of different solid solutions. w is the mass fraction of the database mineral with abbreviation ‘abbr.’ (older nomenclature; *Atg* is antigorite, *Plg* Palygorskite = Attapulgitite, *Eps* epsomite, *Py* pyrite, *Vrm* vermiculite, *Sid* siderite, *Gy* gypsum, *Dol* dolomite, *Sms* sodium metasilicate, *Fo* forsterite, *Fa* fayalite, *Mag* magnetite, *En* enstatite, *Fs* ferrosilite, *Coal* sub-bituminous coal, and *FeNi* meteoritic iron (10 % Ni). For C2-1, antigorite has been substitute for its polymorph lizardite

5.1.2 Tholin Model 2: Mix of Ices and Graphite

The following ‘basic’ tholins are defined (Table 9).

As an illustration of the two extreme classes BB and RR, the following compositions have been suggested (Table 10) and the resulting specific heat curves are shown in Fig. 17 and for the basic tholins 1 to 4 in Fig. 19.

5.1.3 Tholin Model 3: Ammonia Dihydrate $\text{NH}_3 \cdot 2\text{H}_2\text{O}$

Sometimes ammonia dihydrate has been taken as an analog for ‘tholins.’ The specific heat for solid ammonia dihydrate is taken from [316] from near 0 K up to 176.2 K (melting temperature), Fig. 20.

5.2 The $c_p(T)$ of Various Regolith Simulants

The most obvious ‘forward’ application is of course the construction of reference $c_p(T)$ curves for a material with known or assumed mineral composition. We start by calculating the specific heat of various regoliths simulants (detailed description see Online Appendix, Sect. 5); compositions are given in Table 11.

Now applying the mixing model,

$$c_p(T) = \sum_i w_i c_p^{(i)}(T) \text{ with } w_i \text{ the mass fractions of the constituents, } \sum w_i = 1, \text{ we}$$

can immediately generate and plot the $c_p(T)$ curves, Fig. 21.

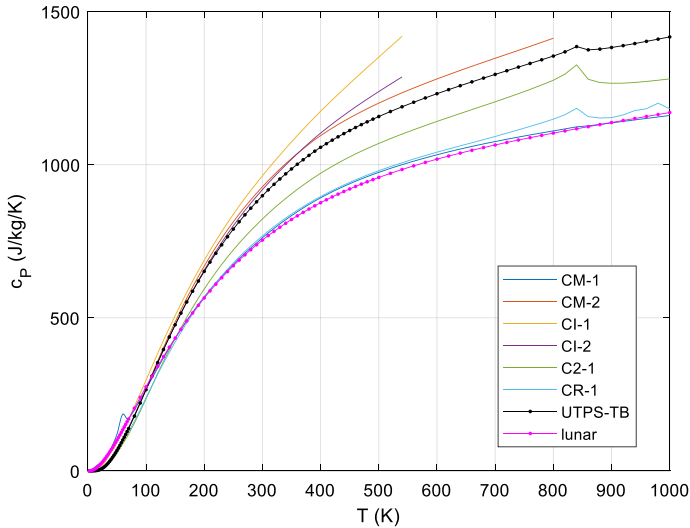


Fig. 21 Calculated $c_p(T)$ of DI regolith simulants. For comparison, the standard lunar c_p curve is given [317]. Note the ‘theoretical’ fayalite peak at ~ 60 K and the ‘theoretical’ magnetite peak at 840 K; the fayalite peak is expected to be smeared out in natural samples with the same mean fayalite content but from a range of olivine compositions. For comparison, the standard lunar c_p curve is given [317]

5.2.1 Estimating the Mineral Composition from Limited c_p Data and Extrapolating

The basic idea is the following. Given a sample where the specific heat has been measured over a limited range of temperatures, assume that we approximately know, or can guess, the mineral composition of this material, at least having an idea which minerals could be present in significant mass fractions ($> 1\%$ or so). Then we can invert the mixing equation, Eq. 10, and solve for the mass fractions w_i of the constituent minerals that produce a specific heat curve best fitting the data (Obviously, we need more data points ($T_p, c_{p,i}$) than the number of constituent minerals). Taking this composition as the best estimate of the truth, we can use Eq. 10 forward and calculate $c_p(T)$ for any temperature T in which the constituent minerals are stable, that is, perform a physically meaningful extrapolation!

We have programmed and tested this method (for lunar data) with success. Here, we present only some main points; for more details (mathematics, figures), see Online Appendix 1.2.

(In this section, to make notation more compact, C, c designate specific heat of mixture and single endmember minerals, and X stands for mass fractions).

Given the experimental c_p data of a mineral mixture over a (wide as possible) temperature range and some idea about the main constituents, i.e., a list of endmember minerals, ‘Main’ means: mass fraction X of a constituent $> X_{threshold} \approx 1\%$. We estimate the most likely mass fractions X_i of the constituent minerals by (weighted) least squares solution of the constrained mixing equation (software function `cp_decompose`) and construct the model $c_p(T)$ curve over a wider temperature range (software function `cp_compose`). So far, this is simple and fast. More difficult and lengthy is the

calculation of realistic uncertainties of the (extrapolated) model values, which we do by Monte Carlo, either adding random noise to the data or using a bootstrap method (bootstrap is preferred, since there are no assumptions about the form of the noise).

Note that the endmember mineral $c_p(T)$ curves are the base functions in our least-squares problem here; they are generally far from being orthogonal, and the problem only has a meaningful unique solution because of the constraint

$$X_i \geq 0, \quad \sum_i X_i = 1. \quad (23)$$

Generally,¹⁶ low-temperature c_p data are constraining the composition better than high-temperature ones, since the low-temperature part is more ‘diagnostic’ of a compound, thus ‘more orthogonal.’

Given M experimental data points, $T_m, C_m(T_m)$, $m = 1 \dots M$, we fit the $N < M$ mass fractions X_i using, as base functions, the $c_i(T)$ of N possible constituent minerals, since $C_m(T_m) = \sum_i X_i c_i(T_m)$ subject to the constraints (24). Let σ be the uncertainties of the C data (weighting). This is a linear least-squares problem with bounds and linear constraints; for details, see Online Appendix 1.2.

The first application of this method, for lunar surface material, is presented in the next section.

5.2.2 Construction of a Lunar c_p Reference Curve

Let us start by looking at all published (unsmoothed) Apollo c_p data (see Online Appendix). Although the 1σ uncertainty of the low-TAC Apollo specific heat data is only $\sim 0.4\%$, it is clear (compare figures in Online Appendix, Sect. 3) that the different Apollo samples have systematic differences among each other, within about $\pm 3\%$, likely due to compositional variations. This is also the range of relative differences between some previous lunar c_p fit functions in the literature. We mention the polynomials in [318] and [319], valid over the temperature range $90 \text{ K} \leq T \leq 350 \text{ K}$. Note that the Hemingway et al. [318] polynomial quickly diverges for $T > 350 \text{ K}$.

There are other correlation equations in the literature; Colozza [320] gives a crude extrapolation formula (logarithmic) of the lunar data up to melting temperatures. The expressions given by Ledlow et al. [321] are highly uncertain (possibly wrong) at high temperatures $> 350 \text{ K}$ and no improvement at low temperatures.

The work of Fujii and Osako [322] is often cited as a reference for ‘basalt.’ Actually, they measured thermal diffusivity of lunar samples and assumed the c_p of this lunar basalt as a fit to the data on lunar crystalline rock 10,057 by Robie et al. [323]. There is up to 5% deviation to the data [323] between 90 and 350 K.

A reasonable model for lunar regolith over wide temperature ranges, in particular for $T > 350 \text{ K}$ up to the assumed melting temperature, $\sim 1500 \text{ K}$, was given by

¹⁶ complications arise if there are significant solid solution composition-dependent transition peaks or other anomalies, as we have seen in the bronzite example in Sect. 2.1.1.

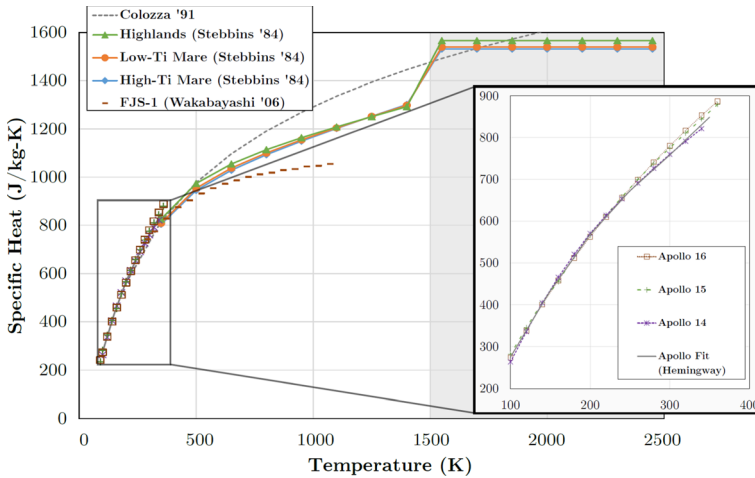


Fig. 22 The specific heat model for lunar regolith. In the lower-temperature regime (≤ 350 K), a fit from [318] based on Apollo data is used. At higher temperatures (> 350 K), a model by [325] is used. Melting temperature is 1500 K. [Reprinted from Schreiner et al. [324] with permission from Elsevier]

Schreiner et al. [324]. It is notable that separate regression models are presented for high- and low-Ti Mare and Highlands regolith to demonstrate the effect of composition—after all, most Apollo samples are basaltic (nearside) mare material, and highlands regolith (including most of the far side) is under-represented. However, as shown in Fig. 22, the difference between Mare and Highlands is $\sim 3.5\%$ at most, and that between low- and high-Ti Mare $< 1\%$.

We performed a preliminary exercise, using the Apollo data and extrapolation with pure anorthite c_p data from our database for extrapolation to low temperatures, 10 K to 80 K, and the Schreiner curve for higher temperatures (=Stebbins’ (1984) model [325] in [324], for 360 K to 1500 K). Biele et al. [317] found a convenient rational log–log fit function for this preliminary reference lunar average $c_p(T)$, Eq. 24. Besides the fact that rational functions often have better approximation properties than simple polynomials, we exploit the fact that a typical $c_p(T)$ curve looks simpler in log–log coordinates; a straight line ($\sim T^3$) at low temperatures, and no point of inflection at medium temperatures.

$$\ln\left(\frac{c_p(T)}{1 \text{ J} \cdot \text{kg}^{-1} \cdot \text{K}^{-1}}\right) = \frac{p_1 x^3 + p_2 x^2 + p_3 x + p_4}{x^2 + q_1 x + q_2} \tag{24}$$

$$x = \ln(T/1 \text{ K})$$

with just 5 fitted coefficients (p_1 is actually fixed).

$$p_1 = 3, p_2 = -54.45, p_3 = 306.8, p_4 = -376.6, q_1 = -16.81, q_2 = 87.32.$$

This rational function has no poles; it correctly predicts zero heat capacity at 0 K and a $\sim T^3$ dependence at $T < 5$ K. It fits the mean, smoothed lunar sample data [318] with an absolute maximum deviation of 3% and the high-temperature Schreiner

Table 12 Best-fit mineral composition for the Apollo c_p data, with the given list of minerals and bounds and the c_p database as of 2021

Mineral	w	$\sigma(w)$
En	0.05	0.02
Di	0.01	0.01
Hd	0.01	0.005
Fs	0.060	0.023
An	0.502	0.064
Ab	0.114	0.038
Fo	0.01	0.006
Fa	0.08	0.026
Or	0.05	0.015
Ilm	0.01	0.002
Tro	0.003	0.006
Chr	0.001	0.016
Spl	0.100	0.010

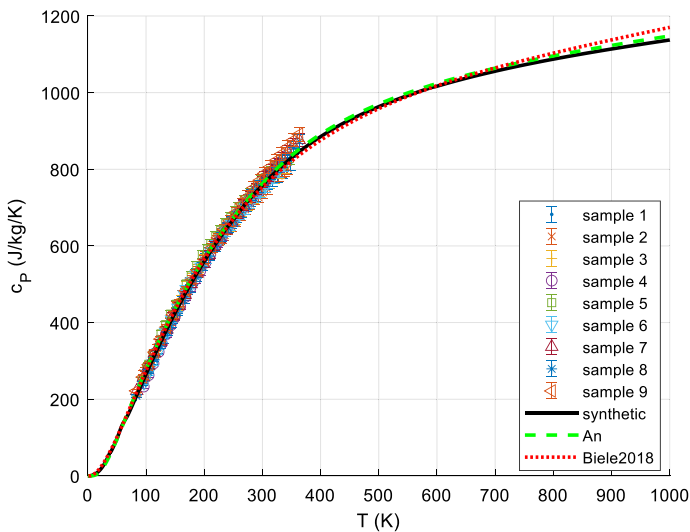


Fig. 23 Synthetic lunar c_p curve, 0 K to 1000 K, bold black line. Apollo data with error bars, separately for each of the 9 sample, are plotted with symbols as indicated in the legend; pure anorthite (An, green dashed) and analytical curve of Biele et al., 2018 [317] (red dotted line) for comparison

model to better than 1 %. The estimated uncertainty of the low-temperature portion rapidly increases below 50 K to $\sim 5\%$ to 10 %.

But now, using the results of the previous section, we are in the position to construct an even more realistic lunar c_p reference curve in a very wide temperature range. We use all the unsmoothed Apollo c_p data, assuming a constant uncertainty of 2% and decompose it into a best-fit composition, using the following list of minerals (imposed mass fraction bounds in parentheses): enstatite (5 % to 40 %),

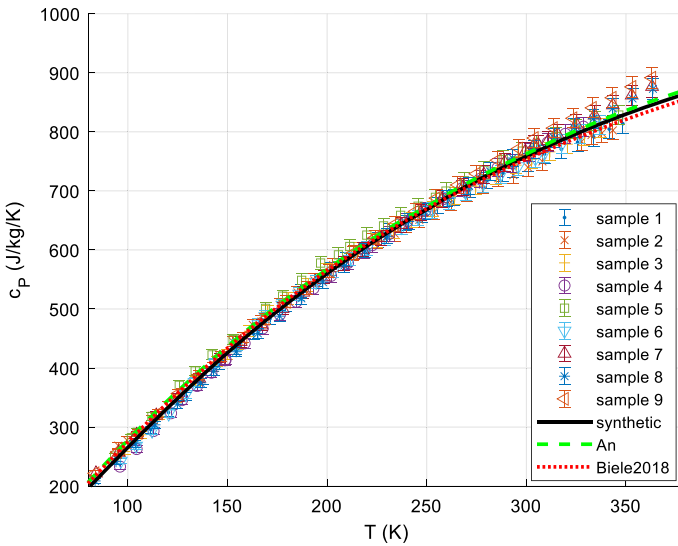


Fig. 24 Enlarged portion of Fig. 23 showing all the well-known Apollo data points (numerical values: see Online Appendix, chapter 4.1

diopside (1 % to 20 %), hedenbergite (1 % to 20 %), ferrosilite (6 % to 24 %), anorthite (12.5 % to 100 %), albite (2 % to 14 %), forsterite (1 % to 8 %), fayalite (1 % to 8 %), orthoclase (0 % to 5 %), ilmenite (1 % to 30 %), troilite (0.3 % to 2 %), chromite (0.1 % to 10 %), magnesio-spinel (0.1 % to 10 %).

The result is the following best-fit composition (Table 12):

The normalized χ^2 is 1.2, quite consistent with the estimated 2% uncertainties (intrinsic and caused by composition variations) in the data.

As expected, there is a dominating anorthite fraction, albite, spinel, olivine, some pyroxene, other feldspar, ilmenite but negligible troilite and chromite. There is a notable variation in the resulting best-fit composition depending which minerals are in the list and on their prescribed bounds, which was expected.

Now we can generate the synthetic curve (Fig. 23) and compare with the data; preliminary uncertainty estimates for the synthetic curve (using many Monte Carlo realizations in composition, calculating the $c_P(T)$ curve for each and analyzing the distribution for each temperature) showed a typical 1σ -uncertainty of $\sim 2\%$ from 90 K to 1200 K, and exponentially increasing uncertainties below 90 K (relative uncertainty 0.87 at 10 K). This will be analyzed in depth in paper II. Comparing with the preliminary model, Eq. 24, shows that the latter agrees to within 4 % for temperatures from 90 K to 1000 K, to $\pm 8\%$ for temperatures between 35 and 90 K and differing by $> 30\%$ for $T < 20$ K.

It is obvious that just the precisely known heat capacity of anorthite explains most of the data and the curve. The region 90 K to 350 K (where data exist) is enlarged in Fig. 24, and the cryogenic temperature region is shown in Fig. 25.

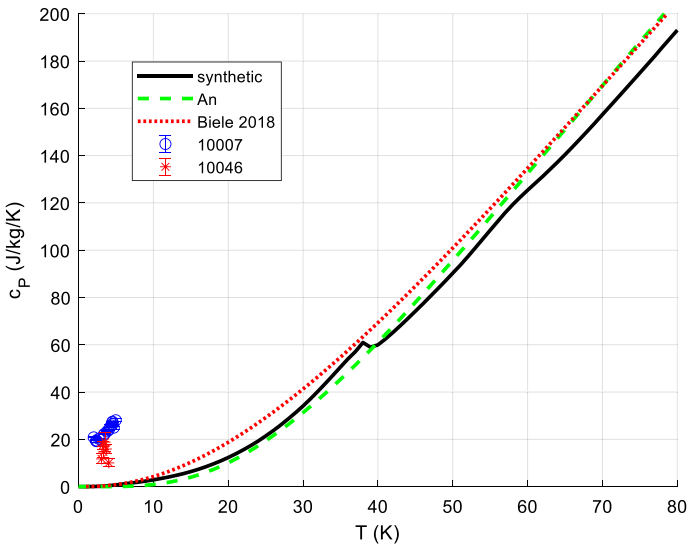


Fig. 25 Enlarged part of Fig. 23, cryogenic temperatures. Added are the specific heats of the two samples measured at LHe temperatures [326] which are ~ 2 orders of magnitude larger than expected. This cannot be explained by a glass excess c_p (factor 2–3 only), maybe it indicates a Schottky anomaly in the liquid Helium temperature range or it is due to experimental errors

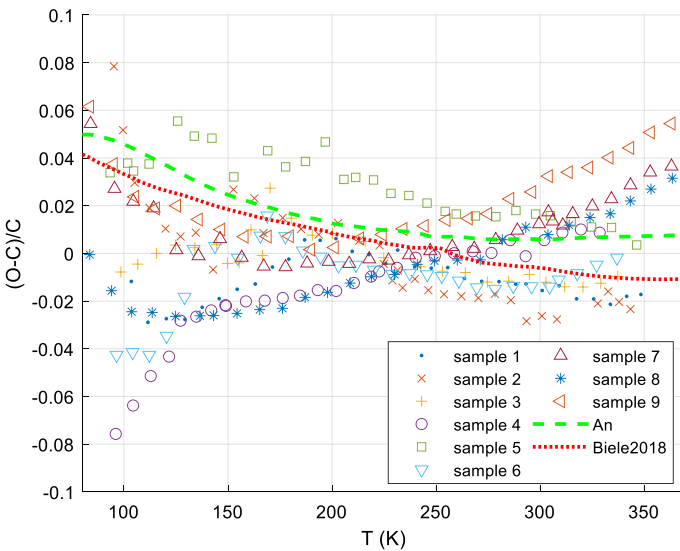


Fig. 26 Relative deviations of modeled ‘synthetic’ c_p curve to Apollo data

Finally, in Fig. 26, the relative deviations of the synthetic curve to the datasets are shown. One can clearly see the systematic differences between the 9 datasets, which we believe are mainly due to compositional differences.

5.2.3 Sensitivity of Specific Heat to Composition-Changing Processes

We can also study the effects of composition on specific heat for the most important practical cases.

Metal content It has long been known and understood that (meteorite) samples with a higher content of meteoritic iron FeNi (thus, also a higher density) have (at ~ room temperature) a smaller specific heat. This is easy to understand, since the c_p of FeNi is smaller than that of most silicates, over wide range of temperatures. We can now quantify the difference vs. temperature, for a arbitrary mass fraction w of FeNi in any mixed material X, $\Delta c_p(w) = c_p(X, \text{with } w \text{ FeNi}) - c_p(X, \text{no FeNi})$.

$$\begin{aligned} c_p &= c_{p,FeNi}w + c_{p,X}(1 - w) \\ \Delta c_p &= c_p - c_{p,X} = w(c_{p,FeNi} - c_{p,X}) \\ \frac{\Delta c_p}{c_{p,X}} &= w \left[\frac{c_{p,FeNi}}{c_{p,X}} - 1 \right] \end{aligned} \quad (25)$$

Weathering It is well known [27] that weathered, originally metal-bearing meteorites (e.g., H-chondrite finds) have a specific heat higher than analogous pristine samples (falls). Terrestrial weathering has a number of effects, the most important being the oxidation of metal to various Fe–Ni oxyhydroxides, having a much higher specific heat than the native metals. Furthermore, in moist air, metal sulfides (e.g., troilite) oxidize to hydrated sulfates, mostly $FeSO_4$, which are usually so soluble that they are transported away, leaving the oxyhydroxides. Updating Mackes weathering model [27], we assume the following: replace a percentage of the FeNi metal with 1/3 of ferrihydrite, akaganéite and goethite each, and replace half of the same percentage of troilite with goethite, the other half runs off (not a closed system). Note that the degree of hydration, i.e., the number of moles of water per mole of akagenéite, goethite, ferrihydrite, and sulfate also influences the weathering end product c_p strongly.

Ordinary chondrite meteorite c_p can be used to estimate the degree of weathering [23, 27].

In very strongly weathered specimens, silicate alteration (mainly olivines which react with water to serpentine or with ambient CO_2 to (Mg,Fe)-carbonates) or even massive replacement of silicates by clay and oxides may take place, leading to further changes in specific heat.

Carbon (organics) content Analogously, we can study the effect of carbon (graphite) or ‘organic matter’ content on $c_p(T)$. Note that ‘carbonaceous’ in meteorites is essentially a misnomer since the carbon content of carbonaceous chondrites is very low ($\leq 3.2\%$, after [327]), they just tend to look like coal. Thus, the effect is small: the ratio of $c_{p,Gr}/c_{p,lunar}$ varies from 0.3 to 1.3 in the temperature range 25 K to 500 K, while the ratio $c_{p,IOM}/c_{p,lunar}$ varies from 1.5 to 3.2; thus, analogously to Eq. 25 the maximum change in c_p to be expected is $- 2.2\%$ to $+7\%$ at 25 K, but rather $< \pm 3\%$ for temperatures > 70 K. Still, carbonaceous chondrites tend to have a higher specific heat than ordinary chondrites (next paragraph).

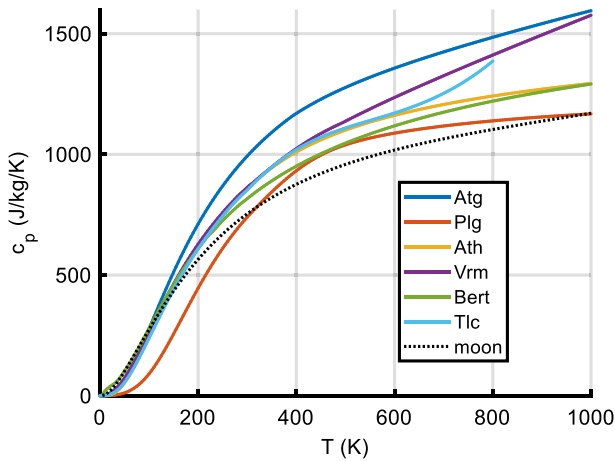


Fig. 27 Comparison of $c_p(T)$ curves for the Moon ('basaltic,' reasonable also for S-type asteroids) and for 4 different phyllosilicates or clay minerals. Talc decomposes for $T > 750$ K to 800 K, this is why the curve ends at 800 K

Phyllosilicate content More instructive is the effect of phyllosilicate content on $c_p(T)$. It turns out that (partially hydrated or dehydrated) phyllosilicates, which can be the dominant mineral species in some primitive carbonaceous chondrites, do have a significant effect on specific heat (they tend to increase c_p), compare Fig. 27. We do not agree that heat capacity of ordinary and carbonaceous chondrites is similar claimed by Consolmagno et al. [23]. The hydration state also matters; this leads directly to the last item on our list,

Thermal metamorphism Here, the idea is to estimate the variation of specific heat as a, say, primitive carbonaceous chondrite with petrologic type 1 (maximum hydrous alteration) to petrologic type 6 (maximum thermal metamorphism).

Dehydrated and thermally metamorphosed phyllosilicates are common among carbonaceous chondrites, and are probably present in the regoliths of many asteroids. For characteristic temperatures of dehydration, organic material degradation or decomposition and dehydroxylation, see e.g., Sect. 3.12 and [278, 328]. The latter work also provides in-depth analysis of the loss of water by dehydration, comparing various proposed reaction pathways for thermal alteration and providing a wealth of new experimental data (thermal gravimetric analysis TGA, differential thermal analysis DTA) on the dehydration of common serpentine group minerals; it turns out that Fe-rich serpentines decompose at > 100 K to 260 K *lower* temperatures than Mg-rich serpentines (550 °C onset, 700 °C for 5 % mass loss). We note that dehydration and dehydroxylation are very different processes. Dehydration is the removal of physisorbed or loosely bound 'crystal water' molecules. Dehydroxylation means $-OH$ groups turn into molecular water; either two neighboring $(OH)^-$ interact to produce H_2O and O_2^{2-} , or a proton H^+ and a $(OH)^-$ combine into a water molecule. To preserve electrical neutrality, complicated cation diffusion is required which really alters the minerals involved.

What can be done with the database is to find a reasonable end-state composition for a thoroughly heated, dehydrated/decomposed phyllosilicate and to calculate the c_p of these (solid) end products, in comparison to the c_p of a the completely hydrated phyllosilicate, like a CII. The water produced in the thermal alteration is of course not counted in the final petrologic type 6 composition, it is assumed to disappear.

6 Summary

In this paper (I), we summarize the theoretical and practically relevant background on the heat capacity of solids (in particular, minerals), its temperature dependence as well as useful approximations, and discuss the phase transitions and effects of pressure, crystallinity, and particle size. The concept of endmember minerals and mechanical mixtures versus solid solutions is introduced, and the possibility to know the specific heat of astro-materials fairly accurately without measuring it—if only the mineral composition can be estimated. We are always talking about the ‘complete’ $c_p(T)$ curve, from ~ 10 K to ~ 1000 K.

For the non-mineralogist, we provide background on important minerals, their polymorphs, and other relevant compounds; we discuss meteoritic iron, carbon-rich/organic matter, solar system ices, and tholins in some detail.

A table with an overview of our database is given—the c_p database itself will be subject of paper II, with a detailed description of methods and used input data (literature review), for each mineral and compound covered.

Important aspects of the specific heat like the influence of composition, (adsorbed/hydrate) water content, and thermal alteration are discussed. Put briefly, the carbon/organic matter content in e.g., carbonaceous chondrite meteorites, is insignificant for c_p variation. However, the a high FeNi (meteoritic iron) fraction significantly decreases c_p while a high content in phyllosilicates markedly increases specific heat, which can be expressed quantitatively with our c_p database.

For hydrated minerals, but even for physisorbed water in porous silicates, the addition or loss (at elevated temperatures) of water also has a significant effect on specific heat.

The accuracy of composite c_p curves is estimated to be of the order of 1 % for $T > 70$ K if the mineral composition is regarded as exact. For $10 \leq T \leq 70$ K, the uncertainty can grow to the order of 5 % (higher, but less relevant, in narrow temperature intervals near transition peaks)—in particular if there is a high proportion of solid solution minerals (other than olivine) present with high excess heat capacities (non-idealities). Anorthite (with mass fraction w_{An}) adds $w_{An} \times 9$ % to the relative uncertainty near 510 K (480 K to 520 K), due to a transition peak that is not predictable in its natural phase.

We give some quantitative example applications of the database already. First, looking at c_p at cryogenic temperatures, we note that the temperature dependence of c_p , which traditionally has often been neglected, has a significant impact on thermal inertia. We now can calculate the specific heat at any low temperature, not only for common (silicate) rocks and regolith materials, but also for solar system ices and

some tholin analogs; the latter show a very large variation in c_p between various models, but their specific heat is generally an order of magnitude higher than that of silicate rock at the same temperature.

An obvious application is the ‘forward’ prediction of c_p curves for materials with known composition, like laboratory (asteroid) regolith analogs. We have done this calculation for 6 commercial analog materials and for the Phobos simulant UTPS-TB of the University of Tokyo [329]. Result tables are in the Online Appendix of this paper.

Turning to the extra-terrestrial material which has been studied best, lunar regolith, we show how to invert the measured c_p data, which cover only the 90 K to 350 K range, and construct a physically reasonable $c_p(T)$ curve from 0 K to 1500 K. A very close predecessor of this curve was also cast into a very compact correlation equation, a rational function with only 5 fitted coefficients, which reproduces the measured and modeled values to $\sim 4\%$.

All published lunar sample c_p data have been collected, for convenience, in the Online Appendix. A brief data review on all (to date) published meteorite specific heat data is also in the Online Appendix.

7 Outlook

This paper already being exceedingly long, we decided to end here (with a kind of cliff-hanger, some might say). Part II will be the database itself, that is, the data files and auxiliary software source code (on a repository), the explanation of using the database, of the methods used for data assimilation and a description of the input and final output $c_p(T)$ for each mineral and compound covered.

This will cover one of our goals, namely to supply the community with all the ingredients to calculate their own $c_p(T)$.

Finally, in order not to delay the publication of paper II, we might publish part III of the trilogy, on further applications and further standard reference curves (e.g., [330]) and in particular on the comparison with experiments (such experiments have recently started at the laboratory of one of us, MG). The applications could, for example, include the quantitative dependence (explicit correlations) of $c_p(T)$ with composition in terms of metal, organics/phyllsilicate content, and the effects of weathering and thermal metamorphism; topics we have only touched, rather qualitatively, in the present paper. As for further specific heat reference curves, we plan to define up-to-date reference mineral compositions for the most important (\sim dozen) meteorite classes, calculate their specific heat curves and compare, if possible, to experimental data.

As of this writing, our c_p dataset includes already more than 100 endmember mineral and compound $c_p(T)$ extracted and reviewed from the literature. It is a work in progress. We know that the database may, like any compilation, contain mistakes, misinterpretations, and omissions. We hope that those who publish c_p data and/or use the database will help us to correct, improve, and extend it; do not hesitate to get in touch with us!

There is already a couple of minerals on our list where (new) specific heat data are sought, or just any because there is no data, e.g., hercynite for $T > 400$ K, NiFe alloys (of different compositions/phases) and meteoritic iron (kamacite, taenite) for 400 K to 1200 K, pentlandite $(\text{Fe,Ni})_9\text{S}_8$ for > 300 K, some phyllosilicates, tholins (laboratory-made), amorphous variants of common minerals incl. diaplectic (or otherwise densified) glass; finally, more c_p measurements on carbonaceous chondrites and iron meteorites with a well-characterized mineral composition would be very interesting, both low T and high T .

On the theoretical side, the plan is to model, if significant, excess heat capacities for feldspars and pyroxenes (simplified: only 'ideal' orthopyroxenes En–Fs and 'ideal' clinopyroxenes Di–Hed (or 'mean pigeonite' and 'mean augite,' that is, with a fixed Ca content); then there is only 1 composition variable besides the T dependence). This might need a few more experimental data. Another issue is a study of transition peaks in c_p ; in natural mineral mixtures with a spatial distribution of solid solution compositions, it is conceivable that narrow transition peaks are 'smeared out'; how to handle this in c_p models needs to be studied.

Finally, and this is relevant for the sample analysis community, we recommend to measure $c_p(T)$ of new samples returned from missions to asteroids (Ryugu, Bennu come to mind), new samples from the Moon (highland rocks, in particular) and other solar system bodies over wide temperature ranges. Nowadays, just 10 mg to 30 mg of a sample¹⁷ suffices to determine the specific heat capacity accurately over the temperature range 2 K to 900 K by PPMS and power-compensated DSC calorimetry. In particular, samples from primitive asteroids that contain a significant amount of phyllosilicates would be very interesting to compare to the models presented here.

Supplementary Information The online version contains supplementary material available at <https://doi.org/10.1007/s10765-022-03046-5>.

Acknowledgments Grant P33904 to E. Dachs by the Austrian Science Fund (FWF) is gratefully acknowledged. M. Zolensky acknowledges a grant by the NASA-Hayabusa 2 Participating Scientist Program. We are grateful for discussions and share of data with Robert J. Macke (Vatican observatory), Dan Britt (University of Central Florida, Orlando), and Cyril P. Opeil (Boston College). We would also like to thank the Engauge team for providing an excellent free digitizer software [331] which made data import from published graphs easy and accurate.

Author Contributions JB and MG had the idea for the article. AB and ED contributed their expertise in minerals, experimental measurement and theory of heat capacity; MZ contributed his vast knowledge about meteoritic minerals; AB helped with artwork and many clarifications; JB performed the literature search, data analysis, and drafted the work; all authors critically revised it.

Funding Open Access funding enabled and organized by Projekt DEAL.

¹⁷ Are such measurements non-destructive besides homogenization and possibly grinding? Potentially yes, if the sample is heated beyond decomposition temperature (~ 200 °C to 300 °C).

Declarations

Conflict of interest The authors have no financial or proprietary interests in any material discussed in this article.

Open Access This article is licensed under a Creative Commons Attribution 4.0 International License, which permits use, sharing, adaptation, distribution and reproduction in any medium or format, as long as you give appropriate credit to the original author(s) and the source, provide a link to the Creative Commons licence, and indicate if changes were made. The images or other third party material in this article are included in the article's Creative Commons licence, unless indicated otherwise in a credit line to the material. If material is not included in the article's Creative Commons licence and your intended use is not permitted by statutory regulation or exceeds the permitted use, you will need to obtain permission directly from the copyright holder. To view a copy of this licence, visit <http://creativecommons.org/licenses/by/4.0/>.

References

1. B. Gundlach, J. Blum, A new method to determine the grain size of planetary regolith. *Icarus* **223**, 479–492 (2013)
2. N. Sakatani et al., Thermal conductivity model for powdered materials under vacuum based on experimental studies. *AIP Adv.* **7**, 015310 (2017). <https://doi.org/10.1063/1.4975153>
3. N. Sakatani et al., Thermal conductivity of lunar regolith simulant JSC-1A under vacuum. *Icarus* **309**, 13–24 (2018)
4. K. Wada et al., Asteroid Ryugu before the Hayabusa2 encounter. *Prog. Earth Planet. Sci.* **5**, 82 (2018). <https://doi.org/10.1186/s40645-018-0237-y>
5. A.J. Ryan et al., Full-field modeling of heat transfer in asteroid regolith: radiative thermal conductivity of polydisperse particulates. *J. Geophys. Res. Planets* **125**, e2019JE006100 (2020). <https://doi.org/10.1029/2019je006100>
6. K. Ogawa et al., Possibility of estimating particle size and porosity on Ryugu through MARA temperature measurements. *Icarus* **333**, 318 (2019)
7. D.P. Rubincam, Asteroid orbit evolution due to thermal drag. *J. Geophys. Res. Planets* **100**(E1), 1585–1594 (1995)
8. S.R. Chesley et al., Direct detection of the Yarkovsky effect by radar ranging to asteroid 6489 Golevka. *Science* **302**(5651), 1739–1742 (2003)
9. W.F. Botke Jr. et al., The Yarkovsky and YORP effects: implications for asteroid dynamics. *Annu. Rev. Earth Planet. Sci.* **34**, 157–191 (2006)
10. S.J. Paddack, Rotational bursting of small celestial bodies: effects of radiation pressure. *J. Geophys. Res.* **74**, 4379–4381 (1969)
11. K.R. Housen, W.J. Sweet, K.A. Holsapple, Impacts into porous asteroids. *Icarus* **300**, 72–96 (2018). <https://doi.org/10.1016/j.icarus.2017.08.019>
12. M. Jutzi, P. Michel, Collisional heating and compaction of small bodies: constraints for their origin and evolution. *Icarus* **350**, 113867 (2020). <https://doi.org/10.1016/j.icarus.2020.113867>
13. C. Sagan, B. Khare, Tholins: organic chemistry of interstellar grains and gas. *Nature* **277**(5692), 102–107 (1979)
14. S. Piqueux et al., Specific heat capacity measurements of selected meteorites for planetary surface temperature modeling. *J. Geophys. Res. Planets* **126**, e2021JE007003 (2021)
15. A. Martinez, M. Siegler, A global thermal conductivity model for lunar regolith at low temperatures. *J. Geophys. Res. Planets* **126**, e2021JE006829 (2021)
16. C.A. Geiger, E. Dachs, Recent developments and the future of low-T calorimetric investigations in the Earth sciences: consequences for thermodynamic calculations and databases. *J. Metamorph. Geol.* **36**, 283–295 (2018)
17. E. MacLennan, A. Toliou, M. Granvik, Dynamical evolution and thermal history of asteroids (3200) Phaethon and (155140) 2005 UD. *Icarus* **366**, 114535 (2021)
18. D.A. Paige et al., Diviner lunar radiometer observations of cold traps in the Moon's south polar region. *Science* **330**(6003), 479–482 (2010)

19. E. Sefton-Nash et al., Evidence for ultra-cold traps and surface water ice in the lunar south polar crater Amundsen. *Icarus* **332**, 1–13 (2019). <https://doi.org/10.1016/j.icarus.2019.06.002>
20. S. Henke et al., Thermal evolution and sintering of chondritic planetesimals. *Astron. Astrophys.* **537**, A45 (2012)
21. T. Baba, A. Ono, Improvement of the laser flash method to reduce uncertainty in thermal diffusivity measurements. *Meas. Sci. Technol.* **12**, 2046 (2001)
22. C.P. Opeil et al., Stony meteorite thermal properties and their relationship to meteorite chemical and physical states. *Meteorit. Planet. Sci.* (2012). <https://doi.org/10.1111/j.1945-5100.2012.01331.x>
23. G.J. Consolmagno et al., The measurement of meteorite heat capacity at low temperatures using liquid nitrogen vaporization. *Planet. Space Sci.* **87**, 146–156 (2013)
24. G. Consolmagno, R. Macke, D. Britt, Meteorite heat capacities: results to date, in *Asteroids, Comets, Meteors 2014 Proceedings of the Conference*, 30 June–4 July 2014 in Helsinki, Finland (2014)
25. R. Macke, G. Consolmagno, D. Britt, Heat capacity measurements of HED meteorites from the Vatican collection, in *Lunar and Planetary Science Conference* (2014).
26. R. Macke et al., Ordinary chondrite heat capacities below 350 K, in *Lunar and Planetary Science Conference* (2016)
27. R. Macke., C. Opeil, G. Consolmagno, Quantifying weathering in ordinary chondrite finds using heat capacity, in *Lunar and Planetary Science Conference* (2017)
28. M. Bonidie et al., *Physical and Thermal Properties of Iron Meteorites Below 300 K* (Bulletin of the American Physical Society, New York, 2019)
29. R.J. Macke et al., Heat capacities of ordinary chondrite falls below 300 K. *Meteorit. Planet. Sci.* **54**, 2729–2743 (2019)
30. C. Opeil et al., The surprising thermal properties of CM carbonaceous chondrites. *Meteorit. Planet. Sci.* (2020). <https://doi.org/10.1111/maps.13556>
31. P. Morgan et al., A pre-landing assessment of regolith properties at the InSight landing site. *Space Sci. Rev.* **214**, 104 (2018)
32. D.S. Lauretta et al., OSIRIS-REx at Bennu: Overcoming challenges to collect a sample of the early Solar System, in *Sample Return Missions* (Elsevier, Amsterdam, 2021), pp. 163–194
33. R. Reisener, J. Goldstein, M. Petaev, Olivine zoning and retrograde olivine-orthopyroxene-metal equilibration in H5 and H6 chondrites. *Meteorit. Planet. Sci.* **41**, 1839–1852 (2006)
34. L.M. Keller et al., Asymmetrically zoned reaction rims: assessment of grain boundary diffusivities and growth rates related to natural diffusion-controlled mineral reactions. *J. Metamorph. Geol.* **26**, 99–120 (2008). <https://doi.org/10.1111/j.1525-1314.2007.00747.x>
35. J. Biele et al., Effects of dust layers on thermal emission from airless bodies. *Prog. Earth Planet Sci.* **6**, 48 (2019). <https://doi.org/10.1186/s40645-019-0291-0>
36. K. Yomogida, T. Matsui, Physical properties of ordinary chondrites. *J. Geophys. Res. Solid Earth* **88**(B11), 9513–9533 (1983)
37. B.-X. Wang, L.-P. Zhou, X.-F. Peng, Surface and size effects on the specific heat capacity of nanoparticles. *Int. J. Thermophys.* **27**, 139–151 (2006)
38. A. Cezairliyan, C.Y. Ho, eds., *Specific Heat of Solids*, vols. 1–2. CINDAS Data Series on Material Properties, ed. by A. Cezairliyan, C.Y. Ho (Hemisphere Publishing, New York, 1988)
39. R.G. Berman, Internally-consistent thermodynamic data for minerals in the system Na₂O–K₂O–CaO–MgO–FeO–Fe₂O₃–Al₂O₃–SiO₂–TiO₂–H₂O–CO₂. *J. Petrol.* **29**, 445–522 (1988)
40. T. Holland, R. Powell, An improved and extended internally consistent thermodynamic dataset for phases of petrological interest, involving a new equation of state for solids. *J. Metamorph. Geol.* **29**, 333–383 (2011)
41. O. Fabricnaya et al., *Thermodynamic Data, Models, and Phase Diagrams in Multicomponent Oxide Systems: An Assessment for Materials and Planetary Scientists Based on Calorimetric, Volumetric and Phase Equilibrium Data*. CODATA: Data and Knowledge in a Changing World (Springer, Berlin, 2004)
42. R.A. Robie, *Thermodynamic Properties of Minerals and Related Substances at 298.15 K and 1 bar (10⁵ Pascals) Pressure and at Higher Temperatures* (US Geological Survey Bulletin, Washington, 1978), p. 1452.
43. R.A. Robie, B.S. Hemingway, *Thermodynamic Properties of Minerals and Related Substances at 298.15 K and 1 bar (10⁵ Pascals) Pressure and at Higher Temperatures*, vol. 2131 (US Geological Survey Bulletin, Washington, 1995), p. 461

44. N.D. Chatterjee et al., The Bayesian approach to an internally consistent thermodynamic database: theory, database, and generation of phase diagrams. *Contrib. Miner. Petrol.* **133**(1–2), 149–168 (1998)
45. R.G. Berman, T.H. Brown, Heat capacity of minerals in the system $\text{Na}_2\text{O}-\text{K}_2\text{O}-\text{CaO}-\text{MgO}-\text{FeO}-\text{Fe}_2\text{O}_3-\text{Al}_2\text{O}_3-\text{SiO}_2-\text{TiO}_2-\text{H}_2\text{O}-\text{CO}_2$: representation, estimation, and high temperature extrapolation. *Contrib. Miner. Petrol.* **89**, 168–183 (1985). <https://doi.org/10.1007/bf00379451>
46. I. Barin, G. Platzki, *Thermochemical Data of Pure Substances*, 3rd edn. (VCH, Weinheim, 1995)
47. M. Gottschalk, *Internally Consistent Thermodynamic Data for Rock Forming Minerals in the System $\text{SiO}_2-\text{TiO}_2-\text{Al}_2\text{O}_3-\text{Fe}_2\text{O}_3-\text{CaO}-\text{MgO}-\text{FeO}-\text{K}_2\text{O}-\text{Na}_2\text{O}-\text{H}_2\text{O}-\text{CO}_2$: Complete Set of Figures with References* (Geoforschungszentrum, Potsdam, 1997)
48. S. Bigdeli, Q. Chen, M. Selleby, A new description of pure C in developing the third generation of calphad databases. *J. Phase Equilib. Diffus.* **39**, 832–840 (2018)
49. N. Mounet, N. Marzari, First-principles determination of the structural, vibrational and thermodynamic properties of diamond, graphite, and derivatives. *Phys. Rev. B* **71**, 205214 (2005). <https://doi.org/10.1103/PhysRevB.71.205214>
50. A. Dick et al., Ab initio based determination of thermodynamic properties of cementite including vibronic, magnetic, and electronic excitations. *Phys. Rev. B* **84**, 125101 (2011)
51. A. Benisek, E. Dachs, The accuracy of standard enthalpies and entropies for phases of petrological interest derived from density-functional calculations. *Contrib. Miner. Petrol.* **173**, 1–11 (2018)
52. R.M. Wentzcovitch, Y.G. Yu, Z. Wu, Thermodynamic properties and phase relations in mantle minerals investigated by first principles quasiharmonic theory. *Rev. Mineral. Geochem.* **71**, 59–98 (2010)
53. A. Cezaairliyan, A.C. Anderson et al., Specific heat of solids, in *CINDAS DATA Series on Material Properties*. ed. by Y.S. Touloukian, C.Y. Ho (Hemisphere Publishing Corporation, New York, 1988), p. 484
54. P. Debye, Zur Theorie der spezifischen Wärmen. *Ann. Phys.* **344**, 789–839 (1912). <https://doi.org/10.1002/andp.19123441404>
55. G.D. Price, N.L. Ross, *The Stability of Minerals*, vol. 3 (Springer, Dordrecht, 1992)
56. G. Mavko, T. Mukerji, J. Dvorkin, *The Rock Physics Handbook: Tools for Seismic Analysis of Porous Media* (Cambridge University Press, Cambridge, 2009)
57. R. Pässler, Efficient Debye function interpolation formulae: sample applications to diamond. *Rec. Prog. Mater.* (2021). <https://doi.org/10.21926/rpm.2104042>
58. A. Einstein, Die Plancksche Theorie der Strahlung und die Theorie der spezifischen Wärme. *Ann. Phys.* **327**, 180–190 (1907). <https://doi.org/10.1002/andp.19063270110>
59. R. Mulford, D. Swift, S. Hamel, Equation of state of ammonia. *J. Phys. Conf. Ser.* **500**, 072001 (2014)
60. B. Wunderlich, *Thermal Analysis of Polymeric Materials* (Springer, Berlin, 2005)
61. S.W. Kieffer, Thermodynamics and lattice vibrations of minerals: 2. Vibrational characteristics of silicates. *Rev. Geophys.* **17**, 20–34 (1979)
62. S.W. Kieffer, Thermodynamics and lattice vibrations of minerals: 3. Lattice dynamics and an approximation for minerals with application to simple substances and framework silicates. *Rev. Geophys.* **17**, 35–59 (1979)
63. S.W. Kieffer, Thermodynamics and lattice vibrations of minerals: 4. Application to chain and sheet silicates and orthosilicates. *Rev. Geophys.* **18**, 862–886 (1980)
64. M.H. Jacobs, R. Schmid-Fetzer, A.P. van den Berg, An alternative use of Kieffer's lattice dynamics model using vibrational density of states for constructing thermodynamic databases. *Phys. Chem. Miner.* **40**, 207–227 (2013)
65. M.H. Jacobs, B.H. de Jong, Quantum-thermodynamic treatment of intrinsic anharmonicity; Wallace's theorem revisited. *Phys. Chem. Miner.* **32**(8–9), 614–626 (2005)
66. E.F. Westrum Jr., N. Komada, Progress in modeling heat capacity versus temperature morphology. *Thermochim. Acta* **109**, 11–28 (1986). [https://doi.org/10.1016/0040-6031\(86\)85004-3](https://doi.org/10.1016/0040-6031(86)85004-3)
67. N. Komada, E.F. Westrum Jr., Modeling lattice heat-capacity contributions by a single-parametric phonon dispersion approach. *J. Chem. Thermodyn.* **29**, 311–336 (1997)
68. C. Bertoldi, E. Dachs, P. Appel, Heat-pulse calorimetry measurements on natural chlorite-group minerals. *Am. Miner.* **92**, 553–559 (2007). <https://doi.org/10.2138/am.2007.2247>
69. A. Chopelas, Thermal properties of forsterite at mantle pressures derived from vibrational spectroscopy. *Phys. Chem. Miner.* **17**, 149–156 (1990). <https://doi.org/10.1007/bf00199666>
70. J. Ganguly, *Thermodynamics in Earth and Planetary Sciences*, 2nd edn. (Springer, Cham, 2020)

71. M. Tirone, On the use of thermal equations of state and the extrapolation at high temperature and pressure for geophysical and petrological applications. *Geophys. J. Int.* **202**, 1483–1494 (2015)
72. O. Anderson, I. Suzuki, Anharmonicity of three minerals at high temperature: forsterite, fayalite, and periclase. *J. Geophys. Res. Solid Earth* **88**(B4), 3549–3556 (1983)
73. J. Leitner et al., Application of Neumann–Kopp rule for the estimation of heat capacity of mixed oxides. *Thermochim. Acta* **497**, 7–13 (2010). <https://doi.org/10.1016/j.tca.2009.08.002>
74. P. Gillet, F. Guyot, J.-M. Malezieux, High-pressure, high-temperature Raman spectroscopy of Ca_2GeO_4 (olivine form): some insights on anharmonicity. *Phys. Earth Planet. Interiors* **58**(2–3), 141–154 (1989)
75. P. Gillet et al., High-temperature thermodynamic properties of forsterite. *J. Geophys. Res. Solid Earth* **96**(B7), 11805–11816 (1991). <https://doi.org/10.1029/91JB00680>
76. S.K. Saxena, *Thermodynamic Data: Systematics and Estimation*, vol. 10 (Springer, New York, 1992)
77. G.A. Berezovskii, V.A. Drebushchak, T.A. Kravchenko, Low-temperature heat capacity of pentlandite. *Am. Miner.* **86**, 1312–1313 (2001)
78. N.E. Phillips, Low-temperature heat capacity of metals. *Crit. Rev. Solid State Mater. Sci.* **2**, 467–553 (1971)
79. T. Nihira, T. Iwata, Temperature dependence of lattice vibrations and analysis of the specific heat of graphite. *Phys. Rev. B* **68**, 134305 (2003)
80. M. De Souza et al., Specific heat anomalies in solids described by a multilevel model. *Braz. J. Phys.* **46**, 206–212 (2016)
81. J. Lee, Analytic model of the Schottky anomaly and phase transition. *J. Korean Phys. Soc.* **67**, 1133–1136 (2015)
82. M. Aronson et al., Magnetic excitations and heat capacity of fayalite, Fe_2SiO_4 . *Am. Miner.* **92**, 481–490 (2007)
83. J.M. Schliesser, B.F. Woodfield, Lattice vacancies responsible for the linear dependence of the low-temperature heat capacity of insulating materials. *Phys. Rev. B* **91**, 024109 (2015)
84. G. Robert et al., Heat capacity of hydrous basaltic glasses and liquids. *J. Non-Cryst. Solids* **390**, 19–30 (2014). <https://doi.org/10.1016/j.jnoncrysol.2014.02.011>
85. J.L. McClure, A. Cezairliyan, Measurement of the heat of fusion of tungsten by a microsecond-resolution transient technique. *Int. J. Thermophys.* **14**, 449–455 (1993). <https://doi.org/10.1007/bf00566044>
86. A. Steppke et al., Nuclear contribution to the specific heat of $\text{Yb}(\text{Rh}_{0.93}\text{Co}_{0.07})_2\text{Si}_2$. *Phys. Status Solidi B* **247**, 737–739 (2010)
87. E.S.R. Gopal, *Specific Heats at Low Temperatures* (Plenum Press, New York, 1966)
88. A. Tari, *The Specific Heat of Matter at Low Temperatures* (World Scientific, Singapore, 2003)
89. C.A. Geiger, *Solid Solutions in Silicate and Oxide systems*, vol. 3 (The Mineralogical Society of Great Britain and Ireland, London, 2001)
90. A. Benisek, E. Dachs, H. Kroll, Excess heat capacity and entropy of mixing in ternary series of high-structural-state feldspars. *Eur. J. Mineral.* **22**, 403–410 (2010)
91. K.M. Krupka et al., High-temperature heat capacities and derived thermodynamic properties of anthophyllite, diopside, dolomite, enstatite, bronzite, talc, tremolite and wollastonite. *Am. Miner.* **70**(3–4), 261–271 (1985)
92. K.M. Krupka et al., Low-temperature heat capacities and derived thermodynamic properties of anthophyllite, diopside, enstatite, bronzite, and wollastonite. *Am. Miner.* **70**(3–4), 249–260 (1985)
93. A. Benisek, E. Dachs, H. Kroll, Excess heat capacity and entropy of mixing in the high-structural state (K, Ca)-feldspar binary. *Phys. Chem. Miner.* **37**, 209–218 (2010)
94. A. Benisek, E. Dachs, H. Kroll, A ternary feldspar-mixing model based on calorimetric data: development and application. *Contrib. Miner. Petrol.* **160**, 327–337 (2010)
95. E. Dachs et al., A low-temperature calorimetric study of synthetic (forsterite + fayalite) ($\text{Mg}_2\text{SiO}_4 + \text{Fe}_2\text{SiO}_4$) solid solutions: an analysis of vibrational, magnetic, and electronic contributions to the molar heat capacity and entropy of mixing. *J. Chem. Thermodyn.* **39**, 906–933 (2007). <https://doi.org/10.1016/j.jct.2006.11.009>
96. H. Haselton et al., Calorimetric investigation of the excess entropy of mixing in analbite-sanidine solid solutions: lack of evidence for Na, K short-range order and implications for two-feldspar thermometry. *Am. Mineral.* **68**(3–4), 398 (1983)
97. A. Benisek, E. Dachs, H. Kroll, Excess heat capacity and entropy of mixing in high structural state plagioclase. *Am. Miner.* **94**(8–9), 1153–1161 (2009)

98. K. Etzel et al., Thermodynamic mixing behavior of synthetic Ca–Tschermak–diopside pyroxene solid solutions: I Volume and heat capacity of mixing. *Phys. Chem. Miner.* **34**, 733–746 (2007). <https://doi.org/10.1007/s00269-007-0191-5>
99. E. Robertson, B. Hemingway, *Heat Capacity and Heat Content of Rocks*, Open-File Report (US Geological Survey Bulletin, Washington, 1995), pp. 95–622
100. H.W. Fairbairn, *A Cooperative Investigation of Precision and Accuracy in Chemical, Spectrochemical and Modal Analysis of Silicate Rocks*, vol. 980 (US Government Printing Office, Washington, 1951)
101. R.E. Stevens, R.E. Stevens, *Second Report on a Cooperative Investigation of the Composition of Two Silicate Rocks* (US Government Printing Office, Washington, 1960)
102. G.M. Friedman, Chemical analyses of rocks with the petrographic microscope. *Am. Mineral. J. Earth Planet. Mater.* **45**(1–2), 69–78 (1960)
103. J. Huebner, A. Duba, L. Wiggins, Electrical conductivity of pyroxene which contains trivalent cations: laboratory measurements and the lunar temperature profile. *J. Geophys. Res. Solid Earth* **84**(B9), 4652–4656 (1979). <https://doi.org/10.1029/JB084iB09p04652>
104. L. Shapiro, *Rapid Analysis of Silicate, Carbonate and Phosphate Rocks—Revised Edition*, U.S. Geological Survey Bulletin (US Government Printing Office, Washington, 1975)
105. P.-S. Ross, B. Giroux, B. Latutrie, Precision and accuracy of modal analysis methods for clastic deposits and rocks: a statistical and numerical modeling approach. *Geosphere* **17**, 987–1006 (2021)
106. A.B. Thompson, E.H. Perkins, Lambda transitions in minerals, in *Thermodynamics of Minerals and Melts*, ed. by R.C. Newton, A. Navrotsky, B.J. Wood (Springer, New York, 1981), pp. 35–62
107. R.A. Yund, J. Tullis, The effect of water, pressure, and strain on Al/Si order-disorder kinetics in feldspar. *Contrib. Miner. Petrol.* **72**, 297–302 (1980)
108. R. Yund, T. Anderson, Oxygen isotope exchange between potassium feldspar and KCl solution, in *Geochemical Transport and Kinetics* (Carnegie Institution of Washington, Washington, DC, 1974), pp. 99–105
109. R. Christoffersen, R.A. Yund, J. Tullis, Inter-diffusion of K and Na in alkali feldspars; diffusion couple experiments. *Am. Miner.* **68**(11–12), 1126–1133 (1983)
110. J.B. Brady, R.A. Yund, Interdiffusion of K and Na in alkali feldspars; homogenization experiments. *Am. Miner.* **68**(1–2), 106–111 (1983)
111. T. Ashida, S. Kume, E. Ito, Thermodynamic aspects of phase boundary among α -, β -, and γ - Mg_2SiO_4 . *High-Press. Res. Mineral Phys. Vol. Honor Syun-iti Akimoto* **39**, 269–274 (1987)
112. R.J. Harrison, Magnetic transitions in minerals. *Rev. Mineral. Geochem.* **39**, 175–202 (2000)
113. J. Coey, S. Ghose, Magnetic phase transitions in silicate minerals, in *Structural and Magnetic Phase Transitions in Minerals* (Springer, Berlin, 1988), pp. 162–184
114. S.L. Chaplot, R. Mittal, N. Choudhury, *Thermodynamic Properties of Solids: Experiment and Modeling* (Wiley, Weinheim, 2010)
115. S. Takai et al., Low-temperature heat capacities and Verwey transition of magnetite. *J. Chem. Thermodyn.* **26**, 1259–1266 (1994). <https://doi.org/10.1006/jcht.1994.1143>
116. F. Walz, The Verwey transition—a topical review. *J. Phys. Condens. Matter* **14**, R285 (2002)
117. J. García, G. Subías, The Verwey transition—a new perspective. *J. Phys. Condens. Matter* **16**, R145 (2004)
118. G. Jaeger, The Ehrenfest classification of phase transitions: introduction and evolution. *Arch. Hist. Exact Sci.* **53**, 51–81 (1998). <https://doi.org/10.1007/s004070050021>
119. P. Ehrenfest, *Phasenumwandlungen im üblichen und erweiterten Sinn, klassifiziert nach den entsprechenden Singularitäten des thermodynamischen Potentials*. Verhandlungen der Koninklijke Akademie van Wetenschappen. Communications from the Physical Laboratory of the University of Leiden. Vol. 36; Supplement No 75b (NV Noord-Hollandsche Uitgevers Maatschappij, Amsterdam, 1933)
120. A.B. Pippard, *Elements of Classical Thermodynamics* (Cambridge University Press, Cambridge, 1957)
121. G. Fischer, On phase transformations. *Am. J. Phys.* **25**, 100–108 (1957)
122. M.E. Fisher, The theory of equilibrium critical phenomena. *Rep. Prog. Phys.* **30**, 615 (1967)
123. M.E. Fisher, The theory of equilibrium critical phenomena. *Rep. Prog. Phys.* **31**, 418–418 (1968). <https://doi.org/10.1088/0034-4885/31/1/508>
124. M.E. Fisher, Phases and phase diagrams: Gibbs’s legacy today, in *The Proceeding of the Gibbs Symposium (Yale University)* (American Mathematical Society, Providence, 1990)
125. A. Münster, *Classical Thermodynamics* (Wiley Incorporated, New York, 1970)

126. E.K. Riedel, Theory of tricritical phase transitions. AIP Conf. Proc. **10**, 865–869 (1973). <https://doi.org/10.1063/1.2947038>
127. S. Kieffer, A. Navrotsky, *Microscopic to Macroscopic: Atomic Environments to Mineral Thermodynamics*, vol. 14 (Walter de Gruyter GmbH & Co KG, Berlin, 1985)
128. Y. Mnyukh, On the phase transitions that cannot materialize. Am. J. Condens. Matter Phys. **4**, 1–12 (2014). <https://doi.org/10.5923/j.ajemp.20140401.01>
129. Y. Mnyukh, Searching for a critical phenomenon. Am. J. Condens. Matter Phys. **10**, 1–13 (2020)
130. K.R. Hosieni, R.A. Howald, M.W. Scanlon, Thermodynamics of the lambda transition and the equation of state of quartz. Am. Miner. **70**(7–8), 782–793 (1985)
131. E.K. Salje, *Physical Properties and Thermodynamic Behaviour of Minerals*, vol. 225 (Springer, Dordrecht, 1988)
132. E. Dachs, C.A. Geiger, Heat-capacity behaviour of hemimorphite, $Zn_4Si_2O_7(OH)\cdot 2H_2O$, and its dehydrated analogue $Zn_4Si_2O_7(OH)_2$: a calorimetric and thermodynamic investigation of their phase transitions. Eur. J. Mineral. **21**, 971–983 (2009)
133. F. Grønvold, A. Sveen, Heat capacity and thermodynamic properties of synthetic magnetite (Fe_3O_4) from 300 to 1050 K. Ferrimagnetic transition and zero-point entropy. J. Chem. Thermodyn. **6**, 859–872 (1974)
134. E. Dachs et al., A calorimetric investigation of spessartine: vibrational and magnetic heat capacity. Geochim. Cosmochim. Acta **73**, 3393–3409 (2009)
135. E. Dachs, C. Geiger, A. Benisek, A calorimetric study of almandine: are the thermodynamic properties of the end-member aluminosilicate garnets finally known quantitatively?, in *AGU Fall Meeting Abstracts* (2012)
136. T. Holland, R. Powell, Thermodynamics of order-disorder in minerals: I. Symmetric formalism applied to minerals of fixed composition. Am. Mineral. **81**(11–12), 1413–1424 (1996)
137. T. Holland, R. Powell, Thermodynamics of order-disorder in minerals: II. Symmetric formalism applied to solid solutions. Am. Mineral. **81**(11–12), 1425–1437 (1996)
138. Q. Chen, B. Sundman, Modeling of thermodynamic properties for Bcc, Fcc, liquid, and amorphous iron. J. Phase Equilib. **22**, 631–644 (2001). <https://doi.org/10.1007/s11669-001-0027-9>
139. W. Xiong et al., An improved magnetic model for thermodynamic modeling. Calphad **39**, 11–20 (2012)
140. P.J. Heaney, D.R. Veblen, Observations of the alpha-beta phase transition in quartz: a review of imaging and diffraction studies and some new result. Am. Miner. **76**, 1018–1032 (1991)
141. S. Stolen et al., *Heat Capacity and Thermodynamic Properties of Nearly Stoichiometric Wüstite from 13 to 450 K* (Mineralogical Society of America, Washington, 1996)
142. F. Grønvold et al., Heat capacities of the wüstites $Fe_{0.9379}O$ and $Fe_{0.9254}O$ at temperatures T from 5 K to 350 K. Thermodynamics of the reactions: $xFe(s) + (1/4)Fe_3O_4(s) = Fe_{0.7500}O(s) + xO(s) = Fe_{1-y}O(s)$ at $T \approx 850$ K, and properties of $Fe_{1-y}O(s)$ to $T = 1000$ K. Thermodynamics of formation of wüstite. J. Chem. Thermodyn. **25**, 1089–1117 (1993). <https://doi.org/10.1006/jcht.1993.1107>
143. P. Blanc et al., Thermodynamics of clay minerals, in *Developments in Clay Science* (Elsevier, Amsterdam, 2013), pp. 173–210
144. K.M. Krupka, *Thermodynamic Analysis of Some Equilibria in the System Magnesium Oxide-Silicon Dioxide-Water (Calorimetry, Metamorphic, Heat Capacity)* (The Pennsylvania State University, State College, 1984)
145. R. Robie, B. Hemingway, W. Wilson, Heat capacities of calorimetry conference copper and muscovite $KAl_2(AlSi_3)O_{10}(OH)_2$, pyrophyllite $Al_2Si_4O_{10}(OH)_2$, and illite $K_3(Al_7/Mg(Si_{14}Al_2)O_{40}(OH)_8$ between 15 and 3750/K and their standard entropies at 298.150/K. J. Res. U.S. Geol. Surv. **4**, 640 (1976)
146. J. Leitner et al., Estimation of heat capacities of solid mixed oxides. Thermochim. Acta **395**(1–2), 27–46 (2002)
147. L. Qiu, M.A. White, The constituent additivity method to estimate heat capacities of complex inorganic solids. J. Chem. Educ. **78**, 1076 (2001)
148. W.M. Latimer, Methods of estimating the entropies of solid compounds. J. Am. Chem. Soc. **73**, 1480–1482 (1951). <https://doi.org/10.1021/ja01148a021>
149. W.S. Fyfe, *Metamorphic Reactions and Metamorphic Facies*, vol. 73. Memoir (Geological Society of America, Washington, 1959)
150. H.C. Helgeson, Summary and critique of the thermodynamic properties of rock-forming minerals. Am. J. Sci. **278**, 1–229 (1978)

151. V. Van Hinsberg, S. Vriend, J. Schumacher, A new method to calculate end-member thermodynamic properties of minerals from their constituent polyhedra II: heat capacity, compressibility and thermal expansion. *J. Metamorph. Geol.* **23**, 681–693 (2005)
152. V. Van Hinsberg, S. Vriend, J. Schumacher, A new method to calculate end-member thermodynamic properties of minerals from their constituent polyhedra I: enthalpy, entropy and molar volume. *J. Metamorph. Geol.* **23**, 165–179 (2005)
153. J.A. Chermak, J.D. Rimstidt, Estimating the thermodynamic properties (ΔG of and ΔH of) of silicate minerals at 298 K from the sum of polyhedral contributions. *Am. Miner.* **74**(9–10), 1023–1031 (1989)
154. P. Blanc et al., A generalized model for predicting the thermodynamic properties of clay minerals. *Am. J. Sci.* **315**, 734–780 (2015)
155. P. Richet et al., Thermodynamic properties of quartz, cristobalite and amorphous SiO_2 : drop calorimetry measurements between 1000 and 1800 K and a review from 0 to 2000 K. *Geochim. Cosmochim. Acta* **46**, 2639–2658 (1982). [https://doi.org/10.1016/0016-7037\(82\)90383-0](https://doi.org/10.1016/0016-7037(82)90383-0)
156. S.K. Saxena, G. Shen, Assessed data on heat capacity, thermal expansion, and compressibility for some oxides and silicates. *J. Geophys. Res. Solid Earth* **97**(B13), 19813–19825 (1992). <https://doi.org/10.1029/92jb01555>
157. P. Dorogokupets, A. Oganov, Intrinsic anharmonicity in equations of state of solids and minerals, in *Doklady Earth Sciences C/C of Doklady-Akademiia Nauk*. Citeseer (2004)
158. G. Grimvall, *Thermophysical Properties of Materials* (Elsevier, Amsterdam, 1999)
159. W. Berg, J. Morrison, The thermal properties of alkali halide crystals. I. The heat capacity of potassium chloride, potassium bromide, potassium iodide and sodium iodide between 2.8 and 270 K. *Proc. R. Soc. Lond. A* **242**(1231), 467–477 (1957)
160. R. Pässler, Representative hybrid model used for analyses of heat capacities of group-IV, III–V, and II–VI materials. *Phys. Status Solidi B* **248**, 904–920 (2011)
161. R. Pässler, Dispersion-related theory for heat capacities of semiconductors. *Phys. Status Solidi B* **244**, 4605–4623 (2007)
162. R. Pässler, Characteristic non-Debye heat capacity formula applied to GaN and ZnO. *J. Appl. Phys.* **110**, 043530 (2011)
163. P. Dorogokupets, E. Ponomarev, E. Melekhova, Optimization of experimental data on the heat capacity, volume, and bulk moduli of minerals. *Petrology C/C Petrol.* **7**, 574–591 (1999)
164. F.D. Stacey, J.H. Hodgkinson, Thermodynamics with the Grüneisen parameter: fundamentals and applications to high pressure physics and geophysics. *Phys. Earth Planet. Interiors* **286**, 42–68 (2019). <https://doi.org/10.1016/j.pepi.2018.10.006>
165. I.F.X. Eder, *Arbeitsmethoden der Thermodynamik*, vol. II (Springer, Berlin, 1983)
166. Y. Fei, S.K. Saxena, An equation for the heat capacity of solids. *Geochim. Cosmochim. Acta* **51**, 251–254 (1987). [https://doi.org/10.1016/0016-7037\(87\)90236-5](https://doi.org/10.1016/0016-7037(87)90236-5)
167. C.G. Maier, K. Kelley, An equation for the representation of high-temperature heat content data. *J. Am. Chem. Soc.* **54**, 3243–3246 (1932)
168. J. Chipman, M. Fontana, A new approximate equation for heat capacities at high temperatures. *J. Am. Chem. Soc.* **57**, 48–51 (1935)
169. J.L. Haas Jr., J.R. Fisher, Simultaneous evaluation and correlation of thermodynamic data. *Am. J. Sci.* **276**, 525–545 (1976)
170. P. Richet, G. Fiquet, High-temperature heat capacity and premelting of minerals in the system $\text{MgO-CaO-Al}_2\text{O}_3\text{-SiO}_2$. *J. Geophys. Res. Solid Earth* **96**(B1), 445–456 (1991). <https://doi.org/10.1029/90jb02172>
171. T. Holland, Thermodynamic analysis of simple mineral systems, in *Thermodynamics of Minerals and Melts*. ed. by R.C. Newton, A. Navrotsky, B.J. Wood (Springer, New York, 1981), pp. 19–34
172. H. Bozdogan, Model selection and Akaike's information criterion (AIC): the general theory and its analytical extensions. *Psychometrika* **52**, 345–370 (1987). <https://doi.org/10.1007/BF02294361>
173. E. Eser, H. Koç, Investigations of temperature dependences of electrical resistivity and specific heat capacity of metals. *Physica B* **492**, 7–10 (2016)
174. A. Dubinov, A. Dubinova, Exact integral-free expressions for the integral Debye functions. *Tech. Phys. Lett.* **34**, 999–1001 (2008)
175. I. Gonzalez et al., Analytic expressions for Debye functions and the heat capacity of a solid. arXiv preprint (2019). [arXiv:1908.08667](https://arxiv.org/abs/1908.08667)
176. H.C. Thacher Jr., Rational approximations for the Debye functions. *J. Chem. Phys.* **32**, 638–638 (1960). <https://doi.org/10.1063/1.1730772>

177. W.W. Anderson, An analytic expression approximating the Debye heat capacity function. *AIP Adv.* **9**, 075108 (2019). <https://doi.org/10.1063/1.5110279>
178. S. Gluzman, V.I. Yukalov, Self-similarly corrected Padé approximants for the indeterminate problem. *Eur. Phys. J. Plus* **131**, 340 (2016)
179. R. Goetsch et al., Structural, thermal, magnetic, and electronic transport properties of the $\text{LaNi}_2(\text{Ge}_{1-x}\text{P}_x)_2$ system. *Phys. Rev. B* **85**, 054517 (2012)
180. G. Grimvall, C. Geiger, Dependence of thermodynamic properties on atomic masses and bonding in solids, in *Solid Solutions in Silicate and Oxide Systems*, vol. 3 (European Notes in Mineralogy, 2001), pp. 11–36.
181. T.J. Ahrens, *Mineral Physics and Crystallography: A Handbook of Physical constants* (American Geophysical Union, Washington, 1995)
182. R.A. Robie, B.S. Hemingway, H. Takei, Heat capacities and entropies of Mg_2SiO_4 , Mn_2SiO_4 and Co_2SiO_4 between 5 and 380 K. *Am. Miner.* **67**(5–6), 470–482 (1982)
183. L. Cemić, E. Dachs, Heat capacity of ferrosilite, $\text{Fe}_2\text{Si}_2\text{O}_6$. *Phys. Chem. Miner.* **33**, 457–464 (2006). <https://doi.org/10.1007/s00269-006-0090-1>
184. D. McQuarrie, *Statistical Mechanics* (Harper Collins, New York, 1976)
185. G.N. Lewis et al., *Thermodynamics* (Courier Dover Publications, Mineola, 2020)
186. V. Gurevich et al., Thermodynamic properties of cassiterite $\text{SnO} \cdot 2(\text{c})$ at 0–1500 K. *Geochem. Int. C/C Geokhim.* **42**, 962–970 (2004)
187. J. Boerio-Goates et al., Heat capacities, third-law entropies and thermodynamic functions of SiO_2 molecular sieves from $T = 0$ K to 400 K. *J. Chem. Thermodyn.* **34**, 205–227 (2002)
188. W. Yong et al., Heat capacity and entropy of rutile and TiO_2II : thermodynamic calculation of rutile– TiO_2II transition boundary. *Phys. Earth Planet. Inter.* **226**, 39–47 (2014)
189. J. Meija et al., Atomic weights of the elements 2013 (IUPAC Technical Report). *Pure Appl. Chem.* **88**, 265–291 (2016)
190. T.B. Coplen, N. Holden, Atomic weights no longer constants of nature. *Chem. Int.* **33**, 10–15 (2011)
191. F. Hawthorne, The use of end-member charge-arrangements in defining new mineral species and heterovalent substitutions in complex minerals. *Can Mineral* **40**, 699–710 (2002). <https://doi.org/10.2113/gscanmin.40.2.699>
192. W. Cross et al., A quantitative chemico-mineralogical classification and nomenclature of igneous rocks. *J. Geol.* **10**, 555–690 (1902)
193. W. Wimmenauer, Petrographie der magmatischen und metamorphen Gesteine. *Geologija* **27**, 334–336 (1985)
194. P. Anderson, G. Bjedov, Chemical stoichiometry using MATLAB, in *Technology-Based Re-Engineering Engineering Education Proceedings of Frontiers in Education FIE'96 26th Annual Conference*. IEEE (1996)
195. J. Kantor, *Stoichiometry Tools* (MATLAB Central File Exchange, 2022)
196. A. Cezairliyan, K. Maglic, V. Peletsky, *Survey of Measurement Techniques*. Compendium of Thermophysical Property Measurement Methods, vol. 1, ed. by A. Cezairliyan, K. Maglic, V. Peletsky (Springer, Berlin, 1984)
197. A. Cezairliyan, K. Maglic, V. Peletsky, *Recommended Measurement Techniques and Practices*, 1st ed. Compendium of Thermophysical Property Measurement Methods: vol. 2. (Springer, New York, 1992)
198. D.G. Archer, Thermodynamic properties of synthetic sapphire ($\alpha\text{-Al}_2\text{O}_3$), standard reference material 720 and the effect of temperature-scale differences on thermodynamic properties. *J. Phys. Chem. Ref. Data* **22**, 1441–1453 (1993). <https://doi.org/10.1063/1.555931>
199. E.F. Westrum, Jr., G.T. Furukawa, J.P. McCullough, Adiabatic low-temperature calorimetry, in *Experimental Thermodynamics* (Elsevier, Amsterdam, 1968), pp. 133–214
200. J.P. McCullough, D.W. Scott, *Calorimetry of Non-Reacting Systems: Prepared Under the Sponsorship of the International Union of Pure and Applied Chemistry Commission on Thermodynamics and the Thermochemistry*, vol. 1 (Elsevier, Amsterdam, 2013)
201. J.S. Hwang, K.J. Lin, C. Tien, Measurement of heat capacity by fitting the whole temperature response of a heat-pulse calorimeter. *Rev. Sci. Instrum.* **68**, 94–101 (1997)
202. Quantum Design, Incorporated (2019). <https://www.qdusa.com/>. Accessed 5 Aug 2019
203. J. Lashley et al., Critical examination of heat capacity measurements made on a Quantum Design physical property measurement system. *Cryogenics* **43**, 369–378 (2003)

204. E. Dachs, C. Bertoldi, Precision and accuracy of the heat-pulse calorimetric technique: low-temperature heat capacities of milligram-sized synthetic mineral samples. *Eur. J. Mineral.* **17**, 251–261 (2005)
205. C.A. Kennedy et al., Recommendations for accurate heat capacity measurements using a Quantum Design physical property measurement system. *Cryogenics* **47**, 107–112 (2007). <https://doi.org/10.1016/j.cryogenics.2006.10.001>
206. E. Dachs, A. Benisek, A sample-saving method for heat capacity measurements on powders using relaxation calorimetry. *Cryogenics* **51**, 460–464 (2011). <https://doi.org/10.1016/j.cryogenics.2011.04.011>
207. A. Benisek, E. Dachs, H. Kroll, Thermochemistry of the alkali feldspars: calorimetric study of the entropy relations in the low albite-low microcline series. *Am. Miner.* **99**, 76–83 (2014)
208. C.E. Bernardes, A. Joseph, M.E.M. da Piedade, Some practical aspects of heat capacity determination by differential scanning calorimetry. *Thermochim. Acta* **687**, 178574 (2020)
209. S. Tanaka, Theory of power-compensated DSC. *Thermochim. Acta* **210**, 67–76 (1992). [https://doi.org/10.1016/0040-6031\(92\)80277-4](https://doi.org/10.1016/0040-6031(92)80277-4)
210. M. Abd-Elghany, T.M. Klapötke, A review on differential scanning calorimetry technique and its importance in the field of energetic materials. *Phys. Sci. Rev.* (2018). <https://doi.org/10.1515/psr-2017-0103>
211. N. Zucca et al., An analytical expression of the output of a power-compensated DSC in a wide temperature range. *Thermochim. Acta* **413**, 117–125 (2004). <https://doi.org/10.1016/j.tca.2003.10.006>
212. G. Höhne et al., *Differential Scanning Calorimetry* (Springer, Berlin, 2003)
213. K. Gavrichev et al., Thermodynamic properties and phase transition of monoclinic terbium orthophosphate. *Thermochim. Acta* **641**, 63–70 (2016)
214. S.C. McRaw, C. Anderson et al., Differential scanning calorimetry, in *CINDAS DATA Series on Material Properties*, ed. by Y.S. Touloukian, C.Y. Ho (Hemisphere Publishing Corporation, New York, 1988), pp. 395–435
215. A. Bosenick, C.A. Geiger, L. Cemič, Heat capacity measurements of synthetic pyrope-grossular garnets between 320 and 1000 K by differential scanning calorimetry. *Geochim. Cosmochim. Acta* **60**, 3215–3227 (1996)
216. E. Dachs, A. Benisek, G. Redhammer, P21/c-C2/c phase transition and mixing properties of the (Li, Na) FeGe₂O₆ solid solution: a calorimetric and thermodynamic study. *J. Chem. Thermodyn.* **120**, 123–140 (2018)
217. G.W.H. Höhne, W. Hemminger, H.-J. Flammersheim, The DSC curve, in *Differential Scanning Calorimetry: An Introduction for Practitioners* (Springer, Berlin, 1996), pp. 81–104. https://doi.org/10.1007/978-3-662-03302-9_5
218. G.W.H. Höhne, W. Hemminger, H.-J. Flammersheim, DSC curves and further evaluations, in *Differential Scanning Calorimetry* (Springer, Berlin, 2003), pp. 115–146. https://doi.org/10.1007/978-3-662-06710-9_5
219. R.L. Danley, New heat flux DSC measurement technique. *Thermochim. Acta* **395**, 201–208 (2002). [https://doi.org/10.1016/S0040-6031\(02\)00212-5](https://doi.org/10.1016/S0040-6031(02)00212-5)
220. V.Y. Bodryakov, Heat capacity of solid tantalum: self-consistent calculation. *High Temp.* **51**, 206–214 (2013)
221. C.A. Geiger, N.M. Vielreicher, E. Dachs, Are the thermodynamic properties of natural and synthetic Mg₂SiO₄–Fe₂SiO₄ olivines the same? *Am. Mineral. J. Earth Planet. Mater.* **106**, 317–321 (2021)
222. A.E. Rubin, C. Ma, Meteoritic minerals and their origins. *Geochemistry* **63**, 101326 (2017)
223. H.-R. Wenk, A. Bulakh, *Minerals: Their Constitution and Origin* (Cambridge University Press, Cambridge, 2016)
224. O. Namur, B. Charlier, Silicate mineralogy at the surface of Mercury. *Nat. Geosci.* **10**, 9–13 (2017)
225. A. Rubin, C. Ma, *Meteorite Mineralogy*. Cambridge Planetary Science (Cambridge University Press, Cambridge, 2021)
226. M. Gilmore et al., Venus surface composition constrained by observation and experiment. *Space Sci. Rev.* **212**, 1511–1540 (2017). <https://doi.org/10.1007/s11214-017-0370-8>
227. B. Fegley, A.H. Treiman, V.L. Sharpton, Venus surface mineralogy: OBSERVATIONAL and theoretical constraints, in *Proceedings of Lunar and Planetary Science*, vol. 22 (Lunar and Planetary Institute, Houston, 1992)
228. G. Heiken, D. Vaniman, B.M. French, *Lunar Sourcebook—A User's Guide to the Moon* (Cambridge University Press, Cambridge, 1991), p. 736

229. E.H. Nickel, Solid solutions in mineral nomenclature. *Mineral. Petrol.* **46**, 49–53 (1992)
230. R.V. Gaines, J.D. Dana, E.S. Dana, *Dana's New Mineralogy: The System of Mineralogy of James Dwight Dana and Edward Salisbury Dana*, 8th edn. (Wiley, New York, 1997)
231. H. Strunz, E. Nickel, *Strunz Mineralogical Tables* (E. Schweizerbart'sche Verlagsbuchhandlung, Berlin, 2001)
232. J.W. Anthony et al., *Handbook of Mineralogy*. Mineralogical Society of America (Mineral Data Publishing, Chantilly, 2022). <http://www.handbookofmineralogy.org/>
233. MSA and MAC, *American Mineralogist Crystal Structure Database*. Mineralogical Society of America and the Mineralogical Association of Canada (2022). <https://rruff.geo.arizona.edu/AMS/amcsd.php>
234. RRUFF, RRUFF database, pdf summaries. Project website <https://rruff.info/> containing an integrated database of Raman spectra, X-ray diffraction and chemistry data for minerals. (Lafuente B, Downs R T, Yang H, Stone N (2015) The power of databases: the RRUFF project, in *Highlights in Mineralogical Crystallography*, ed. By T. Armbruster, R.M. Danisi (W. De Gruyter, Berlin, 2002), pp. 1–30
235. mindat.org, *mindat.org database, The World's Largest Open Database of Minerals, Rocks, Meteorites and the Localities They Come from* (Hudson Institute of Mineralogy, Keswick, 2022)
236. D. Barthelmy, *Mineralogy Database* (2014). <http://www.webmineral.com>
237. L.N. Warr, IMA–CNMNC approved mineral symbols. *Mineral. Mag.* **85**, 291–320 (2021). <https://doi.org/10.1180/mgm.2021.43>
238. E.C. Robertson, *Thermal Properties of Rocks* (US Geological Survey, Washington, 1988)
239. H. Kroll, H.U. Bambauer, U. Schirmer, The high albite-monalbite and analbite-monalbite transitions. *Am. Miner.* **65**(11–12), 1192–1211 (1980)
240. T.R. Schneider, F. Laves, Barbierit oder Monalbit? *Z. Krist. Cryst. Mater.* **109**(1–6), 241–244 (1957)
241. E. Salje et al., Thermodynamics of sodium feldspar II: Experimental results and numerical calculations. *Phys. Chem. Miner.* **12**, 99–107 (1985). <https://doi.org/10.1007/bf01046834>
242. A. Putnis, *An Introduction to Mineral Sciences* (Cambridge University Press, Cambridge, 1992)
243. A. Benisek, E. Dachs, M.A. Carpenter, Heat capacity and entropy of low structural state plagioclases. *Phys. Chem. Miner.* **40**, 167–173 (2013). <https://doi.org/10.1007/s00269-012-0556-2>
244. N. Morimoto, Nomenclature of pyroxenes. *Mineral. Petrol.* **39**, 55–76 (1988)
245. M. Kimura et al., Kushiroite, CaAlAlSiO_6 : a new mineral of the pyroxene group from the ALH 85085 CH chondrite, and its genetic significance in refractory inclusions. *Am. Miner.* **94**, 1479–1482 (2009)
246. C. Ma et al., Calcium Tschermak's pyroxene, CaAlAlSiO_6 , from the Allende and Murray meteorites: EBSD and micro-Raman characterizations. *Am. Miner.* **94**, 1483–1486 (2009)
247. A.E. Rubin, Mineralogy of meteorite groups. *Meteorit. Planet. Sci.* **32**, 231–247 (1997). <https://doi.org/10.1111/j.1945-5100.1997.tb01262.x>
248. S.M.H. De Angelis, O.K. Neill, MINERAL: a program for the propagation of analytical uncertainty through mineral formula recalculations. *Comput. Geosci.* **48**, 134–142 (2012). <https://doi.org/10.1016/j.cageo.2012.05.023>
249. M.R. Smith, J.L. Bandfield, Geology of quartz and hydrated silica-bearing deposits near Antoniadi Crater, Mars. *J. Geophys. Res. Planets* (2012). <https://doi.org/10.1029/2011JE004038>
250. C.L. Snow et al., Heat capacity studies of the iron oxyhydroxides akaganéite ($\beta\text{-FeOOH}$) and lepidocrocite ($\gamma\text{-FeOOH}$). *J. Chem. Thermodyn.* **43**, 190–199 (2011). <https://doi.org/10.1016/j.jct.2010.08.022>
251. B. Gleeson, S. Hadavi, D. Young, Isothermal transformation behavior of thermally-grown wüstite. *Mater. High Temp.* **17**, 311–318 (2000)
252. M.C. De Sanctis et al., Fresh emplacement of hydrated sodium chloride on Ceres from ascending salty fluids. *Nat. Astron.* **4**, 786–793 (2020). <https://doi.org/10.1038/s41550-020-1138-8>
253. T.E. Warner, N.M. Rice, N. Taylor, Thermodynamic stability of pentlandite and violarite and new EH-pH diagrams for the iron-nickel sulphur aqueous system. *Hydrometallurgy* **41**, 107–118 (1996). [https://doi.org/10.1016/0304-386X\(95\)00081-Q](https://doi.org/10.1016/0304-386X(95)00081-Q)
254. A. Sugaki, A. Kitakaze, High form of pentlandite and its thermal stability. *Am. Miner.* **83**(1–2), 133–140 (1998)
255. J.R. DeLaeter, The Mundrabilla Meteorite Shower. *Meteoritics* **7**, 285–294 (1972). <https://doi.org/10.1111/j.1945-5100.1972.tb00442.x>

256. J.H. Allton, S.J. Wentworth, J.L. Gooding, Calorimetric thermometry of meteoritic troilite: preliminary thermometer relationships, in *Lunar and Planetary Science Conference* (1994)
257. F. Grønvold, E.F. Westrum, α -Ferric oxide: low temperature heat capacity and thermodynamic functions. *J. Am. Chem. Soc.* **81**, 1780–1783 (1959)
258. C.-W. Yang, D. Williams, J. Goldstein, A revision of the Fe–Ni phase diagram at low temperatures (< 400 C). *J. Phase Equilib.* **17**, 522–531 (1996)
259. G.P. Vdovykin, The Canyon Diablo meteorite. *Space Sci. Rev.* **14**, 758–831 (1973)
260. C.B. Moore, P.J. Birrell, C.F. Lewis, Variations in the chemical and mineralogical composition of rim and plains specimens of the Cañon Diablo meteorite. *Geochim. Cosmochim. Acta* **31**, 1885–1892 (1967)
261. B. Wilthan, Bestimmung der spezifischen Wärmekapazität von Stoffen mittels dynamischer Differenzkalorimetrie, in *Physics* (TU Graz, Graz, 2002)
262. C.P. Butler, R.J. Jenkins, Thermal properties of meteoritic iron from -150° to 300° C. *Science* **139**(3554), 486–487 (1963)
263. M. Szurgot, On the specific heat capacity and thermal capacity of meteorites, in *Lunar and Planetary Science Conference* (2011)
264. R.A. Howald, The thermodynamics of tetraenaite and awaruite: a review of the Fe–Ni phase diagram. *Metall. Mater. Trans. A* **34**, 1759–1769 (2003)
265. J.I. Goldstein, J.M. Short, The iron meteorites, their thermal history and parent bodies. *Geochim. Cosmochim. Acta* **31**, 1733–1770 (1967)
266. K. Reuter, D.B. Williams, J. Goldstein, Determination of the Fe–Ni phase diagram below 400° C. *Metall. Trans. A* **20**, 719–725 (1989)
267. W. Xiong et al., Magnetic phase diagram of the Fe–Ni system. *Acta Mater.* **59**, 521–530 (2011). <https://doi.org/10.1016/j.actamat.2010.09.055>
268. F. Körmann et al., Lambda transitions in materials science: Recent advances in CALPHAD and first-principles modelling. *Phys. Status Solidi B* **251**, 53–80 (2014). <https://doi.org/10.1002/pssb.201350136>
269. M. Hillert, M. Jarl, A model for alloying in ferromagnetic metals. *Calphad* **2**, 227–238 (1978)
270. A.D. Romig, Determination of the iron rich portion of the iron-nickel-carbon phase diagram (1977)
271. S. Sugita, R. Honda, T. Morota, The geomorphology, color, and thermal properties of Ryugu: implications for parent-body processes. *Science* **364**(6437), eaaw0422 (2019). <https://doi.org/10.1126/science.aaw0422>
272. S. Guggenheim et al., Summary of recommendations of nomenclature committees relevant to clay mineralogy: report of the Association Internationale pour l'Etude des Argiles (AIPEA) Nomenclature Committee for 2006. *Clay Miner.* **41**, 863–877 (2006). <https://doi.org/10.1180/0009855064140225>
273. P.A. Bland, G. Cressey, O.N. Menzies, Modal mineralogy of carbonaceous chondrites by X-ray diffraction and Mössbauer spectroscopy. *Meteorit. Planet. Sci.* **39**, 3–16 (2004)
274. K. Tomeoka, P.R. Buseck, Matrix mineralogy of the Orgueil CI carbonaceous chondrite. *Geochim. Cosmochim. Acta* **52**, 1627–1640 (1988). [https://doi.org/10.1016/0016-7037\(88\)90231-1](https://doi.org/10.1016/0016-7037(88)90231-1)
275. O. Vidal, B. Dubacq, Thermodynamic modelling of clay dehydration, stability and compositional evolution with temperature, pressure and H₂O activity. *Geochim. Cosmochim. Acta* **73**, 6544–6564 (2009). <https://doi.org/10.1016/j.gca.2009.07.035>
276. P. Vieillard, Thermodynamics of hydration in minerals: how to predict these entities, in *Thermodynamics—Fundamentals and Its Application in Science* (InTechOpen, London, 2012), pp. 339–370
277. A. Garenne et al., The abundance and stability of “water” in type 1 and 2 carbonaceous chondrites (CI, CM and CR). *Geochim. Cosmochim. Acta* **137**, 93–112 (2014). <https://doi.org/10.1016/j.gca.2014.03.034>
278. L. Pohl, *The Physical Properties of Asteroids* (Department of Physics, University of Central Florida, Orlando, 2020).
279. K.J.D. MacKenzie, R.M. Berezowski, Thermal and Mossbauer studies of iron-containing hydrous silicates. III. Cronstedtite. *Thermochim. Acta* **44**, 171–187 (1981). [https://doi.org/10.1016/0040-6031\(81\)80039-1](https://doi.org/10.1016/0040-6031(81)80039-1)
280. C. Zhang et al., Metal occupancy and its influence on thermal stability of synthetic saponites. *Appl. Clay Sci.* **135**, 282–288 (2017)
281. F. Franks, ed., Water in disperse systems, in *Water: A Comprehensive Treatise*, vol. 5, ed. F. Franks (Springer, New York, 1975).

282. D.B. Asay, S.H. Kim, Evolution of the adsorbed water layer structure on silicon oxide at room temperature. *J. Phys. Chem. B* **109**, 16760–16763 (2005)
283. J. Majzlan et al., Thermodynamics of Fe oxides: Part I. Entropy at standard temperature and pressure and heat capacity of goethite (α -FeOOH), lepidocrocite (γ -FeOOH), and maghemite (γ -Fe₂O₃). *Am. Mineral.* **88**(5–6), 846–854 (2003)
284. V. Gurevich et al., Heat capacity and thermodynamic functions of epsomite MgSO₄·7H₂O at 0–303 K. *Geochem. Int.* **45**, 206–209 (2007)
285. I. Paukov et al., Low-temperature thermodynamic properties of disordered zeolites of the natrolite group. *Phys. Chem. Miner.* **29**, 300–306 (2002)
286. G. Johnson, H. Flotow, P. O'hare, Thermodynamic studies of zeolites: analcime and dehydrated analcime. *Am. Mineral.* **67**(7–8), 736–748 (1982)
287. C.A. Geiger et al., Molecular H₂O in armenite, BaCa₂Al₆Si₉O₃₀·2H₂O, and epididymite, Na₂Be₂Si₆O₁₅·H₂O: heat capacity, entropy and local-bonding behavior of confined H₂O in microporous silicates. *Geochim. Cosmochim. Acta* **74**, 5202–5215 (2010)
288. I.E. Paukov et al., Heat capacity of synthetic hydrous Mg-cordierite at low temperatures: thermodynamic properties and the behavior of the H₂O molecule in selected hydrous micro and nanoporous silicates. *Am. Miner.* **92**(2–3), 388–396 (2007)
289. C.A. Geiger, E. Dachs, Quasi-ice-like CP behavior of molecular H₂O in hemimorphite Zn₄Si₂O₇(OH)·2H₂O:CP and entropy of confined H₂O in microporous silicates. *Am. Miner.* **94**, 634–637 (2009)
290. W. Giauque, J. Stout, The entropy of water and the third law of thermodynamics. The heat capacity of ice from 15 to 273 K. *J. Am. Chem. Soc.* **58**, 1144–1150 (1936)
291. C. Angell, W. Sichina, M. Oguni, Heat capacity of water at extremes of supercooling and superheating. *J. Phys. Chem.* **86**, 998–1002 (1982)
292. D. Eisenberg and W. Kauzmann, *Water: The Structure and Properties of Water*, vol. 166. Oxford Classic Series, ed. by W. Drost-Hansen (Oxford University Press, New York, 1969), p. 861
293. G.J. MacPherson, 1.08—Calcium–Aluminum-Rich Inclusions in Chondritic Meteorites, in *Treatise on Geochemistry*, ed. by H.D. Holland, K.K. Turekian (Pergamon, Oxford, 2007), pp. 1–47. <https://doi.org/10.1016/B0-08-043751-6/01065-3>.
294. A.S. Doan, J. Goldstein, The formation of phosphides in iron meteorites, in *Meteorite Research* (Springer, New York, 1969), pp. 763–779
295. R.V. Morris et al., Silicic volcanism on Mars evidenced by tridymite in high-SiO₂ sedimentary rock at Gale crater. *Proc. Natl. Acad. Sci. USA* **113**, 7071–7076 (2016)
296. D.D. Clayton, L.R. Nittler, Astrophysics with Presolar Stardust. *Annu. Rev. Astron. Astrophys.* **42**, 39–78 (2004). <https://doi.org/10.1146/annurev.astro.42.053102.134022>
297. T. Nakamura, Post-hydration thermal metamorphism of carbonaceous chondrites. *J. Mineral. Petrol. Sci.* **100**, 260–272 (2005)
298. M.A. Sephton, Organic compounds in carbonaceous meteorites. *Nat. Prod. Rep.* **19**, 292–311 (2002). <https://doi.org/10.1039/B103775G>
299. M.J. Richardson, The specific heats of coals, cokes and their ashes. *Fuel* **72**, 1047–1053 (1993). [https://doi.org/10.1016/0016-2361\(93\)90307-N](https://doi.org/10.1016/0016-2361(93)90307-N)
300. V. Laštovka et al., A similarity variable for estimating the heat capacity of solid organic compounds: Part II. Application: heat capacity calculation for ill-defined organic solids. *Fluid Phase Equilib.* **268**, 134–141 (2008). <https://doi.org/10.1016/j.fluid.2008.03.018>
301. R.L. Levy, M.A. Grayson, C.J. Wolf, The organic analysis of the Murchison meteorite. *Geochim. Cosmochim. Acta* **37**, 467–483 (1973)
302. D. Stöffler, Glasses formed by hypervelocity impact. *J. Non-Cryst. Solids* **67**(1–3), 465–502 (1984)
303. M. Chen, A. El Goresy, The nature of maskelynite in shocked meteorites: not diaplectic glass but a glass quenched from shock-induced dense melt at high pressures. *Earth Planet. Sci. Lett.* **179**(3–4), 489–502 (2000)
304. S.J. Jaret et al., Maskelynite formation via solid-state transformation: evidence of infrared and X-ray anisotropy. *J. Geophys. Res. Planets* **120**, 570–587 (2015)
305. Y. Inamura et al., Peculiar suppression of the specific heat and boson peak intensity of densified SiO₂ glass. *Physica B* **263–264**, 299–302 (1999). [https://doi.org/10.1016/S0921-4526\(98\)01362-3](https://doi.org/10.1016/S0921-4526(98)01362-3)
306. G. Grimvall, S. Sjödin, Correlation of properties of materials to Debye and melting temperatures. *Phys. Scr.* **10**, 340 (1974)
307. C. Ferrari, A. Lucas, Low thermal inertias of icy planetary surfaces-Evidence for amorphous ice? *Astron. Astrophys.* **588**, A133 (2016)

308. C. Ferrari, Thermal properties of icy surfaces in the outer solar system. *Space Sci. Rev.* **214**, 111 (2018). <https://doi.org/10.1007/s11214-018-0546-x>
309. R. Hanus, Heat conduction in defective and complex crystals: phonon scattering and beyond, in *Materials Science & Engineering*. PhD thesis. Northwestern University, Evanston (2019)
310. M.S. Gudipati, J. Castillo-Rogez, eds., *The Science of Solar System Ices*. Springer Astrophysics and Space Science Library, vol. 356 (Springer, New York, 2013)
311. M. Barucci et al., Surface composition and temperature of the TNO Orcus. *Astron. Astrophys.* **479**, L13–L16 (2008)
312. M. Barucci, N. Peixinho, Trans-Neptunian objects' surface properties. *Proc. Int. Astron. Union* **1**(S229), 171–190 (2005)
313. C.D. Bergh, et al. The ices on transneptunian objects and Centaurs, in *The Science of Solar System Ices* (Springer, New York, 2013), pp. 107–146
314. E. Quirico et al., New experimental constraints on the composition and structure of tholins. *Icarus* **198**, 218–231 (2008)
315. C.P. McKay et al., Physical properties of the organic aerosols and clouds on Titan. *Planet. Space Sci.* **49**, 79–99 (2001). [https://doi.org/10.1016/S0032-0633\(00\)00051-9](https://doi.org/10.1016/S0032-0633(00)00051-9)
316. J.P. Chan, W.F. Giauque, The entropy of $\text{NH}_3 \cdot 2\text{H}_2\text{O}$. Heat capacity from 15 to 300°K. *J. Phys. Chem.* **68**, 3053–3057 (1964)
317. J. Biele, M. Grott, Reference heat capacity for asteroid regolith from 10 to 1000 K, in *49th Lunar and Planetary Science Conference* (Lunar and Planetary Institute, Houston, 2018), p. Abstract #1877
318. B.S. Hemingway, R.A. Robie, W.H. Wilson, Specific heats of lunar soils, basalt, and breccias from the Apollo 14, 15, and 16 landing sites, between 90 and 350 K, in *Proceedings of the Fourth Lunar Science Conference (Supplement 4, Geochimica et Cosmochimica Acta)* pp. 2481–2487 (1973)
319. P.O. Hayne et al., Global regolith thermophysical properties of the moon from the diviner lunar radiometer experiment. *J. Geophys. Res. Planets* (2017). <https://doi.org/10.1002/2017je005387>
320. A.J. Colozza, *Analysis of Lunar Regolith Thermal Energy Storage* (Sverdrup Technology, Brook Park, 1991)
321. M.J. Ledlow et al., Subsurface emission from mercury: VLA radio observations at 2 and 6 centimeters. *ApJ* (1992). <https://doi.org/10.1086/170906>
322. N. Fujii, M. Osako, Thermal diffusivity of lunar rocks under atmospheric and vacuum conditions. *Earth Planet. Sci. Lett.* **18**, 65–71 (1973)
323. R. Robie, B. Hemingway, W. Wilson. Specific heats of lunar surface materials from 90 to 350 K, in *Proceedings of the Apollo 11 Lunar Science Conference*, 5–8 January, 1970. *Geochimica et Cosmochimica Acta Supplement 1*, Houston, TX (1970)
324. S.S. Schreiner et al., Thermophysical property models for lunar regolith. *Adv. Space Res.* **57**, 1209–1222 (2016). <https://doi.org/10.1016/j.asr.2015.12.035>
325. J. Stebbins, I. Carmichael, L. Moret, Heat capacities and entropies of silicate liquids and glasses. *Contrib. Miner. Petrol.* **86**, 131–148 (1984)
326. J.A. Morrison, P.J. Norton, The heat capacity and thermal conductivity of Apollo 11 lunar rocks 10017 and 10046 at liquid helium temperatures. *J. Geophys. Res.* **75**, 6553–6557 (1970)
327. M.E. Zolensky et al., Physical, chemical, and petrological characteristics of chondritic materials and their relationships to small solar system bodies, in *Primitive Meteorites and Asteroids*. ed. by N. Abreu (Elsevier, Amsterdam, 2018), pp. 59–204. <https://doi.org/10.1016/B978-0-12-813325-5.00002-1>
328. M. Delbo, P. Michel, Temperature history and dynamical evolution of (101955) 1999 RQ 36: a potential target for sample return from a primitive asteroid. *Astrophys. J. Lett.* **728**, L42 (2011)
329. H. Miyamoto et al., Phobos environment model and regolith simulant for MMX mission, in *49th Lunar and Planetary Science Conference 2018* (LPI, Houston, 2018)
330. M. Isachenkov et al., Characterization of novel lunar highland and mare simulants for ISRU research applications. *Icarus* **376**, 114873 (2022)
331. Mitchell, M., et al., *Engauge Digitizer Software* (2020)

Authors and Affiliations

Jens Biele¹  · Matthias Grott² · Michael E. Zolensky³ · Artur Benisek⁴ · Edgar Dachs⁴

¹ RB-MUSC, DLR – German Aerospace Center, 51147 Cologne, Germany

² Institute for Planetary Research, DLR – German Aerospace Center, Berlin, Germany

³ NASA Johnson Space Center, Houston, USA

⁴ Chemistry and Physics of Materials, University of Salzburg, Jakob-Haringer-Str. 2a, 5020 Salzburg, Austria